To the Graduate Council:

I am submitting herewith a dissertation written by Earl Evans Ingram entitled "Behavior of Piles Supporting Integral Abutments." I have examined the final paper copy of this dissertation for form and content and recommend that it be accepted in partial fulfillment of the degree of Doctor of Philosophy, with a major in Civil Engineering.

Edwin G. Burdette

Edwin G. Burdette, Major Professor

We have read this dissertation and recommend its acceptance:

Acceptance for the Council:

Vice Provost and Dean of Graduate Studies

BEHAVIOR OF PILES SUPPORTING INTEGRAL ABUTMENTS

A Dissertation
Presented for the
Doctor of Philosophy
Degree
The University of Tennessee, Knoxville

Earl Evans Ingram
August 2002

Thesis
2002b
.I54

DEDICATION

This Dissertation is dedicated to my wife, Christa Ingram, and my children, Dan Earl Ingram and Emma Clara Ingram, for providing me with the love, support, and encouragement that help me to achieve my goals.

ACKNOWLEDGEMENTS

Numerous individuals have provided me with moral and financial support during my tenure as a graduate student. First and foremost, I would like to thank my wife, Christa, for her endless support of my pursuit of this degree, and doing more than her fair share of the parenting of our children during this process.

I would like to express my gratitude to the members of my committee for their tireless support during this endeavor. I am especially thankful to my major professor, Dr. Edwin G. Burdette, for his guidance, constructive criticism, mentoring, and friendship. The education that I received inside, as well as outside, of the classroom from my committee members, Drs. Richard M. Bennett, J. Harold Deatherage, David W. Goodpasture, and Chris D. Pionke, is something for which I will forever be grateful.

Many graduate and undergraduate students worked diligently on collecting much of the data that were used in this dissertation. They include Samer Al-Jamal, Laura Arico, Eric Bonanno, Brian Calloway, Ken Harvey, Jay Lewis, Chris Myers, Jeremy Pettus, Todd Philips, and Anthony Zeind. The conducted research would not have been possible without the generous support of TDOT and particularly of Edward Wasserman.

I am very thankful to the Burdette family for awarding me with the Edwin G. and Patsy Burdette Fellowship during my graduate studies. Their generous support is much appreciated. In addition to the Burdettes' kind support, Dr. Roger Parsons allowed me to work with the Engage program, for which I am very grateful.

Finally, I would like to thank my parents, Bruce and Gloria Ingram, for always being supportive of my endeavors. I am very lucky to have such wonderful parents.

ABSTRACT

Steel H-piles are commonly used to support integral abutments. In the absence of expansion joints that allow the superstructure to expand and contract freely, piles supporting integral abutments are subjected to lateral displacement, horizontal shear, and bending moment. Data are presented in this dissertation that describe the variation of bending moment and lateral pressure with depth of pile, and comparisons of test data with predicted values from a commercially available software, LPILE, are made.

The piles supporting integral abutments are often designed according to column interaction equations presented by AASHTO or AISC specifications. Both sets of specifications provide valid design approaches for columns subjected to combined stresses. However, neither specification addresses how to account for lateral support provided by surrounding soil.

The main focus of this dissertation centers on predicting the buckling capacity of a pile surrounded by soil and subjected to combined axial and bending forces. Field test data obtained from full-scale lateral load tests that included ultimate capacity tests performed in Tennessee were used to develop finite element models of the pile-soil system. The models were executed for various magnitudes of soil stiffness to investigate the relationship between soil stiffness and pile stability. Results produced an approximate minimum soil stiffness required to prevent buckling prior to a yielding failure of the pile. Based on results presented herein, a suggested design approach for determining the structural capacity of a laterally loaded pile is presented.

TABLE OF CONTENTS

Chapter Page

1. INTRODUCTION, PROBLEM STATEMENT, AND OVERVIEW OF SOLUTION 1
- Introduction 1
- Statement of Problem 1
- Overview of Solution Process 2
- Objectives 9

2. REVIEW OF LITERATURE 11
- The Practice of Jointless Bridge Construction 11
- Experimental Studies 12
- Modeling Lateral Soil-Pile Response 14
- Buckling in Elastic Continuum 15
- Buckling of Piles 16
- Analysis and Design of Laterally Loaded Piles 17

3. DESCRIPTION OF FIELD TESTS 21
- Field Tests 21
- Ultimate Capacity Hold-Down Test Description 27
- Ultimate Capacity Hold-Down Test Results 29

4. APPLICABLE USES OF LPILE 33
- Objective 33
- Description of LPILE 33
- Comparison of Field Data to LPILE Predictions 36
- Limited Sensitivity Study 39
- Conclusion 41

5. TYPICAL COLUMN DESIGN EQUATIONS RELATED TO LATERALLY LOADED STEEL H-PILES 45
- Introduction 45
- American Association of State Highway and Transportation Officials 45
- American Institute of Steel Construction 51
- Plastic Limit 57
- Comparison to Results Obtained From Field Tests 58
- Conclusion 59

6. MODEL VERIFICATION 61
- Introduction 61
- Element Choice 61
- Verification of Section Properties 64
- Error Prediction 69

Combined Stress Behavior 73
Second-Order Effects 76
Soil Model Justification 76
Soil Model 79

7. MODELING OF PILE BEHAVIOR 85
Introduction 85
Model Specifics 87
Pile Loading 89
Constant Moment Model Results 92
Discussion of Constant Moment Model Results 94
Rotational Spring Model Results 103
Discussion of Rotational Spring Model Results 103
Fixed Rotation Model Results 112
Discussion of Fixed Rotation Model Results 113
50% Gap Model Results 120
Discussion of 50% Gap Model Results 128
Comparison of Finite Element Results with Results From Gabr's Method 129

8. CONCLUSION 131
Conclusions Drawn From Finite Element Models 131
Suggested Design Procedure 132
Potential For Further Research 133

WORKS CONSULTED 135
APPENDIX COMPUTER PROGRAM 143
VITA 153

LIST OF FIGURES

Figure Page

1. Final Bending Condition (Pile 5)....6
2. Interaction Curves (Pile 5)....6
3. Axial Load vs. Axial Deflection (Pile 5 soil)....8
4. Axial Load vs. Axial Deflection (no soil)....8
5. Field Test Setup (not to scale)....23
6. Hold-Down Field Test Setup (not to scale)....23
7. Gage Locations....25
8. Moment vs. Depth (Pile 1)....37
9. Moment vs. Depth (Pile 4)....37
10. Moment vs. Depth (Pile 5)....38
11. Moment vs. Depth (Pile 5), Shear-Rotational Stiffness Boundary Condition....40
12. Rotational Stiffness Sensitivity Study, x = 11300 kN-m/rad....40
13. Shear Strength Sensitivity Study....42
14. ε50 Sensitivity Study....42
15. Pile 5 Upper Section Interaction Curves and Results....52
16. Pile 5 Lower Section Interaction Curves and Results....52
17. Pile 3 Upper Section Interaction Curves and Results....53
18. Ansys Beam23 Element....62
19. Load vs. Deflection (HP10x42): simply supported beam L = 100 in. 66
20. Load vs. Deflection (Modified HP10x42): L = 100 in. 66
21. Moment vs. Deflection (HP10x42): simply supported beam L = 100 in. 67
22. Moment vs. Deflection (Modified HP10x42): L = 100 in. 67
23. First Yield Location (HP10x42) 68
24. First Yield Location (Modified HP10x42) 68
25. Load vs. Strain (HP10x42) 70
26. Load vs. Strain (Modified HP10x42) 70
27. Axial Load vs. Moment for Interaction Verification Models....75
28. Comparison of Finite Element Buckling Capacity to Euler Solution....77
29. Comparison of Buckling with Elastic and Elasto-plastic Material....78
30. Pile 5 Sample p-y Curves Obtained From Experimental Data....83
31. Pile 5 Initial Soil Modulus vs. Depth Obtained From Experimental Data 84
32. Euler buckling load vs. K for modified HP10x42 with L = 38.5 ft....86
33. Finite Element Model Illustration 88
34. Sample of Soil Spring Stiffness Reduction 90
35. Load vs. Axial Deflection: Constant Moment Models....93
36. Moment vs. Depth, Constant moment boundary condition (Soil = Baseline) 96

37. Deflected Shape, Constant moment boundary condition (Soil = Baseline) 96
38. Moment vs. Depth, Constant moment boundary condition (Soil = 10% of Baseline) 97
39. Deflected Shape, Constant moment boundary condition (Soil = 10% of Baseline) 97
40. Moment vs. Depth, Constant moment boundary condition (Soil = 1% of Baseline) 98
41. Deflected Shape, Constant moment boundary condition (Soil = 1% of Baseline) 98
42. Moment vs. Depth, Constant moment boundary condition (Soil = 0.1% of Baseline) 99
43. Deflected Shape, Constant moment boundary condition (Soil = 0.1% of Baseline) 99
44. Moment vs. Depth, Constant moment boundary condition (No Soil) 100
45. Deflected Shape, Constant moment boundary condition (No Soil) 100
46. Load vs. Axial Deflection: Rotational Spring Models 104
47. Moment vs. Depth, Rotational spring boundary condition (Soil = Baseline) 106
48. Deflected Shape, Rotational spring boundary condition (Soil = Baseline) 106
49. Moment vs. Depth, Rotational spring boundary condition (Soil = 10% of Baseline) 107
50. Deflected Shape, Rotational spring boundary condition (Soil = 10% of Baseline) 107
51. Moment vs. Depth, Rotational spring boundary condition (Soil = 1% of Baseline) 108
52. Deflected Shape, Rotational spring boundary condition (Soil = 1% of Baseline) 108
53. Moment vs. Depth, Rotational spring boundary condition (Soil = 0.1% of Baseline) 109
54. Deflected Shape, Rotational spring boundary condition (Soil = 0.1% of Baseline) 109
55. Moment vs. Depth, Rotational spring boundary condition (No Soil) 110
56. Deflected Shape, Rotational spring boundary condition (No Soil) 110
57. Load vs. Axial Deflection: Fixed Pile Head Models 114
58. Moment vs. Depth, Fixed pile head boundary condition (Soil = 10% of Baseline) 116
59. Deflected Shape, Fixed pile head boundary condition (Soil = 10% of Baseline) 116
60. Moment vs. Depth, Fixed pile head boundary condition (Soil = 1% of Baseline) 117
61. Deflected Shape, Fixed pile head boundary condition (Soil = 1% of Baseline) 117

62. Moment vs. Depth, Fixed pile head boundary condition (Soil = 0.1% of Baseline) 118
63. Deflected Shape, Fixed pile head boundary condition (Soil = 0.1% of Baseline) 118
64. Moment vs. Depth, Fixed pile head boundary condition (No Soil)..... 119
65. Deflected Shape, Fixed pile head boundary condition (No Soil)..... 119
66. Example Soil Spring Curve (with and without gap)..... 122
67. Initial Moment vs. Depth Comparison (Soil = Baseline) 124
68. Initial Moment vs. Depth Comparison (Soil = 0.1 x Baseline) 124
69. Initial Deflected Shape Comparison (Soil = Baseline) 125
70. Initial Deflected Shape Comparison (Soil = 0.1 x Baseline) 125
71. Moment vs. Depth, 50% Gap Model (Soil = Baseline) 126
72. Deflected Shape, 50% Gap Model (Soil = Baseline) 126
73. Moment vs. Depth, 50% Gap Model (Soil = 0.1 x Baseline) 127
74. Deflected Shape, 50% Gap Model (Soil = 0.1 x Baseline) 127

LIST OF TABLES

Table Page

1. Field Specimen Specifics 22
2. Section Properties 47
3. Weighted Areas at Integration Points 64
4. Section Verification Model Results Comparison (Third-Point Loading) 71
5. Error Prediction Model Results (Mid-span Point Load) 74
6. Buckling Model Summary of Results 77
7. Constant Moment Model Results 95
8. Rotational Spring Model Results 105
9. Fixed Pile Head Model Results 115
10. 50% Gap Model Results 123
11. P_{cr} Values Obtained From Gabr's Method (Strong Axis) 130
12. P_{cr} Values Obtained From Gabr's Method (Weak Axis) 130

NOMENCLATURE

Capital Letters

A	area
A_g	gross area (AISC)
A_s	gross effective area of the column cross section (AASHTO)
C	equivalent moment factor
E	modulus of elasticity
EI	flexural stiffness
F_{cr}	buckling stress
F_e	Euler Buckling stress in the plane of bending
F_L	reduced value of yield stress accounting for residual stresses
F_y	yield stress
I	moment of inetia
K	effective length factor
L	length
L_b	unbraced length
L_c	unbraced length
L_e	effective length of pile
L_e'	nondimensional effective length of pile
M	applied moment (AASHTO)
M_n	nominal flexural strength (AISC)
M_p	plastic moment
M_u	maximum bending strength (AASHTO)
M_u	required flexural strength (AISC)
M_y	yield moment
P	applied axial load (AASHTO)
P_{cr}	critical buckling load
P_{eu}	Euler buckling load
P_n	nominal axial strength (AISC)
P_u	required axial strength (AISC)
R_m	E_pI_p
S	elastic section modulus
V	shear
Z	plastic section modulus

Lower Case Letters

b	width of pile
b'	width of projecting flange element
c	shear strength
e	embedment ratio
h	distance between nodes
h	embedment depth of pile
h'	nondimensional embedment depth of pile

k_e effective spring constant for a given deflection
p soil reaction per unit length of pile
r radius of gyration
t thickness
t_f flange thickness
t_w web thickness
w distributed load
x depth from ground surface
y lateral displacement

Subscripts
b bending
cr critical
e effective
eu Euler
f flange
p pile
w web
x strong axis
y weak axis
y yield

Greek
α coefficient of pile-soil compliancy
Δ deflection
ε strain
ε_{50} strain corresponding to one-half the maximum principal stress difference
ϕ friction angle
ϕ resistance factor
ϕ_b resistance factor for flexure
ϕ_c resistance factor for compression
γ' average unit weight
η_h constant of horizontal subgrade reaction
λ slenderness parameter
λ_c column slenderness parameter
λ_p limiting slenderness parameter for compact element
λ_r limiting slenderness parameter for noncompact element
θ rotation
π pi (3.14159)

Units

in.	inches
ft	feet
k	kips (1000 lbs)
lbs	pounds
psi	pounds per square inch

CHAPTER 1

INTRODUCTION, PROBLEM STATEMENT, AND OVERVIEW OF SOLUTION

Introduction

The use of jointless bridges with pile supported integral abutments has become common practice in many states. In the absence of joints that allow movement due to thermal expansion and contraction without inducing additional stresses, the design of the pile-abutment system that supports the bridge must consider lateral load and deflection caused by temperature fluctuations. Load versus moment interaction must be considered when determining pile capacity.

Expansion and contraction of the superstructure caused by temperature fluctuation results in horizontal movement of the abutments supporting the ends of the superstructure. Passive soil pressure against the piles that support the abutments resists the horizontal movement, thereby inducing a horizontal shear force into the piles and the pile-abutment connection. In the presence of this induced shear force, the piles are subjected to a significant amount of bending stress. This dissertation investigates the behavior and design of steel H-piles surrounded by soil and subjected to relatively large bending and axial loads, simultaneously.

Statement of Problem

The typical design procedure for designing steel H-piles supporting integral abutments currently practiced by some states involves the use of computer software, such

as COM624P or LPILE, to obtain an approximate moment versus depth curve for each pile. From this curve, the locations of inflection points are determined, and the pile is designed as a column with an effective length equal to the distance between inflection points. This method fails to account for lateral support provided by surrounding soil, therefore yielding a very conservative solution. When sufficient lateral support is provided, the effective length of the column is reduced and the capacity is greatly increased. In the presence of continuous lateral support and a purely axial load, the capacity of the column is equal to the yield stress multiplied by the gross area.

Through the use of field research conducted at The University of Tennessee, in combination with finite element models, this dissertation research focuses on the development of a more accurate procedure for the design of steel piles supporting integral abutments. Specifically, the minimum amount of continuous lateral support required to prevent column buckling is determined to aid in selecting the appropriate load versus moment interaction curve to be used for the design of piles supporting integral abutments. The approach used to develop this more accurate design procedure is described in the following paragraphs.

Overview of Solution Process

Moment vs. Depth Prediction

Accurate prediction of the maximum moment present in the piles supporting a jointless bridge is both difficult to obtain and critical to the design of the piles. Research sponsored by the Tennessee Department of Transportation (TDOT) and conducted by

The University of Tennessee, Knoxville, provides a significant amount of data regarding the behavior of steel H-piles supporting integral abutments. Five separate test specimens, each including a concrete abutment supported on an HP10x42 pile and restrained against rotation, were used to obtain moment versus depth, load-deflection, and ultimate capacity data. Over 50 moment versus depth and load-deflection curves were generated. Comparing moment versus depth curves generated from LPILE with those obtained from field tests provides a means of validating the LPILE results. Varying boundary conditions are studied with an objective of determining the most appropriate application of LPILE to actual abutments.

Once the maximum moment is determined and the axial load on the pile is obtained, the designer can size the pile based on load-moment interaction. The only challenge remaining is choosing the appropriate load-moment interaction capacity curve that will accurately predict the true capacity of the pile.

Ultimate Capacity Field Tests

Two piles were tested to ultimate capacity in the research conducted in Tennessee. "Ultimate capacity" was defined as the condition at which additional lateral deflection of the abutment resulted in no additional moment experienced by the pile. The first pile tested to ultimate capacity, Pile 3, was driven into compacted fill, while the second, Pile 5, was driven into undisturbed clay typical to East Tennessee. The compacted fill was less stiff than the virgin clay. Significant cracking in the abutment supported by Pile 3 allowed rotation of the pile within the abutment. Therefore, the

connection of the pile to the abutment was no longer "fixed." This limited the ultimate capacity to a value less than the true capacity of the pile; the failure occurred in the abutment.

Stresses transferred from the pile to the abutment were reduced in Pile 5 by increasing the embedment depth of the pile into the abutment. The increased embedment depth allowed the connection between the pile and abutment to remain "fixed" throughout the duration of the test. Local buckling in the compression flange of the pile finally limited the ultimate capacity of the system.

The two ultimate capacity field tests produced two distinctly different modes of failure. Abutment failure, such as that with Pile 3, can be addressed by revising the design of the abutment, but is beyond the scope of this dissertation. Pile failure, as occurred with Pile 5, is more desirable due to easier predictability. Information gained from the two sets of field test data, along with finite element models and classical column equations, are employed later herein to more accurately predict the capacity of the pile.

Classical Column Equations

Designers typically predict the capacity of laterally loaded piles through the use of either AASHTO or AISC column design equations. The two methods are based on the same principles, but the AASHTO equations incorporate reduction factors that are integrated directly into the design equations, making the factors undetectable and, therefore, impossible to remove. AISC uses a more direct approach that involves calculating the true capacity of the member before applying the reduction factors. Thus,

the AISC equations, without the reduction factors applied, can be used to compare predicted capacity to field test data.

The theoretical ultimate capacity of a section, without consideration of length effects, is its "plastic limit." The plastic limit is equal to the plastic moment in pure bending and the yield axial load in pure compression. A stress diagram with the entire section experiencing the yield stress in tension or compression can be used to develop a plastic limit interaction curve by locating the neutral axis at various elevations within the section (Horne, 1979).

A moment versus depth curve, at failure, for Pile 5 is presented in Figure 1, while Figure 2 shows interaction curves calculated using AISC equations with an effective length equal to the distance between inflection points on the moment versus depth diagrams, and the plastic limit. Also plotted are the data points generated from the field test of Pile 5. The plot illustrates the inapplicability of the AISC equations to predict pile capacity when an effective length greater than zero is used. The true capacity of the pile is more closely predicted by the plastic limit curve. The results imply that sufficient lateral support is provided by the soil to prevent buckling. Not apparent, however, is the minimum amount of support required to prevent buckling.

Finite Element Buckling Model

Nonlinear buckling analysis can be used to predict the minimum soil stiffness required to prevent buckling. A preliminary model consists of 2-D structural surface effect elements overlaid onto 2-D plastic beam elements. Structural surface effect

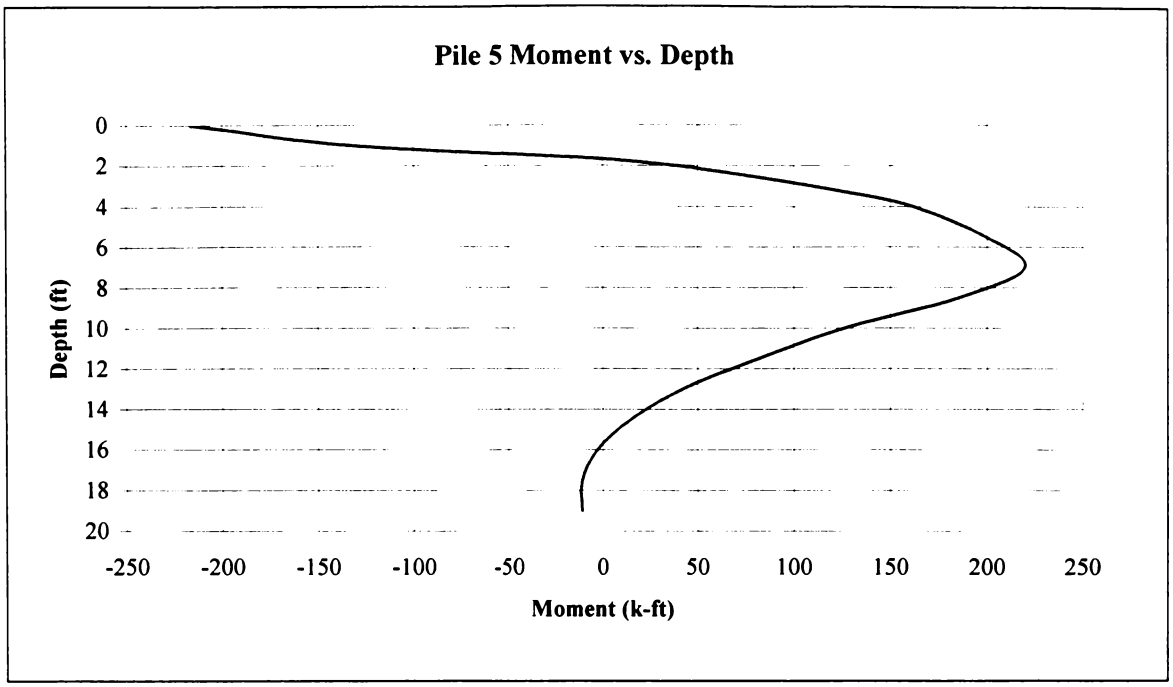


Figure 1: Final Bending Condition (Pile 5)

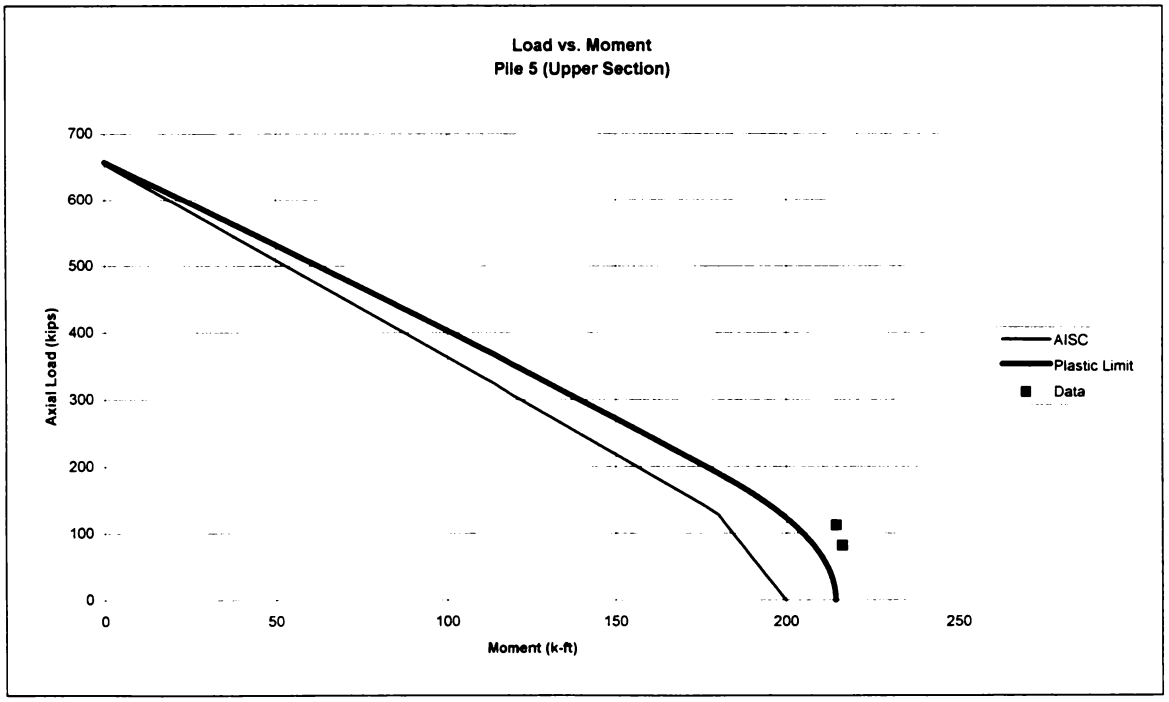


Figure 2: Interaction Curves (Pile 5)

elements are beam elements that allow surface pressure to be applied to plastic beam elements when the beam is deflected. The pressure may be limited to positive (compression) only, negative (tension) only, or both. Piles are typically subjected to only positive pressures from surrounding soil. Structural surface effect elements are limited to elastic behavior, which is not sufficiently accurate to represent soil behavior when drawing final conclusions. However, these elements do aid in creating a simplified preliminary model used for discovery purposes only. The plastic beam elements allow the use of non-elastic materials to represent the pile. An elastic modulus is used until the yield stress is achieved, at which time the modulus becomes zero.

Load is applied to the model in small increments until the solution begins to diverge. With automatic time stepping active, the load increment is bisected when the solution does not converge. The program then seeks a solution with the reduced load increment. This process continues until the minimum load increment, defined by the user, is achieved. To represent pile behavior, the lower end of the beam is pinned while the upper end receives an initial horizontal perturbation and is then deflected axially. A plot of axial load versus axial deflection illustrates the maximum axial load capacity of the pile for a given initial perturbation.

Figures 3 and 4 present theoretical axial load versus axial deflection curves for the HP10x42 obtained from the preliminary finite element model. The top of the pile is initially deflected 1 inch laterally and receives a moment of 104 k-ft. These values are typical for 1-inch lateral tests performed on Pile 5. The uppermost node is then deflected downward. Plotting axial load versus axial deflection, for the top node, reveals the axial

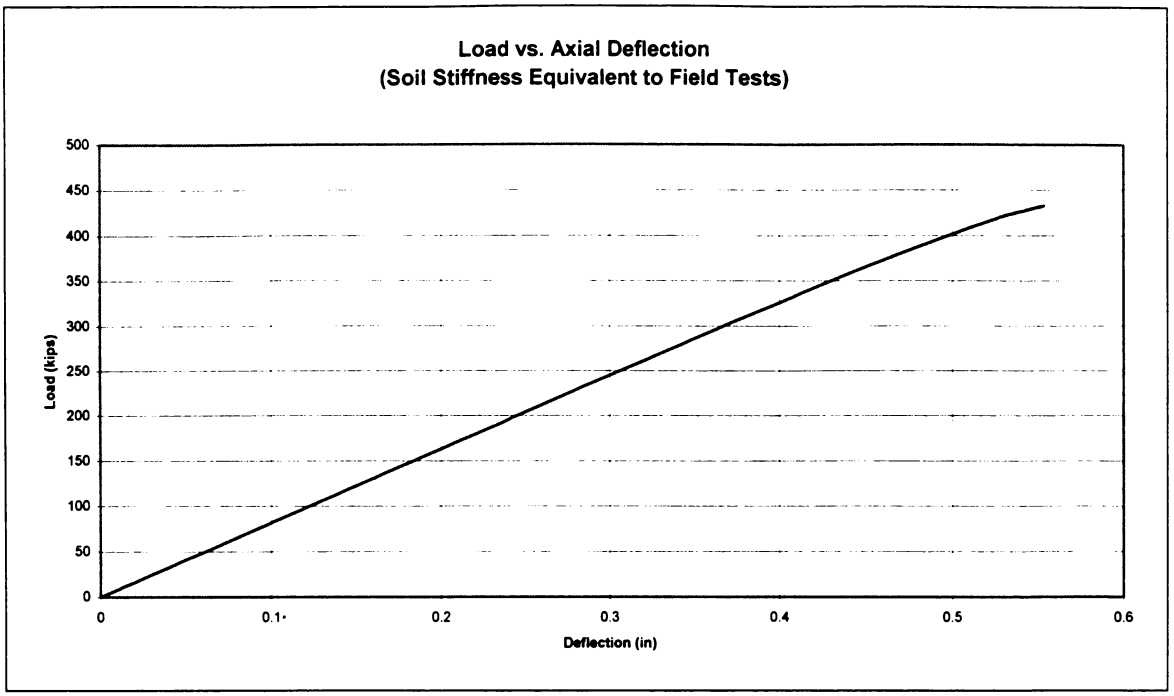


Figure 3: Axial Load vs. Axial Deflection (Pile 5 soil)

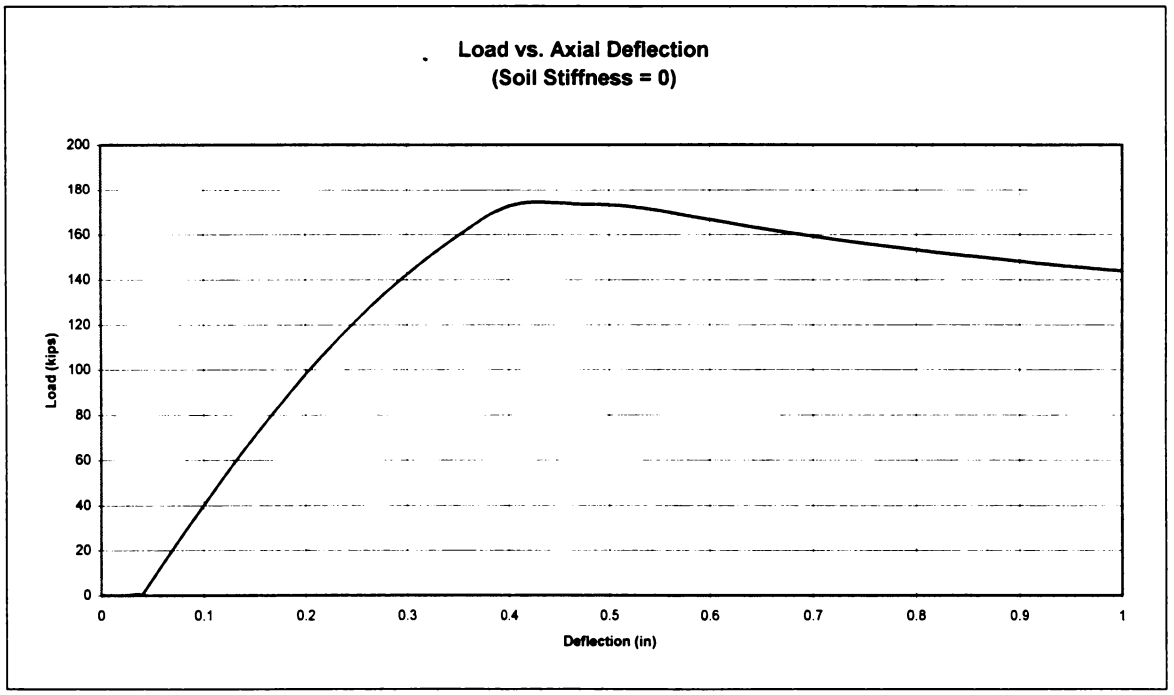


Figure 4: Axial Load vs. Axial Deflection (no soil)

capacity of the pile when subjected to the given conditions. Figure 3 represents the pile behavior when the stiffness of the surrounding soil is equivalent to that encountered in field tests of Pile 5. Figure 4 represents the pile behavior with no surrounding soil. Determining a value for the minimum soil stiffness required to prevent buckling under various initial conditions is the key to simplifying and improving the pile design process. The design of a pile in soil above the "minimum stiffness" would be equivalent to the design of a zero length column, therefore making possible the use of a single interaction curve per section.

Overview Summary

This dissertation provides a more accurate means of designing piles supporting integral abutments. Field test data provide information regarding moment distribution in the pile as well as horizontal load and deflection at the top of the pile. Field test data are also used to determine the appropriate application of LPILE. Finally, finite element models, used in conjunction with field test data, aid in determining soil stiffness requirements needed to provide continuous lateral support.

Objectives

This dissertation has three objectives. The first objective is to describe the results of the field tests, focusing on the behavior of the pile-abutment system under conditions simulating actual conditions in practice. The second objective is to evaluate the applicability of LPILE to the design of piles supporting integral abutments. The third

objective, the accomplishment of which is the primary focus of this dissertation, is to evaluate the buckling characteristics of piles supporting integral abutments. Recommendations for a more appropriate method of pile design evolve from the work on the third objective.

CHAPTER 2

REVIEW OF LITERATURE

The Practice of Jointless Bridge Construction

Kunin and Alampalli (2000) report on the results of a jointless bridge construction study initiated by the state of New York in 1996. Thirty-nine states and provinces in the United States and Canada responded to the survey, with only eight indicating no experience. The survey included information regarding the number of structures built, length of structures, and dates built. Information pertaining to the pile design approach used by each state was also obtained from the survey and is of particular relevance to the research presented herein. The report indicates that steel H-piles are the most commonly used form of support for jointless bridges. Nearly half of the responding states design the piles based solely upon axial loads. The remaining states design piles based on combined axial and bending analysis. Pile orientation was also evenly spilt, among the states responding, between strong axis and weak axis perpendicular to the direction of traffic. LPILE is the most common means of obtaining a lateral response for the piles. Details of how each state defines the interaction capacity of piles were not indicated in the study.

Wasserman (2001) justifies the use of jointless bridges based on performance and economics. In the absence of expansion joints, which are expensive to purchase, install, and repair, successive paving overlays can be accommodated without raising or replacing any joints. Other expensive items to purchase, install, and maintain on a typical bridge are the bearings. Integral abutments do not use typical steel, elastomeric, or Teflon

bearings that require regular maintenance. Performance advantages include increased design efficiency, increased redundancy, and enhanced load distribution at the girder supports. Wasserman also states that the use of jointless bridges aids in decreasing construction time and minimizing tolerance problems during construction. The design approach used by The Tennessee Department of Transportation is also discussed in detail by Wasserman, and is addressed in Chapter 5 of this dissertation.

Experimental Studies

Paduana and Yee (1974) present results from full-scale lateral load tests performed on three different sets of piles in California. The piles were located at three different bridge construction sites. Two sets of piles were steel pipe piles, and the third set were steel H-piles. The piles were loaded laterally before construction of the abutments and superstructure, and again after completion of the abutments and superstructure. The objectives of the research were to investigate the load-deflection behavior of the piles for comparison to theoretical results, and to determine the subgrade modulus. Results showed that for relatively small lateral displacements (0.25 in.) the lateral response of the pile-soil system could be reasonably approximated using a beam on an elastic foundation approach. More recent research conducted in Iowa and Tennessee expand on the concepts behind Paduana and Yee's work and include field test results for large deflections that cause inelastic behavior of the soil and the pile.

Design recommendations for piles supporting integral abutments are presented by Girton et al. (1991) based upon research conducted in Iowa. One of the goals of the

research was to validate assumptions regarding thermal expansion and abutment movement used in the design process. Piles supporting two different jointless bridges were instrumented and monitored. Each of the two bridges spanned approximately 320 feet. One of the bridges utilized prestressed girders, while the other bridge was a composite concrete deck, steel girder bridge. All piles were oriented such that bending was primarily induced about the weak axis. Recorded data included air temperature, longitudinal bridge displacement, and strain induced in the piles. Air temperatures at each bridge fluctuated over a total range of about 125 degrees Fahrenheit over the course of a one-year period. Results indicated a longitudinal displacement range for the abutments on both bridges of approximately +0.75 inches to –1.5 inches, with zero displacement occurring in the late spring (which is when the gages were zeroed) and again in the early fall. Data collected during this study support the currently used methods for calculating abutment movement.

Extensive research pertaining to the response of laterally loaded piles and the performance of abutments supported by these piles was conducted at The University of Tennessee (Burdette et al., 1999). Each test apparatus contained an abutment constructed atop a single HP10x42 pile that was driven to a depth of 38 feet. Five pile-abutment systems were tested during the research. A total of more than 60 lateral load tests were performed on the five systems. The test procedure used by the researchers in Tennessee is presented along with test results in Chapter 3 herein.

Anagnostopoulos and Georgiadis (1993) performed a series of laboratory experiments to investigate the effects of combined axial and lateral loads on pile

settlement. Results from this study indicate that pile settlement increases when the pile is subjected to a horizontal load in the presence of a substantial axial load. The increased settlement is caused by a change in the skin friction between the pile and soil, and not by a structural failure of the pile itself. This type of soil failure is beyond the scope of this dissertation, but should be considered when determining the bearing capacity of laterally loaded piles.

Modeling Lateral Soil-Pile Response

Ashour and Norris (2000) state that the soil-pile interaction response (p-y curve) is dependent upon both soil and pile properties. The behavior is a function of pile bending stiffness, cross-sectional shape, pile-head fixity, and pile depth (for short embedment depths). Therefore, results presented herein regarding the soil-pile interaction response of the field-tested piles are case specific. Altering of the pile properties or boundary conditions at the top of the pile may significantly change the characteristics of the soil response, which affects the distribution of lateral loads along the pile.

The most important soil parameter relevant to laterally loaded piles is defined by Reese and Van Impe (2001) as being the reaction modulus, which is the resistance (force) from the soil per displacement at a given elevation. The reaction modulus is a function of depth and pile deflection. In order to accurately model the response of laterally loaded piles, the reaction modulus must be well defined throughout the range of lateral displacement and depth of the pile. Reese and Van Impe suggest, based on field research,

that cyclic loading dramatically reduces the ultimate strength of soil, especially soil located below the water table. The research conducted by The University of Tennessee showed that moment versus depth curves for the laterally loaded test piles did not significantly change with repeated cycles, contradicting Reese and Van Impe's findings. The differing conclusions regarding the effects of cyclic loading suggest that cyclic behavior may be soil specific.

The conversion of the differential equation governing beam-column behavior into a finite difference form is also covered in Reese and Van Impe's book. The finite difference procedure is discussed in detail in Chapter 4, herein. Through the use of the finite difference approach, pile response can be estimated for a given set of p-y curves for the surrounding soil. LPILE, developed by Reese and Wang (1997), implements the finite difference approach to solve the differential equation based on p-y curves developed from field data.

Buckling in Elastic Continuum

Madhav and Davis (1974) utilize a finite difference approach to investigate the buckling of finite length beams in an elastic continuum. Assumptions made during this study included (1) homogeneous, isotropic, and elastic continuum, (2) elastic beam behavior, and (3) the fact that beam depth is negligible in the calculation of continuum displacements. For the specific case of laterally loaded piles, the validity of the first two assumptions is somewhat questionable. Piles supporting jointless bridges often experience lateral displacements large enough to cause inelastic soil and pile material

behavior. The work presented by Madhav and Davis strictly investigates the effects that the continuum has on the elastic stability of the finite length beam. Results are presented in the form of plots with a ratio of P_{cr} to P_{eu} (Euler buckling load) on the vertical scale and $k_r = E_p I_p / (E_s L^4)$ (where subscripts p and s correspond to pile and soil, respectively) on the horizontal scale. The test piles used by researchers in Tennessee corresponded to a k_r value of approximately 10^{-3} to 10^{-4}. Modhav and Davis's results indicate that P_{cr} is more than ten times P_{eu} for k_r values in the range experienced during the Tennessee research. Based on Modhav and Davis's work, it is apparent that sufficient lateral support was provided on the Tennessee test piles to prevent elastic stability issues. In addition, deflected shape plots from data obtained in Tennessee, which are presented later herein, suggest that additional length added to the piles should not affect the stability since pile displacement is essentially zero well above the base of the pile.

Buckling of Piles

A method for predicting the buckling capacity of axially loaded piles is developed and presented by Gabr et al. (1994) and Gabr et al. (1997). The presented method uses information regarding pile and soil properties to determine an effective length (L_e) that is then used to calculate P_{cr} based on Euler buckling theory. Nondimensional parameters used to determine the appropriate effective length are as follows.

$e = h / L$ (embedment ratio)

$\alpha = \sqrt[5]{\frac{\eta_h}{EI}}$ (coefficient of pile-soil compliancy)

$h' = \alpha h$ (nondimensional embedment length)

where L = total length of pile (in.)

h = length of pile embedded in soil (in.)

η_h = constant of horizontal subgrade reaction (lbs/in.^{3})

EI = flexural stiffness of pile (lb-in.^{2})

After calculating e and h', L_e' (nondimensional effective length) can then be obtained from nomographs developed by Gabr et al. (1994). Numerous nomographs are presented for various boundary conditions and values of the subgrade modulus power index (ω). After obtaining L_e', the effective length, L_e, is then calculated by dividing L_e' by α, and P_{cr} can then be calculated using Euler's buckling equation. Gabr's method is used in Chapter 7 to validate presented finite element results.

Analysis and Design of Laterally Loaded Piles

Various methods for designing integral abutment bridges and, specifically, the piles supporting the bridges are presented by Wasserman (2001) and Abendroth et al. (1989). Wasserman describes a design method that uses AASHTO column design equations to predict the capacity of laterally loaded piles. After calculating the plastic moment capacity of the pile and verifying that the pile-abutment connection is capable of resisting the pile's plastic moment, Wasserman models the lateral response of the pile using COM624P. The boundary condition used at the top of the pile includes the application of a lateral displacement equal to that calculated for thermal movement of the superstructure, and an applied moment equal to the plastic moment capacity of the pile. Points of inflection in the moment versus depth diagram are then determined from the

COM624P results. The pile capacity is then determined based on AASHTO interaction equations for a column having an effective length equal to the distance between inflection points. Failure is only considered about the axis perpendicular to the direction of load application (ie. the pile is considered continuously supported about an axis parallel to the direction of load). Wasserman only analyzes the portion of pile between the two inflection points, and neglects to investigate the possibility of pile failure above the uppermost inflection point. A more complete procedure would include the investigation of a second failure scenario that accounted for the possibility of pile failure occurring between the pile-abutment connection and the upper inflection point. However, when subjected to Wasserman's boundary conditions, the top of the pile experiences its plastic moment and therefore would have no remaining axial capacity. Also, this method for determining the capacity of the piles fails to consider support provided in the direction of lateral load application by soil pressure between inflection points, thus underestimating the buckling capacity of the piles.

Abendroth et al. (1989) suggest that a pile embedded in soil should be modeled as an equivalent cantilever. The behavior of a laterally loaded pile is described as involving a combination of material instability and geometric instability. Plastic collapse and elastic buckling are expressed as two extreme types of failure, while inelastic buckling occurs as a combination of inelastic strain and geometric instability. Abendroth et al. describes two design alternatives. The first method is based on elastic behavior, and failure is assumed to occur when the yield stress is achieved at any location along the length of the pile. The second method, which is more similar to Wasserman's method,

permits plastic redistribution of forces. Abendroth et al. compared results from finite element models of the equivalent cantilever system to AASHTO interaction curves for an HP10x42 bent about its weak axis. The models neglected the possibility of local buckling and lateral-torsional buckling. Results showed that AASHTO equations predict conservative values for axial capacity of the equivalent cantilever when KL/r values are relatively large. However, validation of the equivalent cantilever approach by comparison to full-length models was not included in the presented material. Also, when the equivalent cantilever approach is used, the pile is modeled as a cantilevered column without a surrounding continuum, a fact that raises questions about the validity of the method.

CHAPTER 3

DESCRIPTION OF FIELD TESTS

Field Tests

Researchers at The University of Tennessee began conducting field tests aimed at investigating the performance of laterally loaded piles supporting integral abutments in April of 1996. The tests continued through December of 1999. Five piles were tested during this period. All tests were conducted in Knox County, Tennessee at the intersection of Interstate 140 and Dutchtown Road on property made available by The Tennessee Department of Transportation.

The five piles tested are herein referred to as Pile 1, Pile 2, etc. in accordance with the chronological order of each pile tested. Each pile was driven approximately 38 feet into the ground and oriented such that bending was about the strong axis. An abutment consistent with the current design used in Tennessee was constructed atop each pile. Piles 1 thru 4 were embedded 1 foot into the abutment while Pile 5 was embedded 2 feet. A loading slab was cast monolithically atop each abutment to (1) provide support for additional ballast to increase axial load on the pile, (2) supply a location to apply lateral load, and (3) allow for the application of an eccentric vertical force used to control abutment rotation. Abutment and loading slab width was 6 feet for Piles 1 thru 3, and 10 feet for Piles 4 and 5.

The superstructure of an integral abutment bridge provides the abutment with rotational resistance through a fixed connection. In an effort to accurately model pile behavior, rotation of the test abutments was controlled using two different devices. Piles

1 thru 4 implemented a W18x106 reaction beam beneath the loading slab to control rotation, while a "hold-down" device constructed of two W14x61 cantilever beams connected to the loading slab and a tension bar anchored to a concrete slab was used for all tests, including an ultimate capacity test, on Pile 5 and for two ultimate capacity tests on Pile 3. Table 1 presents the dimensional information (including embedment depth into the abutment, abutment width, and beginning axial load) for each pile tested. Figures 5 and 6 illustrate the test setup using the reaction beam and "hold-down," respectively.

Also visible in Figures 5 and 6 are the details of the placement of the concrete ballast blocks, pull pad, pull frame, linear variable differential transformers (LVDT), and load cells. The concrete ballast blocks were constructed of normal weight concrete (approx. 145 pcf) and measured 24 x 30 x 72 inches. Each block weighed approximately 4360 lbs. Seven blocks were placed atop the loading slab to provide an additional 30.5 kips of axial load to the pile. The abutment and loading slab were constructed of reinforced concrete weighing approximately 150 pcf. An abutment and loading slab width of 6 feet provided an additional 36 kips of axial load while a width of 10 feet provided 60 kips. The "hold-down" device weighed approximately 3.1 kips.

Table 1: Field Specimen Specifics

Pile	Embedment Depth (ft)	Abutment Width (ft)	Initial Axial Load (kips)
1	1	6	66.5
2	1	6	66.5
3	1	6	66.5
4	1	10	90.5
5	2	10	93.6

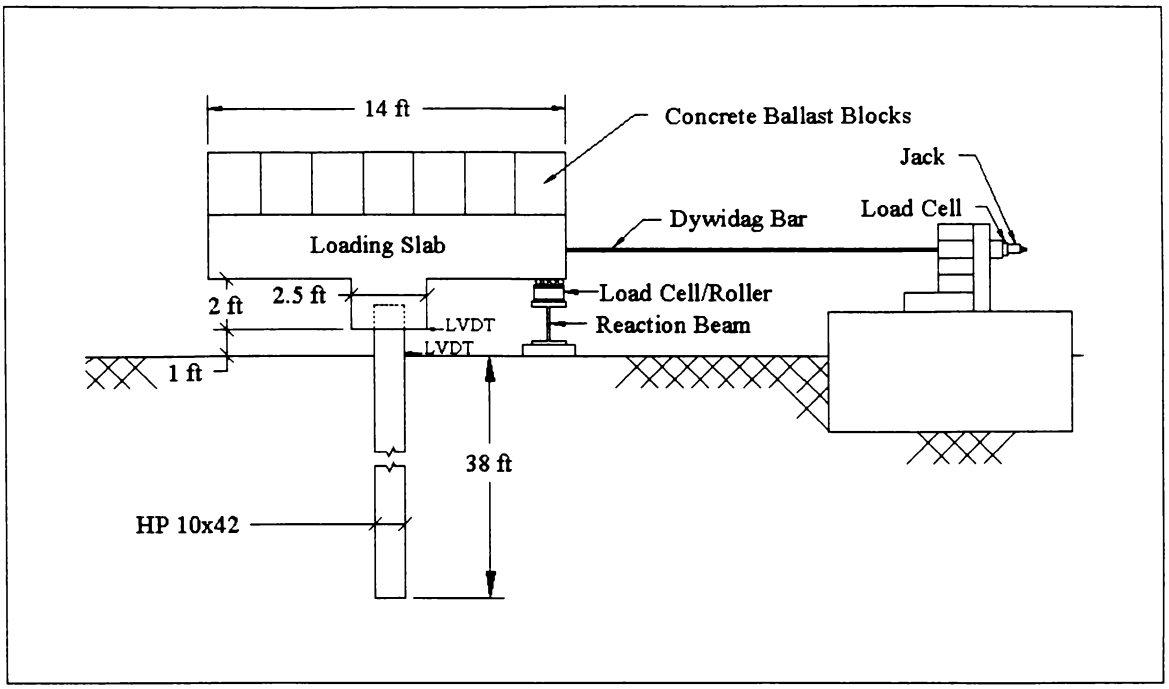


Figure 5: Field Test Setup (not to scale)

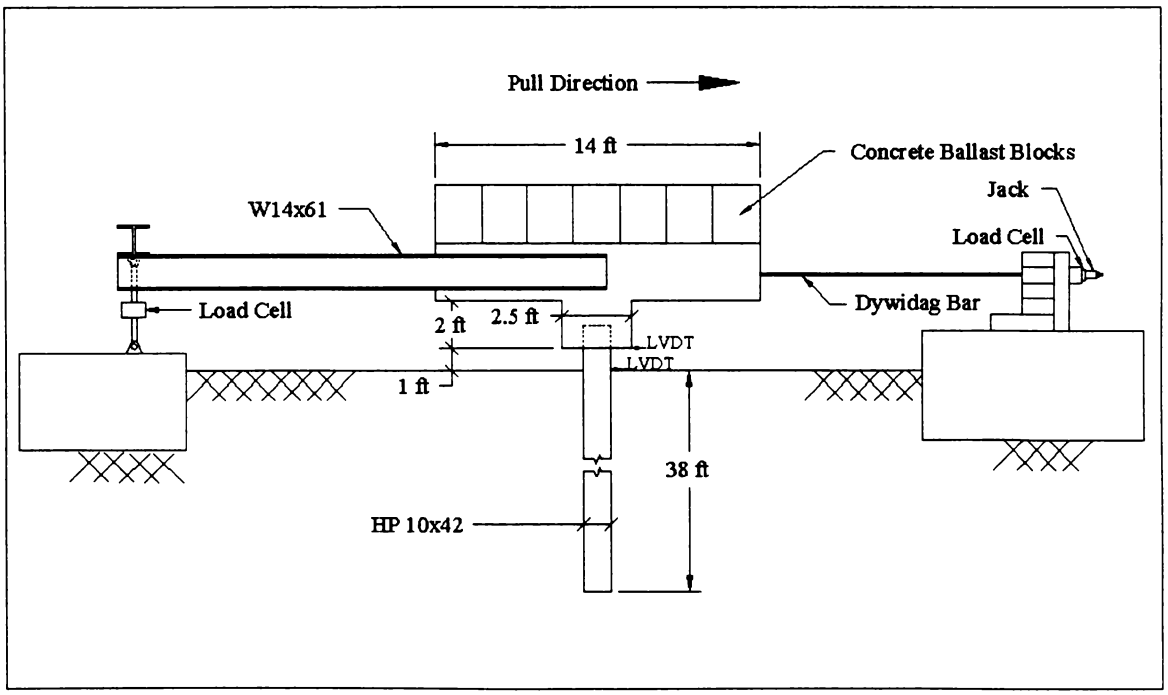


Figure 6: Hold-Down Field Test Setup (not to scale)

Instrumentation

Weldable strain gages were placed on the inside faces of each flange projection at various elevations on each pile. All gages were Hitec HEW-35-250-6's, which have a gage length of 0.25 inches and a resistance of 350 ohms. Two gages were placed on the compression flange and two on the tension flange at each elevation chosen. Vertical spacing between the groups of gages varied between 9 and 18 inches. The 9 inch spacing was used near the top of the piles where the moment gradient was high, while the 18 in spacing was used on the lower portion of the piles. Thin sheet metal was used to protect the gages during driving. Induced strain was only monitored in the upper 18 to 20 feet of each pile due to extremely low moments generated below 20 feet. The strain gages were zeroed prior to the start of each test. Therefore, only additional strain induced by lateral displacement of the abutment was measured. Initial axial strain at the top of the pile was obtained from statics prior to the start of each test. Sensotec pressure sensors were also placed on each flange at elevations ranging from 5 feet to 20 feet below the ground surface. A schematic of strain gage and pressure sensor locations along the length of the pile is presented in Figure 7.

RDP Electrosense type LDC3000A Linear Variable Differential Transformers (LVDTs) were used to monitor the lateral displacement of the system. One LVDT was placed on the pile directly above the ground surface, and a second was placed on the leading face of the abutment directly above the pile-abutment interface. A third LVDT was used in conjunction with a cantilevered arm bolted to the pile at the ground surface to monitor pile rotation at the ground elevation.

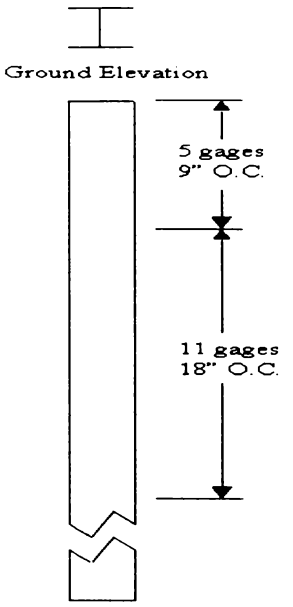


Figure 7: Gage Locations

Lateral load applied to the abutment and the resulting reaction load controlling abutment rotation were measured using 100 kip Interface load cells. For tests on Pile 5, all of which utilized the hold-down device, a 50 kip Interface load cell connected to the tension bar on the hold-down device replaced the 100 kip reaction load cell. The location of the lateral load with respect to the pile-abutment interface and the location of the vertical reaction force with respect to the neutral axis of the pile were noted. These distance measurements were used in conjunction with the measured loads to calculate the induced moment at the pile-abutment interface for the purpose of verifying results obtained from strain gage data.

All electronic data were collected using a MEGADAC 3108 with an expansion chassis, along with Optim's TCS software. This system allowed for monitoring of up to seventy-two channels, simultaneously. Data were collected from all strain gages, LVDTs, load cells, and pressure sensors at a rate of one sampling every two seconds (0.5 Hz).

Testing Procedure

Lateral load was applied such that a displacement rate of approximately 1 inch per 6 hours was achieved, thereby simulating the relatively slow expansion and contraction of a bridge superstructure with changes in temperature. The piles were pulled in one direction as follows: 3 separate tests to a maximum of 0.5 inch displacement at the ground surface followed by 3 separate tests to 1 inch displacement. The testing apparatus was then reversed and the same set of tests was repeated in the opposite direction.

Test Results

Each test produced data regarding moment versus depth for the upper 20 feet of pile, horizontal shear and rotation at the top of the pile, lateral load versus lateral displacement of the abutment, and interface soil pressure along the pile. A limited number of test results pertaining directly to this dissertation are presented herein. A more complete presentation of the field test results is presented in Behavior of Laterally Loaded Piles Supporting Bridge Abutments (Burdette et al., 1999).

Ultimate Capacity Hold-Down Test Description

Prior to May of 1999, all tests performed involved laterally loading the test abutment until a predetermined pile deflection was reached. Rotation of the abutment was eliminated in previous tests through an eccentric upward reacting force. This setup was adequate to control abutment rotation, but the upward force effectively reduced the axial load on the pile. Since an axial load representative of service loads was desired when testing the system to extreme deflections, an alternative method of controlling abutment rotation was designed. The new apparatus consisted of two cantilever beams extending from the abutment opposite the direction of the lateral load. A simply supported cross beam which spanned between the two cantilever beams was anchored to a concrete pad through a tension bar with pinned ends. When the abutment was loaded laterally, a downward reacting force resisted rotation of the abutment. This device, referred to as the "hold-down" device, controlled rotation while adding axial load to the pile. Figure 6 illustrates the hold-down device. Four strain gages were attached to the hold-down bar on Pile 3 to determine the force applied to restrain abutment rotation. These strain gages were replaced by a load cell prior to the testing of Pile 5. The remainder of the test setup was identical to the setup previously described herein with the exception of the absence of the reaction beam and load cell.

The objective of the hold-down tests was to show that the pile had the capacity to support the service axial load and a significant bending moment simultaneously. The hold-down tests were run in a similar manner to the previous tests. Without a predetermined ultimate deflection, time of testing could not be calculated prior to running

the test. This caused concern that the previously used load rate would create a test duration which was longer than the hours of light in a day. To avoid testing in the dark, the hold-down tests were performed at a deflection rate of 0.25 inch increments at 15 minute intervals. The tests were begun with zero lateral load and zero load in the hold-down bar. Testing was continued until additional deflection of the abutment produced no additional moment in the pile, or until significant cracking of the abutment occurred. Due to the balancing of all strain gages before starting the test, it became necessary to calculate the initial strain conditions in order to know when the pile reached its yield strain during the test. Dead load of the abutment and hold-down device, as well as moment induced by the eccentricity of the cantilever arms, were accounted for.

Axial load and moment at the pile-abutment interface were calculated using data collected from strain gages at that location. A strain diagram of the cross section was generated from the summation of initial strain and induced strain. The strain diagram was then used in conjunction with the yield stress and modulus of elasticity, which were determined from coupon tests, to develop a stress diagram. From the stress diagram, the axial load and moment were calculated and compared to values obtained through statics from the load cell data. Due to gage failures, all hold-down results at the pile-abutment interface for Pile 5 are based solely on statics.

Ultimate Capacity Hold–Down Test Results

Pile 3 Results

Pile 3 consisted of a 6 foot wide abutment with a pile embedment depth of 1 foot. The pile was driven 38 feet into engineered fill material which produced a relatively low lateral stiffness of approximately 30 kips/in. at 1 inch of lateral displacement. Abutment concrete strength was 5900 psi (tested), and the theoretical plastic moment capacity was 181.1 k-ft. On May 10,1999, the first hold down test was performed on Pile 3. Initial load conditions on the pile included an axial load of 68.5 kips and a moment at the top of the pile of 37 k-ft. The top of the pile was displaced laterally 2.3 inches, generating a total axial load of 74 kips and a total bending moment at the top of the pile of 169 k-ft. The test was stopped due to lack of increase in moment or axial load during the last deflection increment. A second hold down test was performed on Pile 3 on June 1, 1999. At a deflection of about 2 inches, a crack in the abutment was noticed. Testing continued to a deflection of 4.1 inches with a significant increase in cracking along the way. Due to the cracking, the ability to directly transfer moment from the abutment to the pile through a fixed connection was lost. This condition led to a lower moment at the top of the pile than had been generated during the previous test. However, at a deflection of 4.1 inches, the abutment proved capable of carrying the applied load despite significant cracking.

Pile 5 Results

Pile 5 consisted of a 10 foot wide abutment with a pile embedment depth of 2 feet. The pile was driven 37 feet into undisturbed soil which produced a high lateral

stiffness of approximately 60 kips/in at 1 inch of lateral displacement. Abutment concrete strength was 3800 psi, and the theoretical plastic moment capacity was 214.1 k-ft. Following the final 1 inch test on Pile 5, some settlement of the pile occurred before the pile again became stable. The settling of the pile, which was caused by a soil bearing failure as described by Anagnostopoulos and Georgiadis (1993), reduced the amount of pile exposed between the ground and the bottom of the abutment from 1 foot to about 4 inches, making placement of an LVDT at the ground elevation on Pile 5 impossible. Therefore, deflections during the hold-down test were measured at 1 inch above the base of the abutment. The test began with no load in the hold-down bar or the lateral load bar and without the presence of the ballast blocks atop the abutment. This generated an initial load condition on the pile that consisted of 61.6 kips axial load and 44.6 k-ft of moment. At a deflection of 2.4 inches, an additional 168.0 k-ft of moment and 20.3 kips of axial load had been induced in the pile directly below the bottom surface of the abutment. This generated a total load condition in the pile of 81.9 kips axial load with a 212.6 k-ft moment. Then, 30.5 kips of axial load was added to the pile by placing the ballast blocks on top of the abutment. The additional axial load to the pile caused the total moment to drop, as expected, to 198.6 k-ft with no additional deflection. The test was then continued to a deflection of 4.3 inches with a maximum total moment of 214.5 k-ft with 112.1 kips of axial load. At this time, local flange buckling occurred in the compression flange and the test was stopped. The abutment remained intact and showed no significant signs of failure. One vertical crack in the abutment occurred on the opposite side to the direction of lateral load at a deflection of approximately 1 inch. The

crack was monitored thoughout the remainder of the test and did not grow, open, or lead to other cracks.

CHAPTER 4

APPLICABLE USES OF LPILE

This chapter is a slightly revised version of a paper titled "A Comparison of Measured Bending Moments in Laterally Loaded Piles With Bending Moments Calculated With LPILE" written by Earl Ingram, Edwin Burdette, David Goodpasture, Hal Deatherage, and Chris Myers. The paper was presented by Earl Ingram at the 2002 Transportation Research Board Annual Meeting.

Ingram, Earl E., Burdette, Edwin G., Goodpasture, David W., Deatherage, J. Harold, and Christopher A. Myers, "A Comparison of Measured Bending Moments in Laterally Loaded Piles With Bending Moments Calculated With LPILE," 81st Annual Meeting CD-Rom, Transportation Research Board, TRB 02-2777, 2002

My primary contributions to the paper included (1) participation in field data collection, (2) running the LPILE analyses, (3) interpretation of LPILE results, and (4) most of the writing.

Objective

The objectives of this chapter are (1) to present some typical pile bending moment diagrams for laterally loaded piles in stiff clay, (2) to compare these moments to moments calculated using LPILE, and (3) to illustrate the effects of varying boundary conditions and input soil parameters on the calculated moments. Data from three HP10x42 piles included in the field tests discussed in Chapter 3 are used for comparisons with LPILE calculations.

Description of LPILE

LPILE is a special purpose computer program for analyzing laterally loaded piles and drilled shafts. This program uses a finite difference approach to solve the differential equation for a beam-column while taking into account the nonlinear soil response. The

behavior of the pile material is assumed to be elastic. The pile is assumed to be straight with a uniform cross-section and to have a longitudinal plane of symmetry in which loads and reactions lie. Only bending deformations are considered.

LPILE Plus 3.0 can approximate appropriate p-y curves based on user input soil information, or the user can choose to define case specific p-y curves. The most practical approach to using LPILE by a bridge designer is to allow LPILE to choose an appropriate set of p-y curves based on user input soil properties. The required user input soil information includes (1) soil type, (2) shear strength (c), (3) internal friction angle (ϕ), (4) strain corresponding to one-half the maximum principal stress difference (ε_{50}), and (5) unit weight.

Nine different types of soils are included in LPILE's internal database, including stiff clay with free water and stiff clay without free water. The LPILE Plus 3.0 user's manual explains that the stiff clay with free water option is intended for cases where water exists above the top layer of soil (ie. piles driven off-shore). Therefore, "stiff clay without free water" is the appropriate choice for modeling piles driven into stiff clay on dry land.

The field tests conducted in Tennessee (described in Chapter 3) utilized piles driven into stiff clay without free water. When the LPILE user describes the soil as stiff clay without free water, LPILE calculates p-y curves using the following equations that were developed by Welch and Reese (1972) based on experimental data collected in Houston, Texas.

$$p = 0.5 p_u \left(\frac{y}{y_{50}} \right)^{\frac{1}{4}}$$

where: y = lateral displacement

$y_{50} = 2.5\ \varepsilon_{50}\ b$

b = width of pile

p_u is taken as the smaller of the values given by the following two equations.

$$p_u = \left[3 + \frac{\gamma'}{c} x + \frac{J}{b} x \right] cb$$

$$p_u = 9cb$$

where: γ' = average unit weight

x = depth from ground surface

c = shear strength at depth x

J = 0.5

Beyond a lateral deflection equal to $16y_{50}$, p is taken as p_u for all values of y.

Four options for the boundary conditions at the top of the pile are available in LPILE. The user may input shear and moment, shear and slope, shear and rotational stiffness, or deflection and moment at the top of the pile. Field test data provided shear, moment, and deflection data. Slope data were also collected but not used due to a large amount of variation between tests. This variation led researchers to question the accuracy of the slope data.

Comparison of Field Data to LPILE Predictions

LPILE was used to generate two moment versus depth curves for each of the three piles considered in this chapter. Each pile was modeled from the ground elevation to the bottom tip of the pile. The deflection-moment boundary condition was used to generate the first curve, while the shear-moment boundary condition was used to generate the second. If the soil data input into LPILE and the shear, moment, and deflection data obtained from the field tests were perfectly accurate, the two different sets of input boundary conditions should produce the same moment versus depth curve.

Soil data obtained for each of the test piles were somewhat limited. Pile 1 data included, for one elevation, shear strength, unit weight, and the strain corresponding to one-half the maximum principal stress difference (ε_{50}). These data are not sufficient to create a profile of the soil along the length of the pile. However, the data are sufficient to produce a reasonably accurate moment versus depth curve using LPILE. Figure 8 presents two moment versus depth curves generated from LPILE for Pile 1. The first curve was generated using deflection and moment at the top of the pile as the upper boundary condition, while the second curve was generated using shear and moment at the top of the pile as the upper boundary condition. The difference in the two moment versus depth curves generated using two different boundary conditions is indicative of an inaccurate or incomplete soil profile. Soil data for Piles 4 and 5 consisted of shear strength and unit weight values at four different elevations in the upper 12 ft. of the pile. Approximate values for ε_{50} were estimated based on tables provided in the LPILE technical manual. Figures 9 and 10 show that a more complete soil profile aids in

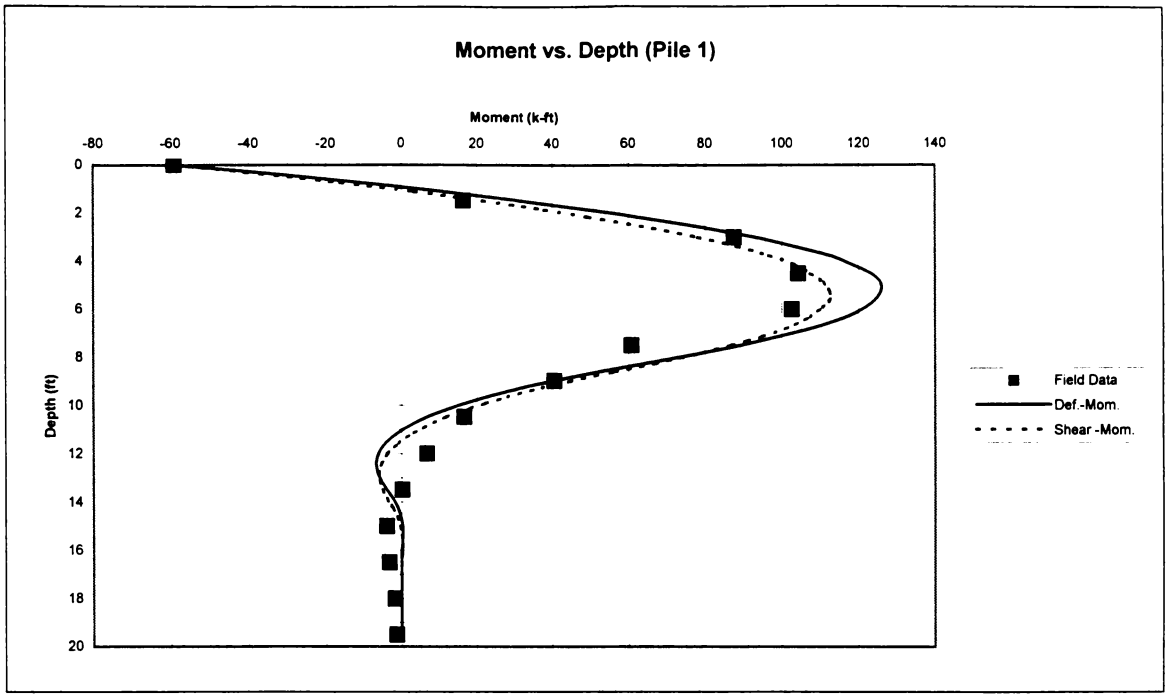


Figure 8: Moment vs. Depth (Pile 1)

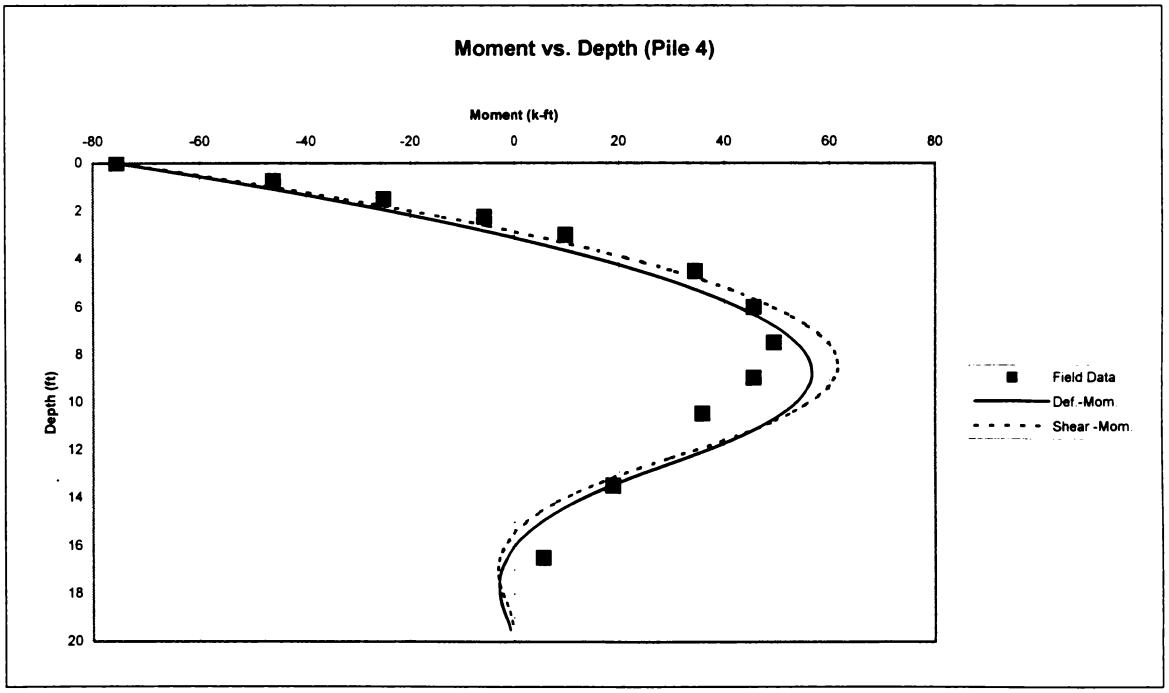


Figure 9: Moment vs. Depth (Pile 4)

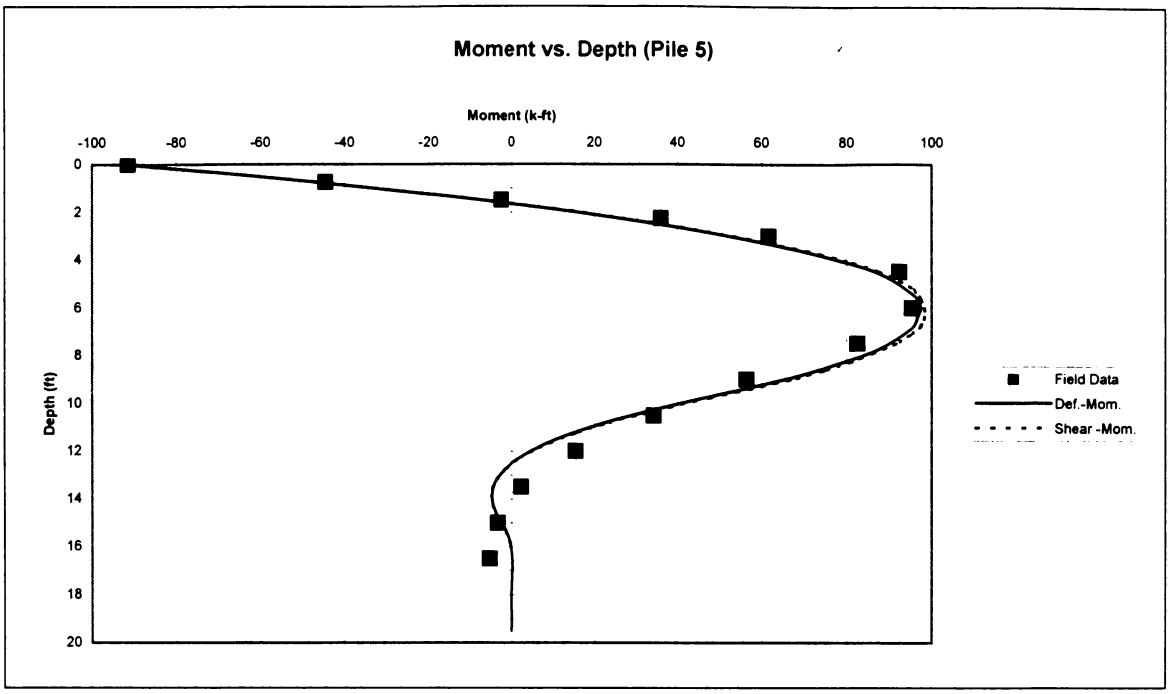


Figure 10: Moment vs. Depth (Pile 5)

narrowing the gap between the moment versus depth curves generated from the two different sets of boundary conditions.

Figures 8 thru 10 illustrate the ability of LPILE to reasonably estimate the moment versus depth curve for a given pile when the boundary conditions are well known. Unfortunately, during the design phase of an integral abutment bridge, the moment and the shear at the top of the pile are not known; rather, these values need to be determined from LPILE. One possible means of obtaining these values from LPILE is to use the shear-rotational stiffness boundary condition. The shear value input into LPILE must then be adjusted until the desired displacement is achieved. Once the designer has determined the correct shear value, the corresponding moment diagram, including the moment at the top of the pile, should accurately represent the pile behavior.

The rotational stiffness at the ground elevation for Pile 5 was estimated to be 8300 k-ft./rad. by dividing moment data by rotation data obtained from field tests. This value was used to model the pile using the shear-rotational stiffness boundary condition. The shear value was adjusted until the displacement matched that obtained from the field data. The resulting moment versus depth curve is presented in Figure 11. It is also noted that the input shear value did not vary significantly from the shear value obtained from the field data.

Limited Sensitivity Study

A limited sensitivity study was performed to illustrate the effects of error in input data when using LPILE. Rotational stiffness, shear strength, and ε_{50} were analyzed in the sensitivity study. The shear-rotational stiffness boundary condition was used to generate moment versus depth curves for each of the studies. Input shear values were adjusted for each test in order to maintain a constant displacement of 1 inch. The "baseline" curve was generated using a single layer soil profile with a shear strength value of 25 psi, an ε_{50} of 0.010, and a pile rotational stiffness of 8300 k-ft./rad at the ground elevation.

Figure 12 illustrates the effects of varying the rotational stiffness of the pile-head. As rotational stiffness is increased, the required shear to produce a given displacement and the resulting moment at the top of the pile are also increased. The inverse is true when rotational stiffness is decreased. A 50% increase in rotational stiffness resulted in

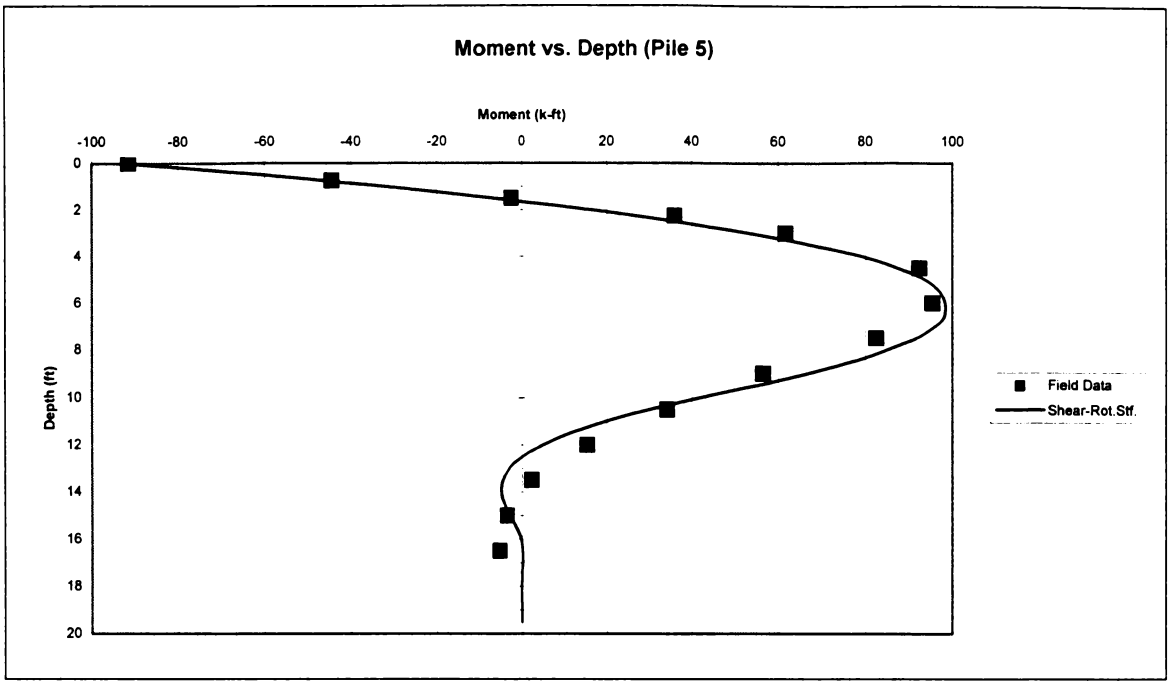


Figure 11: Moment vs. Depth (Pile 5), Shear-Rotational Stiffness Boundary Condition

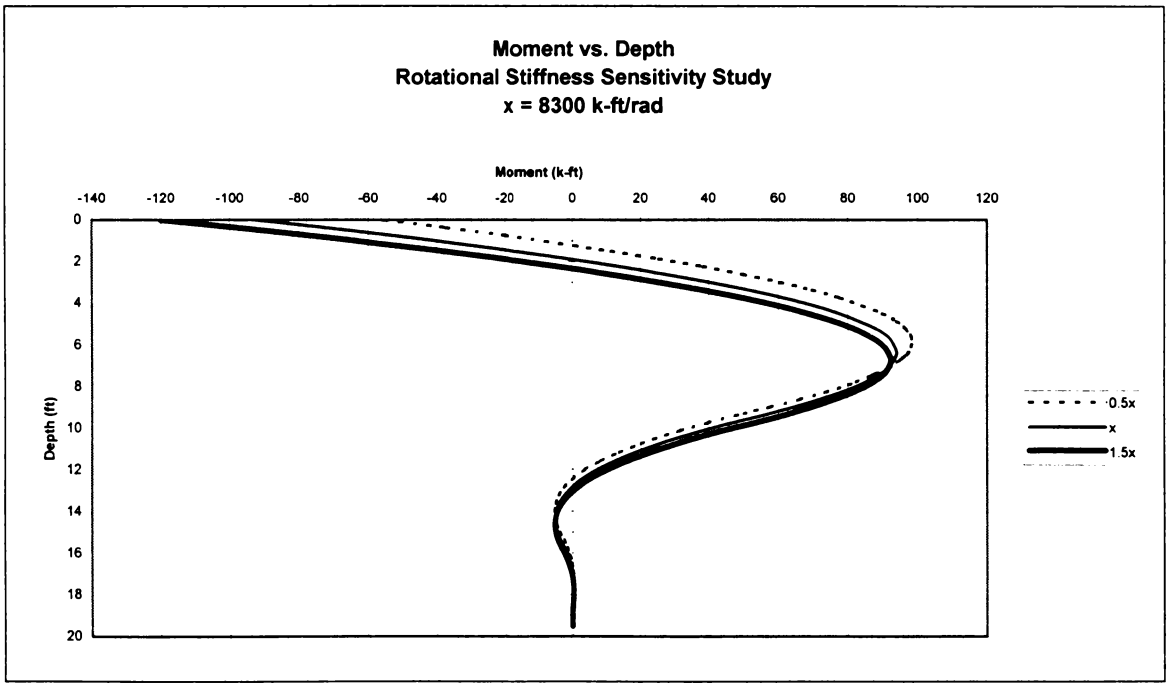


Figure 12: Rotational Stiffness Sensitivity Study, x = 8300 k-ft/rad

an 8% increase in shear and a 30% increase in moment at the top of the pile while the magnitude of the maximum moment below the surface decreased 2%.

The effects of shear strength variation are presented in Figure 13. As the shear strength of the soil is increased, the resulting shear produced by a given displacement and the resulting moment at the top of the pile are again increased. However, in this case the maximum moment below the ground surface is more strongly affected than is the moment at the top of the pile. A 40% increase in soil shear strength resulted in a 25% increase in shear. The moment at the top of the pile was only increased 9% while the magnitude of the maximum moment below the surface increased 17%.

The effects of variations in ε_{50} are presented in Figure 14. A 50% decrease (stiffening) in ε_{50} produced little change in the maximum moments but caused a 12% increase in the shear force required to displace the top of the pile 1 inch. The moment at the top of the pile and maximum below ground moment increased 5% and 8%, respectively.

Conclusion

The ability of LPILE to predict the behavior of laterally loaded piles has been illustrated through the use of comparisons to collected field data. When soil properties and the boundary conditions at the top of the pile are known, reasonably accurate results can be obtained. While the horizontal shear at the top of the pile is typically not known, a reasonable approximation of rotational stiffness can be made by modeling the superstructure with pinned ends and applying a moment at the end of the bridge. The

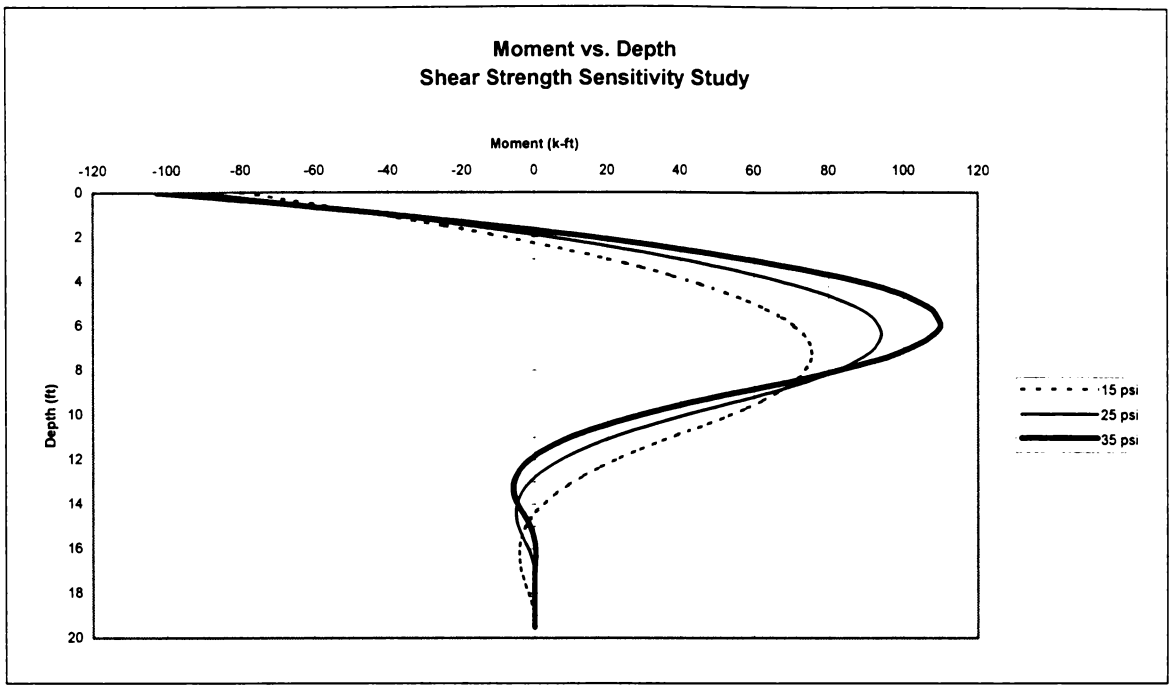


Figure 13: Shear Strength Sensitivity Study

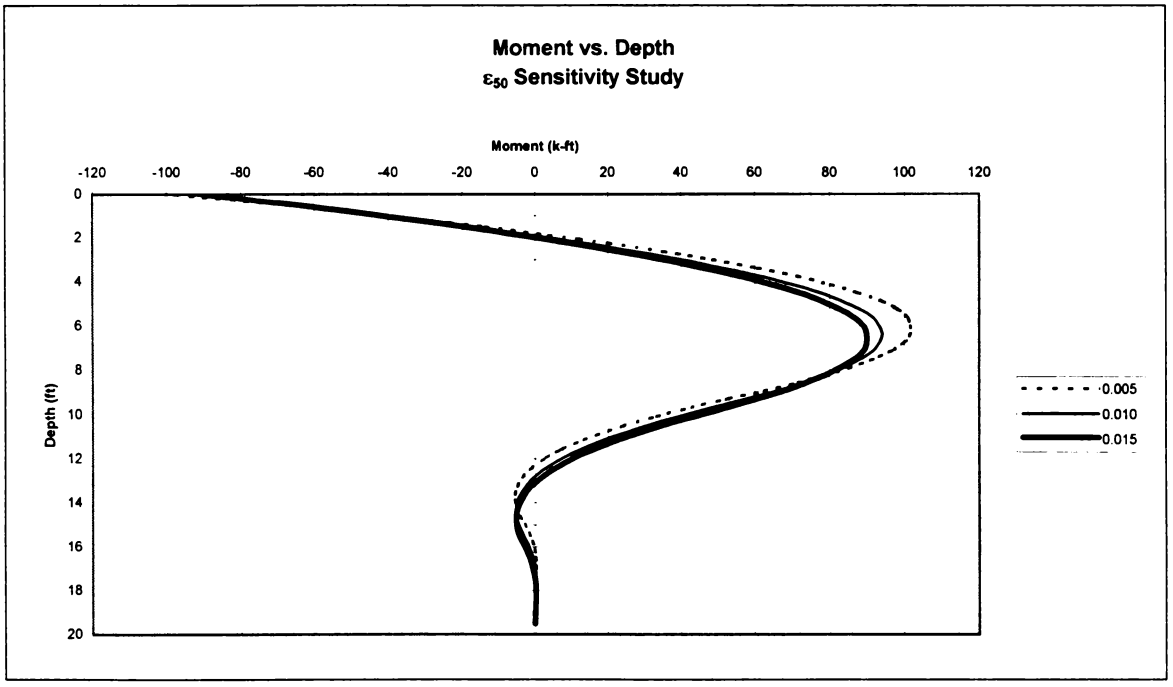


Figure 14: ε50 Sensitivity Study

approximate rotational stiffness of the abutment is equal to the applied moment divided by the resulting rotation. From this approximate value and a known value of horizontal deflection, the value of shear can be approximated through iteration. Thus, approximate but realistic values of boundary conditions can be obtained.

The complex interaction between lateral displacement of the bridge abutment and nonlinear soil response creates a loading condition on the piles supporting the abutment that cannot be reasonably calculated by hand. Provided with a relatively accurate rotational stiffness for the pile connection and proper soil data, LPILE can be used to predict reasonably accurate response for a given lateral displacement.

The following chapters in this dissertation address the analysis and design of piles supporting integral abutment bridges. Appropriately used, LPILE can provide reasonable values of lateral load and moment for use in the design of piles.

CHAPTER 5

TYPICAL COLUMN DESIGN EQUATIONS RELATED TO LATERALLY LOADED STEEL H-PILES

This chapter is a slightly revised version of a paper titled "Evaluation of Applicability of Typical Column Design Equations to Steel H-Piles Supporting Integral Abutments" written by Earl Ingram, Edwin Burdette, David Goodpasture, and Hal Deatherage. The paper was submitted to the American Institute of Steel Construction for publication, but has not been accepted at the time of completion of this dissertation.

My primary contributions to the paper included (1) participation in field data collection, (2) reduction of field data, (3) generation of AASHTO, AISC, and Plastic Limit interaction curves, and (4) most of the writing.

Introduction

The purpose of this chapter is to address the question of how well the American Association of State Highway and Transportation Officials (AASHTO) and American Institute of Steel Construction (AISC) column design equations apply to the design of laterally loaded piles. While neither Standard Specifications for Highway Bridges nor Load and Resistance Factor Design (LRFD) specifically addresses the design of laterally loaded piles, both codes address the design of columns subjected to combined axial and bending loads.

American Association of State Highway and Transportation Officials (AASHTO)

Section 10.54.2 of AASHTO's Standard Specifications for Highway Bridges, "Combined Axial and Bending," has been used by some states to determine the capacity of piles supporting integral abutments. If the piles are situated such that bending induced

by thermal movement is about the strong axes, a pile is considered continuously supported by soil along its weak axis, and supported at points of inflection in the strong axis direction. Therefore, buckling of the pile will occur about the strong axis, with the column length being determined by the distance between inflection points in the moment diagram. This method for determining the capacity of the piles fails to consider support provided in the strong axis direction by soil pressure between inflection points, thus underestimating the buckling capacity of the piles.

The final bending condition presented for Pile 5 in Figure 1 indicates that two possible buckling scenarios need to be investigated if the AASHTO equations are to be used. The first inflection point consistently occurred approximately 1.75 ft. below the bottom face of the abutment, while the second occurred approximately 14 ft. below the first. Thus, two column sections must be analyzed: one above the upper inflection point, and another between the two inflection points. Extremely large moments induced at the bottom face of the abutment in the presence of the maximum axial load on the pile create the need to investigate the upper section of the pile, despite its short effective length. The axial load on the pile at the lower column section is somewhat less due to skin friction. However, due to the lack of knowledge concerning the amount of axial load supported through skin friction above the first inflection point, each of the two column sections is considered to carry the applied axial load in full.

The following is a summary of how the interaction diagrams were developed for Pile 5. Sheet metal shielding welded to the pile in an effort to protect the attached strain gages during pile driving caused a change in the cross-sectional properties of the pile.

Table 2: Section Properties

	HP10x42	Modified HP10x42
A (in^2)	12.4	13.8
I (in^4)	210	226.5
S (in^3)	43.4	46.7
Z (in^3)	48.3	52.9

The lower column section was shielded over its entire length, while the majority of the upper column section remained unshielded. A brief summary of the pertinent section properties for each column section is tabulated in Table 2.

Article 10.54.2.1 requires that equations (10-155) and (10-156) be satisfied if the applied axial compressive force is in excess of $0.15F_yA$. (If P is less than $0.15F_yA$, Article 10.48.2.1 indicates that the pile has a bending capacity of M_u.)

$$\frac{P}{0.85A_sF_{cr}} + \frac{MC}{M_u\left(1-\frac{P}{A_sF_e}\right)} \le 1.0 \qquad (10\text{-}155)$$

$$\frac{P}{0.85A_sF_{cr}} + \frac{M}{M_p} \le 1.0 \qquad (10\text{-}156)$$

Setting each of the two above equations equal to 1.0, and then solving for M, provides a means of developing an interaction curve for a given pile.

$$M = \left[\frac{M_u\left(1-\frac{P}{A_sF_e}\right)}{C}\right]\left(1.0-\frac{P}{0.85A_sF_{cr}}\right) \qquad (A)$$

$$M = M_p\left(1.0-\frac{P}{0.85A_sF_{cr}}\right) \qquad (B)$$

The maximum allowable moment for a given axial load P is the smaller value of M obtained from the two equations above.

M_u = maximum bending strength as defined in Section 10.48;

$M_p = F_yZ$, the full plastic moment of the section;

C = equivalent moment factor (conservatively taken as unity);

A_s = gross effective area of the column cross section;

$$Fe = \frac{\pi^2 E}{\left(\frac{KL_c}{r}\right)^2} = \text{Euler Buckling stress in the plane of bending} \qquad (10\text{-}157)$$

F_{cr} = buckling stress determined by Equations (10-151) and (10-153)

For $\frac{KL_c}{r} \le \sqrt{\frac{2\pi^2 E}{F_y}}$

$$F_{cr} = F_y\left[1 - \frac{F_y}{4\pi^2 E}\left(\frac{KL_c}{r}\right)^2\right] \qquad (10\text{-}151)$$

For $\frac{KL_c}{r} > \sqrt{\frac{2\pi^2 E}{F_y}}$

$$F_{cr} = \frac{\pi^2 E}{\left(\frac{KL_c}{r}\right)^2} \qquad (10\text{-}153)$$

AASHTO instructs that the effective length factor K shall be equal to 0.875 for a column with pinned ends. The top of the pile moves laterally with respect to the first inflection point, but is restrained against rotation by the abutment; therefore, an effective length factor of 2 x 0.875 = 1.75 is used when analyzing the upper portion of the pile. The

section of pile between the two inflection points is considered pinned at each end, yielding an effective length factor of 0.875. Since buckling is being considered about the strong axis, r_x is deemed the appropriate value of radius of gyration to be used in all calculations.

With a yield stress of 53.2 ksi, which was obtained from coupons taken from Pile 5, the HP10x42 fails to meet the compact section requirements of Article 10.48.1. Therefore, M_u must be determined from Article 10.48.2, which defines the maximum bending strength as:

$$M_u = F_y S \tag{10-98}$$

where S is the section modulus.

The value calculated in Equation (10-98) is commonly known as the yield moment, M_y. Requirements listed in Article 10.48.2.1 must be satisfied before utilizing equation (10-98). Article 10.48.2.1 is divided into four parts, (a) through (d).

(a) Projecting compression flange element

$$\frac{b'}{t} \leq \frac{2200}{\sqrt{F_y}} \tag{10-99}$$

(NOTE: F_y is in units of psi)

where $M < M_u$, b'/t may be increased by the ratio $\sqrt{M_u/M}$

b' is defined as the width of the projecting flange element.

$$b' = \frac{b_f - t_w}{2}$$

Since the compression flange fails to meet the requirements of equation (10-99), the maximum value of M, such that the following equation is satisfied, must be determined.

$$\frac{b'}{t} \leq \frac{2200}{\sqrt{F_y}} \sqrt{M_u / M}$$

Setting the two sides equal and solving for M yields

$$M = M_u \left(\frac{2200t}{b'\sqrt{F_y}} \right)^2 \qquad \text{(C)}$$

From equation (C), the maximum bending strengths for the upper and lower sections of Pile 5 are determined to be 132.4 k-ft. and 142.4 k-ft, respectively. These are the appropriate values for M_u to be used in equation (10-155).

(b) Web thickness

The HP10x42 satisfies the web thickness requirements of part (b).

(c) Spacing of lateral bracing for compression flange

Since the pile is assumed to be fully braced in the weak axis direction, $L_b = 0$.

Therefore, part (c) is satisfied.

(d) Maximum axial compression

$$P \leq 0.15 F_y A \qquad \text{(10-102)}$$

Equations (10-155) and (10-156) must be satisfied if P exceeds $0.15F_yA$.

The interaction diagrams for each of the two sections of pile can now be developed. When the axial compressive force is less than $0.15F_yA$, the allowable moment is equal to M_u (132.4 k-ft. for the upper section, and 142.4 k-ft. for the lower section). Otherwise, the allowable moment is the smaller of the two values obtained by Equations (A) and (B).

The interaction diagrams resulting from the appropriate application of Equations (A) and (B) are plotted in Figures 15 and 16. The AASHTO interaction diagram for the upper section of Pile 3 is presented in Figure 17. Pile 3 had a yield stress of 45 ksi and an upper column section length of 4 feet.

American Institute of Steel Construction (AISC)

While AISC Load & Resistance Factor Design (LRFD) does not specifically address the design of laterally loaded piles, Chapter H, "Members Under Combined Forces and Torsion," does address the design of columns subjected to combined axial and bending loads. The following is a summary of how the interaction diagrams were developed in accordance with AISC for Pile 5.

For $\frac{P_u}{\phi P_n} \geq 0.2$

$$\frac{P_u}{\phi P_n} + \frac{8}{9}\left[\frac{M_{ux}}{\phi_b M_{nx}} + \frac{M_{uy}}{\phi_b M_{ny}}\right] \leq 1.0 \qquad \text{(H1-1a)}$$

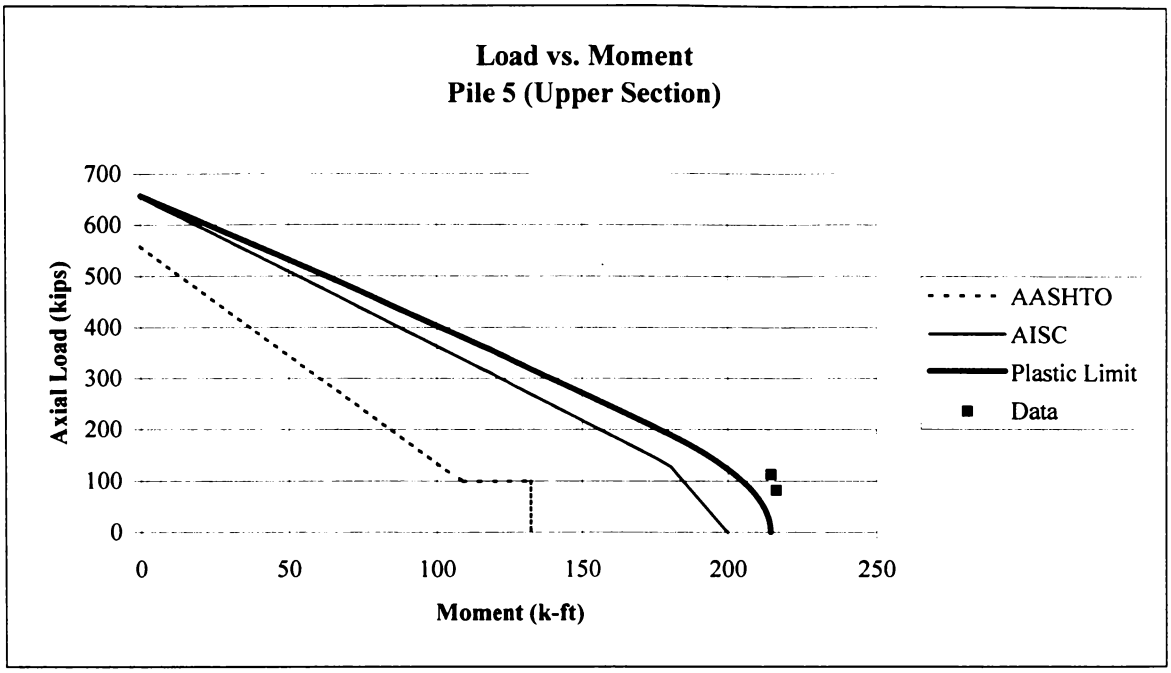


Figure 15: Pile 5 Upper Section Interaction Curves and Results

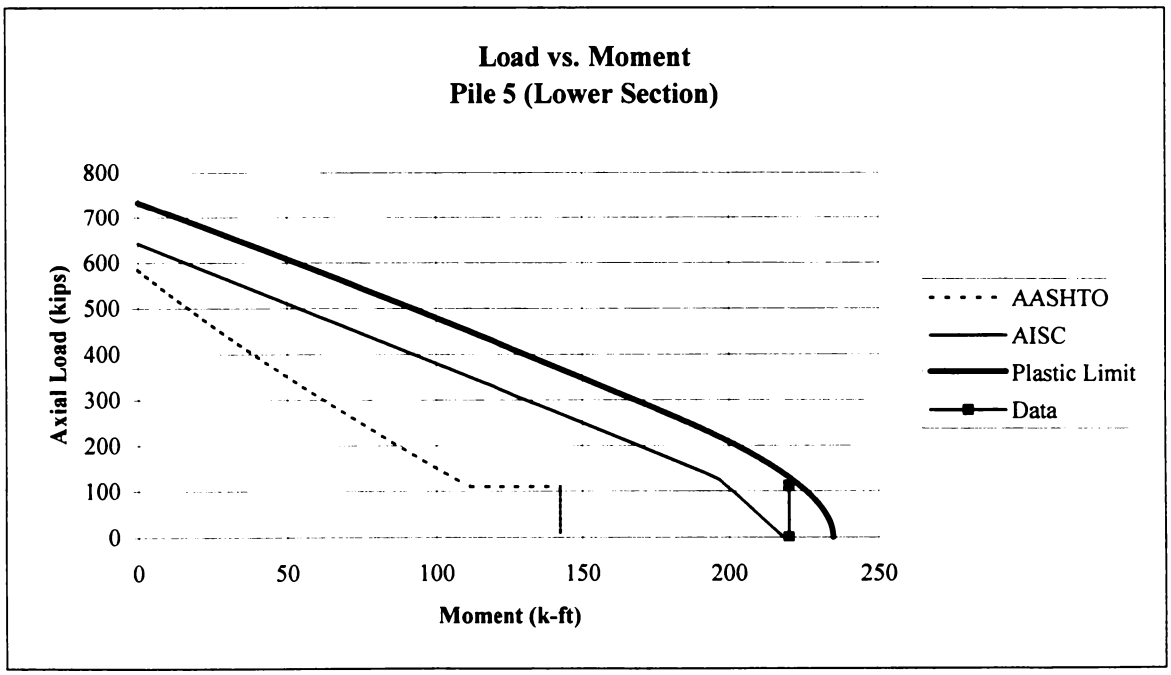


Figure 16: Pile 5 Lower Section Interaction Curves and Results

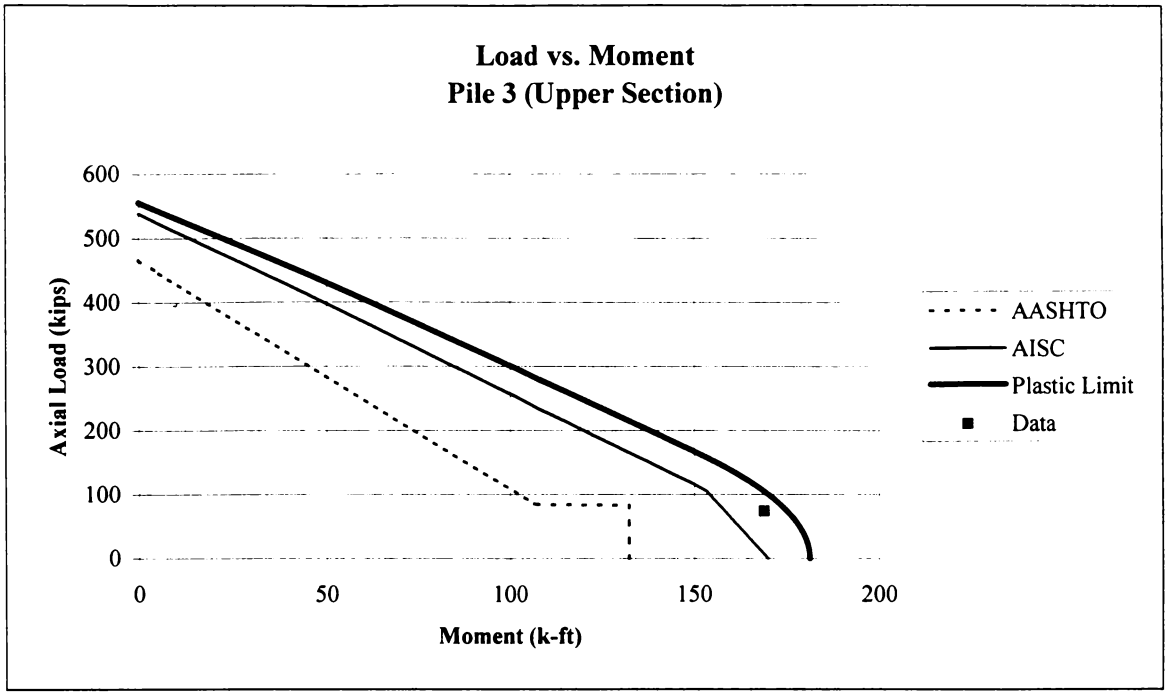


Figure 17: Pile 3 Upper Section Interaction Curves and Results

For $\frac{P_u}{\phi P_n} < 0.2$

$$\frac{P_u}{2\phi P_n} + \left[\frac{M_{ux}}{\phi_b M_{nx}} + \frac{M_{uy}}{\phi_b M_{ny}}\right] \leq 1.0 \qquad \text{(H1-1b)}$$

Since $M_{uy} = 0$, setting each of the two above equations equal to 1.0, and then solving for M_{ux}, provides a means of developing an interaction curve for a given pile.

$$M_{ux} = \frac{9\phi_b M_{nx}}{8}\left[1.0 - \frac{P_u}{\phi P_n}\right] \qquad \text{(D)}$$

$$M_{ux} = \phi_b M_{nx}\left[1.0 - \frac{P_u}{2\phi P_n}\right] \qquad \text{(E)}$$

P_n = nominal compressive strength determined in accordance with Section F1

M_n = nominal flexural strength determined in accordance with Section F1

$$P_n = A_g F_{cr} \tag{E2-1}$$

For $\lambda_c \leq 1.5$

$$F_{cr} = (0.658^{\lambda_c^2})F_y \tag{E2-2}$$

where

$$\lambda_c = \frac{KL}{r\pi}\sqrt{\frac{F_y}{E}}$$

AISC instructs that the effective length factor K shall be equal to 1.0 for a column with lateral support. The top of the pile is restrained against rotation by the abutment; therefore, an effective length factor of 2.0 is used when analyzing the upper portion of the pile. The section of pile between the two inflection points is considered pinned at each end, yielding an effective length factor of 1.0. Since buckling is being considered about the strong axis, r_x is deemed the appropriate value of radius of gyration to be used in all calculations. The nominal compressive strength determined from Section E2 is 654.7 kips and 641.7 kips for the upper and lower sections of Pile 5, respectively.

The limit states of yielding, lateral-torsional buckling, flange local buckling, and web local buckling must be investigated when determining the nominal flexural strength of the pile. In the case of the HP10x42, flange local buckling is the controlling limit state.

Yielding

$$M_n = M_p = F_y Z_x \leq 1.5 M_y \qquad \text{(F1-1)}$$

Lateral-Torsional Buckling

$L_b = 0$, due to continuous lateral support provided by surrounding soil.

$$M_n = M_p \qquad \text{(A-F1-1)}$$

Flange Local Buckling

The HP10x42 fails to satisfy the flange local buckling criteria. The slenderness parameter (λ) for the flange necessitates a reduction in the nominal moment capacity in accordance with Equation (A-F1-3).

$$M_n = M_p - (M_p - M_r)\left(\frac{\lambda - \lambda_p}{\lambda_r - \lambda_p}\right) \qquad \text{(A-F1-3)}$$

$$M_r = F_L S_x$$

$F_L = F_y - 10$ ksi, for rolled shapes

Web Local Buckling

$$M_n = M_p \qquad \text{(A-F1-1)}$$

The nominal flexural strengths determined from Section F1 are 199.9 k-ft and 218.2 k-ft for the upper and lower sections of Pile 5, respectively. The interaction diagrams for each of the two sections of pile can now be developed. When the axial

compressive force is greater than $0.2P_n$, the allowable moment is calculated using Equation (D); otherwise, the allowable moment is calculated using Equations (E). In an effort to use the AISC equations to predict the actual behavior of the pile, the reduction factors for both flexural and compressive strength were removed from equations (D) and (E).

The interaction diagrams resulting from the appropriate application of the AISC equations are plotted in Figures 15 and 16. The AISC interaction diagram for the upper section of Pile 3 is presented in Figure 17. Pile 3 had a yield stress of 45 ksi and an upper column section length of 4 feet.

The design equations presented by AISC predict the ultimate capacity of the member. For safety purposes, the ultimate capacity is then multiplied by a reduction factor to account for inherent uncertainties in material and section properties. Thus, the AISC equations, without the reduction factors, predict the ultimate capacity of a member. Since the goal of this chapter is to compare predicted ultimate capacity to experimental field test data, no reduction factors were applied to the AISC equations. In the AASHTO equations, the maximum bending strength (M_u) is calculated with the appropriate reduction for a noncompact section inextricably incorporated into the calculation. Therefore, the AASHTO equations cannot be used to predict ultimate capacity without the reduction factor applied. Consequently, the AASHTO interaction diagrams are plotted as "design" values, while the AISC diagrams are plotted as theoretical ultimate capacity values.

Plastic Limit

If length effects of a structural steel member are ignored, the ultimate capacity of a cross-section can be defined as any load combination that generates a stress condition where the entire cross-section is stressed to the yield strength of the material. The plastic moment ($M_p=F_yZ$) is the ultimate capacity in pure bending, while the yield axial load ($P_y=F_yA$) is the ultimate axial capacity. A symmetric section loaded to its plastic moment experiences the yield stress uniformly distributed in tension over half of its area and in compression over the other half. Since the net difference between the tensile and compressive forces is zero, the section is not capable of supporting any axial load. When a section is loaded to the plastic axial load, the entire section experiences the yield stress uniformly distributed, in either tension or compression, over its entire area. Therefore, the centroid of the applied force coincides with the centroid of the section, creating a moment arm of zero length; thus, no moment is developed.

A theoretical ultimate capacity interaction curve, hereinafter referred to as the "plastic limit," was created for the HP10x42 used in the field tests. The plastic limit curve was calculated through the altering of the plastic moment stress condition by moving the neutral axis towards the tensile side of the section in small increments until, ultimately, the plastic axial compressive load condition was achieved. At each increment, the tensile force was subtracted from the compressive force to obtain the net axial load on the section. Moments were then summed about the centroid of the section to obtain the applied moment. The section was assumed to be uniformly subjected to the yield stress; strain hardening was not considered. The fillets at the web-flange

connection were idealized as triangular. Dimensions for the triangular fillets were derived such that all section properties calculated for the section coincided with those listed by AISC for the HP10x42. Two separate plastic limit curves were generated, one for the typical HP10x42 pile and a second for the section containing the added strain gage protective shielding. These two curves are shown in Figures 15 and 16 for the upper and lower sections of Pile 5 (F_y = 53.2 ksi), and in Figure 17 for the upper section of Pile 3 (F_y = 45 ksi). The yield stress for each pile was determined from tensile testing of coupons taken from the flange of each pile prior to driving.

Comparison to Results Obtained From Field Tests

A detailed account of results obtained from the ultimate capacity hold-down tests was presented in Chapter 3. However, no reference was made to any figures illustrating the results due to the lack of development of any benchmarks by which to compare the results in Chapter 3. The upper section of Pile 5 experienced flange local buckling and, therefore, will be the main focus of capacity concerns. The load-moment results for the upper section of Pile 5 are plotted along with the AASHTO, AISC, and plastic limit interaction curves in Figure 15. The test data appear to exceed the plastic limit of the pile. This anomaly is at least partially explained by the fact that the plastic limit curve does not account for strain hardening. A stress increase of 3 ksi would justify the results. Due to the loss of the strain gages at the top of Pile 5, data regarding the ultimate strain developed in the pile were not obtained. However, based on material specimen tests, it is feasible that the magnitude of strain required to induce strain hardening of 3 ksi was

achieved during this test. Field test results for the lower section of Pile 5 and the upper section of Pile 3 are presented in Figures 16 and 17, respectively. Results for the lower section of Pile 3 were omitted due to relatively low moment induced in that area of the pile causing the results to lend minimal contribution to any drawn conclusions.

The Pile 3 abutment's inability to restrain pile rotation up to pile failure reduced the amount of moment present at the top of the pile. Also, the relatively low strength of the compacted fill in which Pile 3 was driven reduced the amount of moment induced in the lower section of the pile. Therefore, in terms of determining pile capacity, data obtained from Pile 3 are not nearly as useful as that obtained from Pile 5. However, the tests clearly demonstrated the inapplicability of the AASHTO and AISC column equations, and valuable information concerning the pile-abutment connection, which is beyond the scope of this paper, was deduced from that data.

Conclusion

The stated purpose of this chapter was to address the applicability of the AASHTO and AISC column design equations to the design of steel H-piles. These equations are applied to piles by taking the distance between calculated inflection points as the unsupported length. The applied axial load and moment were compared to the load-moment values obtained from the AASHTO and AISC equations and to those calculated at the plastic limit.

The combinations of axial load and bending moment in the steel H-piles for all three tests described herein were clearly beyond the capacity limits calculated using the

AASHTO and AISC equations for column design. Instead, the load combinations, for all practical purposes, were of the magnitudes that coincided with the plastic limits for the pile cross-section.

The test results clearly demonstrate the inappropriateness of applying the AASHTO and AISC column design equations, which consider length effects, to steel H-piles embedded in soil. Combinations of axial load and moment corresponding to the plastic limit capacity of a pile cross-section can more reasonably be used to evaluate the capacity of a pile. As noted earlier, however, the question of soil stiffness requirements to produce the support necessary to assure the development of the plastic limit capacity remains unanswered. This question is addressed in Chapters 7 and 8.

CHAPTER 6

MODEL VERIFICATION

Introduction

The validity of conclusions drawn from finite element model results is dependent on the accuracy of the model. Therefore, verification of model performance is necessary prior to analysis. This chapter addresses the verification of accurate model performance. The objectives include justification of element choice, verification of accurate section property representation, affirmation of the capability to accurately predict error, and confirmation of accurate performance when subjected to combined axial and bending stresses beyond yield.

Element Choice

Modeling a beam-column to a state of failure requires a plastic beam element with both axial and bending capabilities. Ansys 5.6 provides such an element in "Beam23 - 2D Plastic Beam." Beam23 is a uniaxial element with three degrees of freedom at each node (translation in x and y, and rotation in z) and plastic capabilities. A line of five integration points through the thickness of the element exists at three locations along the length of the element, one at each end and one at the mid-span. The five integration points through the thickness are located relative to the mid-thickness at ±50%(h), ±30%(h), and 0%(h). A diagram of the element with node locations, integration point locations, and degrees of freedom is presented in Figure 18. A beam cross-section is

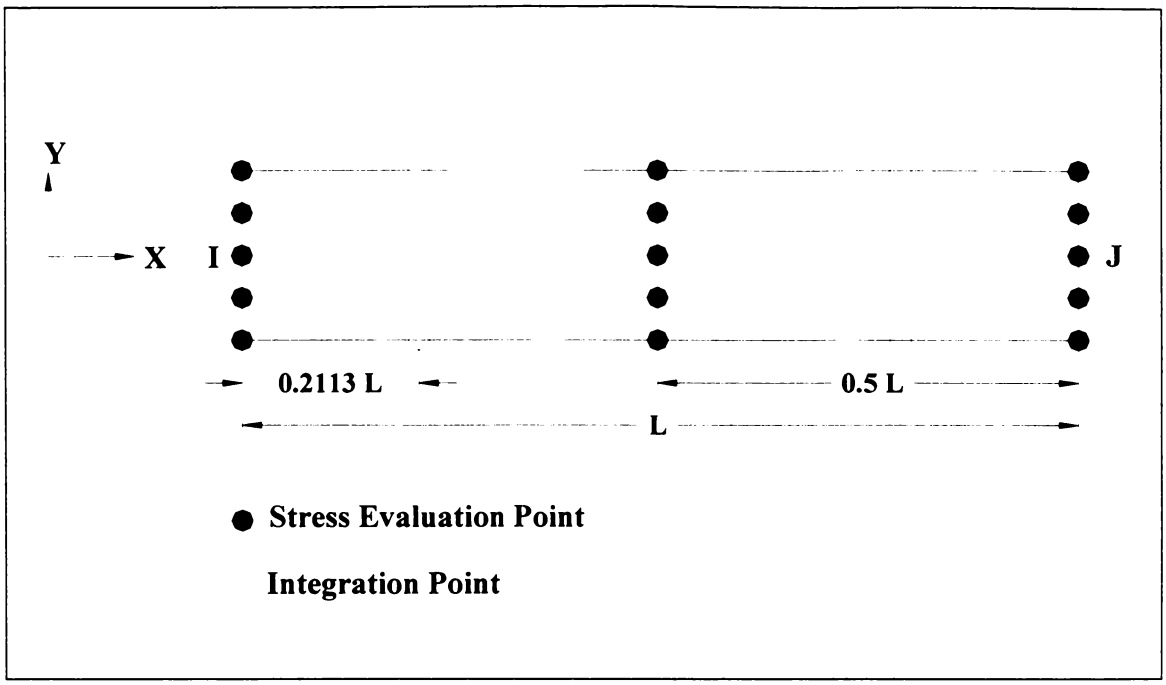


Figure 18: Ansys Beam23 Element

defined by inputting a section height and a five-location area distribution. The input areas are weighted distributions at the ±50%, ±30%, and 0% integration points. The height is defined as the distance between the ±50% integration points, and is not necessarily the actual height of the member. For a symmetric cross-section, area A(50)=A(-50) and area A(30)=A(-30).

Values of weighted distributions of area are chosen to accurately represent cross-sectional area, moment of inertia, fourth moment, and plastic section modulus. These properties are related to the integration points through the following equations.

$$A = \sum_{i=1}^{5} H(i)L(i)h$$

$$I_2 = \sum_{i=1}^{5} H(i)L(i)h(hP(i))^2$$

$$I_4 = \sum_{i=1}^{5} H(i)L(i)h(hP(i))^4$$

$$Z = \sum_{i=1}^{5} H(i)L(i)h|hP(i)|$$

where: H(i) = weighting factor at point i

H(±50) = 0.0625

H(±30) = 0.28935185

H(0) = 0.29629630

L(i) = effective width at point i, L(i) = A(i)/h

h = distance between +50% and –50% integration points (ie. height of section)

P(i) = integration point location in y direction (±0.5, ±0.3, 0)

A numerical relationship between the section properties and the input areas may be obtained by recognizing that L(i)h = A(i), and rewriting the above equations as follows.

A = 0.0625 (A(-50)+A(50)) + 0.28935185 (A(-30)+A(30)) + 0.29629630 (A(0))

I_2 = [0.015625 (A(-50)+A(50)) + 0.0260417 (A(-30)+A(30))] h^2

I_4 = [0.0039063 (A(-50)+A(50)) + 0.00234375 (A(-30)+A(30))] h^4

Z = [0.03125 (A(-50)+A(50)) + 0.08680554 (A(-30)+A(30))] h

In order for the elastic section modulus (S) to be accurately represented, the height (h) must be defined as the actual height of the cross-section. Subsequently, for a symmetric cross-section, the number of unknowns in the above equations is reduced to three; A(50),

A(30), and A(0). An initial estimate of values for the weighted distributions of area is obtained by solving the equations for A, I_2, and Z. The obtained values are then verified by accurate performance of a model whose behavior can be predicted through conventional analysis. A summary of the weighted area at each integration point for the standard HP10x42 and the modified HP10x42 is presented in Table 3.

Verification of Section Properties

Two basic models were used to verify section properties. The first model consisted of a simply supported beam deflected vertically at the one-third points beyond the deflection required to produce the plastic moment in the center region of the beam. A bilinear kinematic hardening material table containing a modulus of elasticity and a yield stress was used to define the material behavior. This beam model was used to verify accurate representation of the moment of inertia, elastic section modulus, and plastic section modulus. The load versus deflection curve obtained from the model was compared to deflection values obtained from statics in the elastic range to confirm that the moment of inertia of the element was correct. Accurate representation of the moment

Table 3: Weighted Areas at Integration Points

	HP10x42	Modified HP10x42
H	9.7	9.7
A(50)	58.8069	61.95358
A(30)	7.510754	8.977448
A(0)	2.371396	2.904254

of inertia of the standard HP10x42 and the modified HP10x42 is confirmed in Figures 19 and 20. The plastic section modulus was verified by dividing the maximum moment obtained from the model by the yield stress. Figures 21 and 22 show that the finite element models accurately predict the plastic moment capacity of the standard and modified HP10x42, thereby indicating an accurate representation of the plastic section modulus. Finally, plotting the change in moment divided by the change in deflection versus the moment divided by yield stress identified the point at which increased deflection no longer caused a constant increase in moment. This phenomenon occurs at the point of first yield, and the corresponding value of M/F_y is the elastic section modulus (S) of the element.

Figures 23 and 24 present the $\Delta M/\Delta\delta$ vs. M/F_y curve for the standard HP10x42 and the modified HP10x42, respectively. Also plotted on each of these two graphs is a vertical line representing the theoretical elastic section modulus for the respective cross section. It is apparent from these two plots that both models began to behave non-linearly when M/F_y was equal to the theoretical section modulus, thereby indicating that the model section modulus accurately represented the actual elastic section modulus for each of the two cross sections. The reason for the "stair stepping" shape of the results in the nonlinear portion of the curve is addressed in the following section.

One weakness of the 2D plastic beam element does become apparent when studying the curves presented in Figures 19 and 20. Since all of the element's area is lumped at the five integration points through its thickness, the element cannot yield through its thickness in a gradual manner when subjected to a uniform moment along the

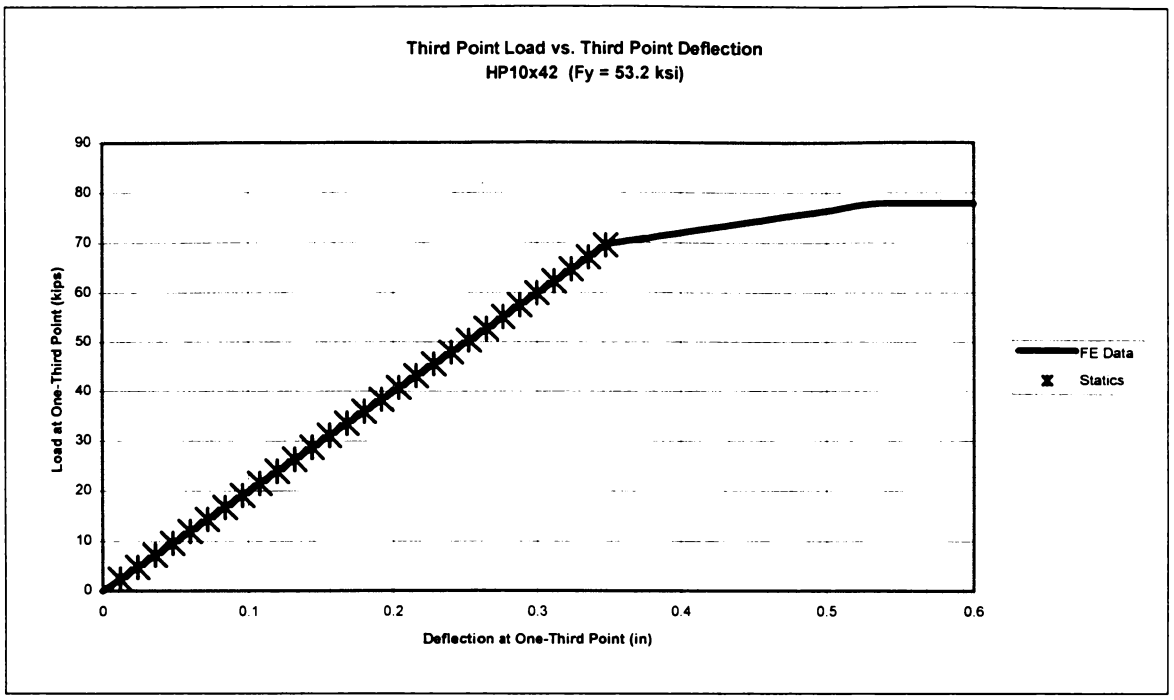


Figure 19: Load vs. Deflection (HP10x42): simply supported beam L = 100 in.

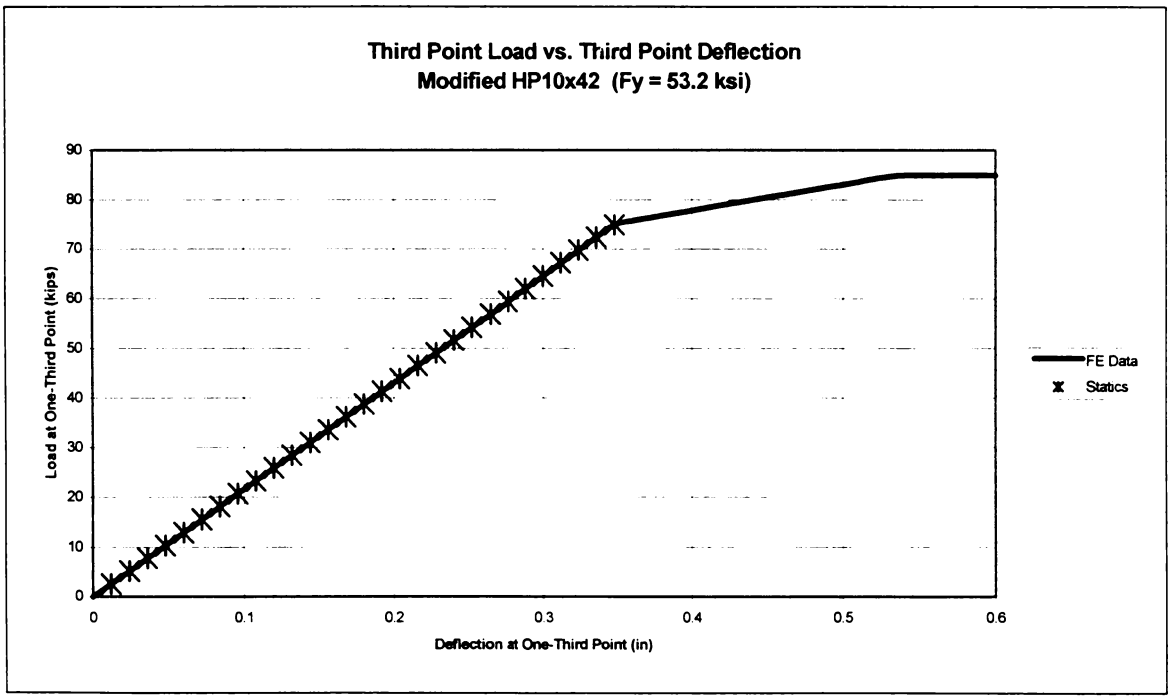


Figure 20: Load vs. Deflection (Modified HP10x42): L = 100 in.

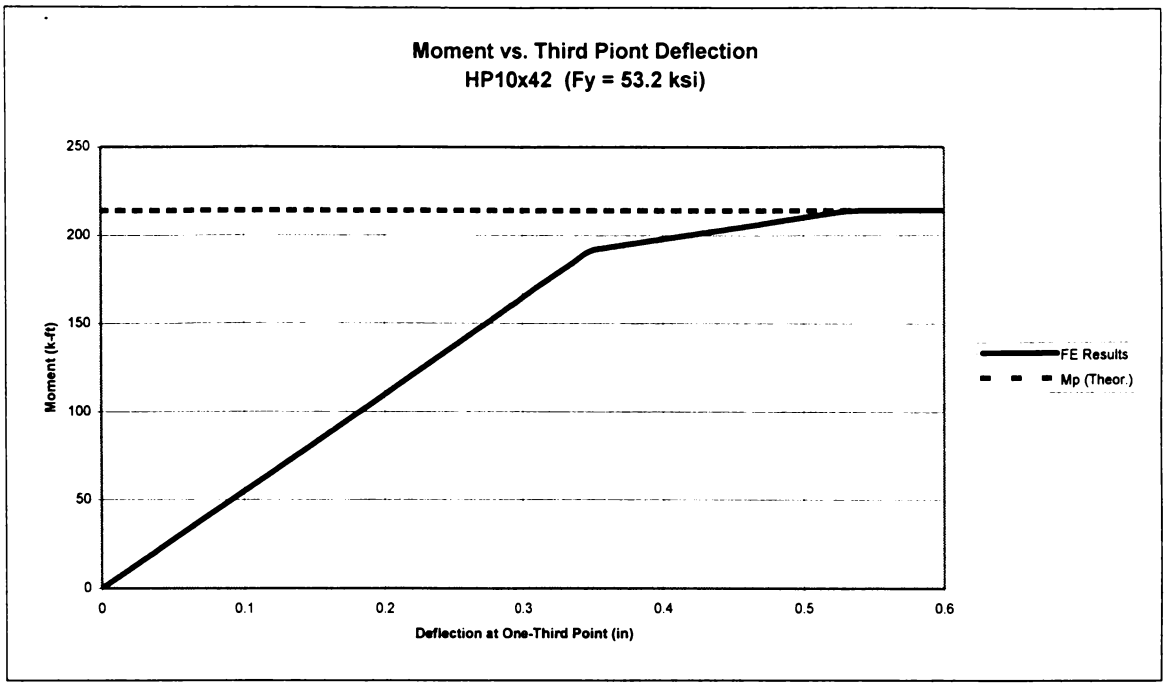


Figure 21: Moment vs. Deflection (HP10x42): simply supported beam L = 100 in.

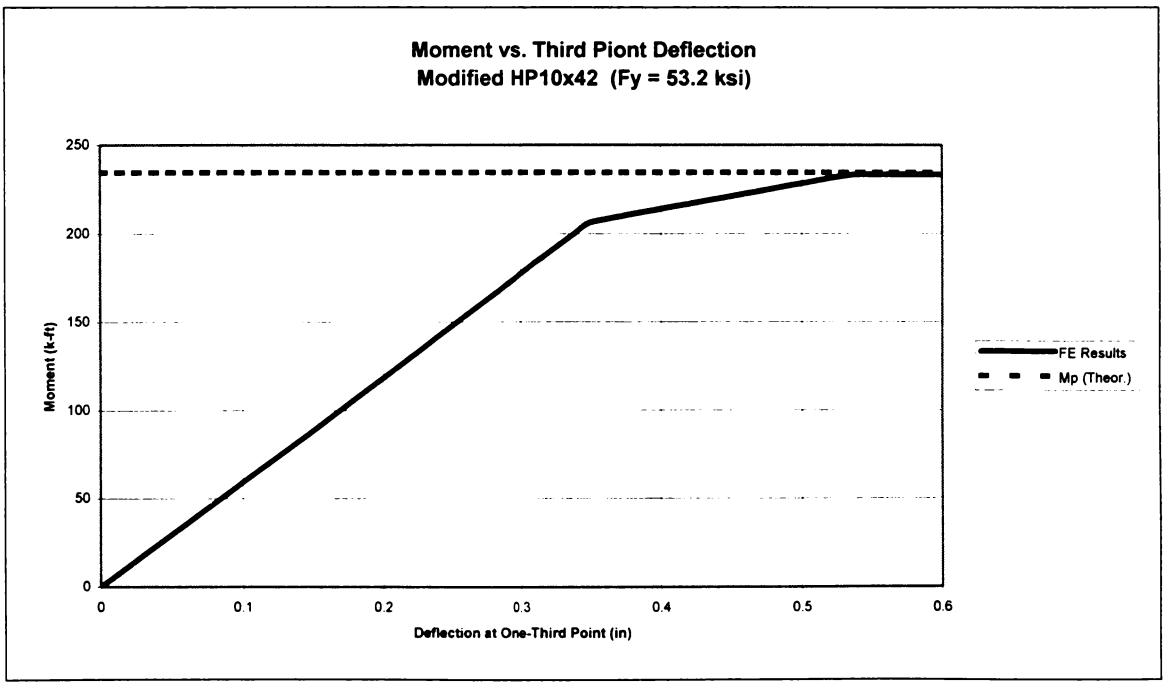


Figure 22: Moment vs. Deflection (Modified HP10x42): L = 100 in.

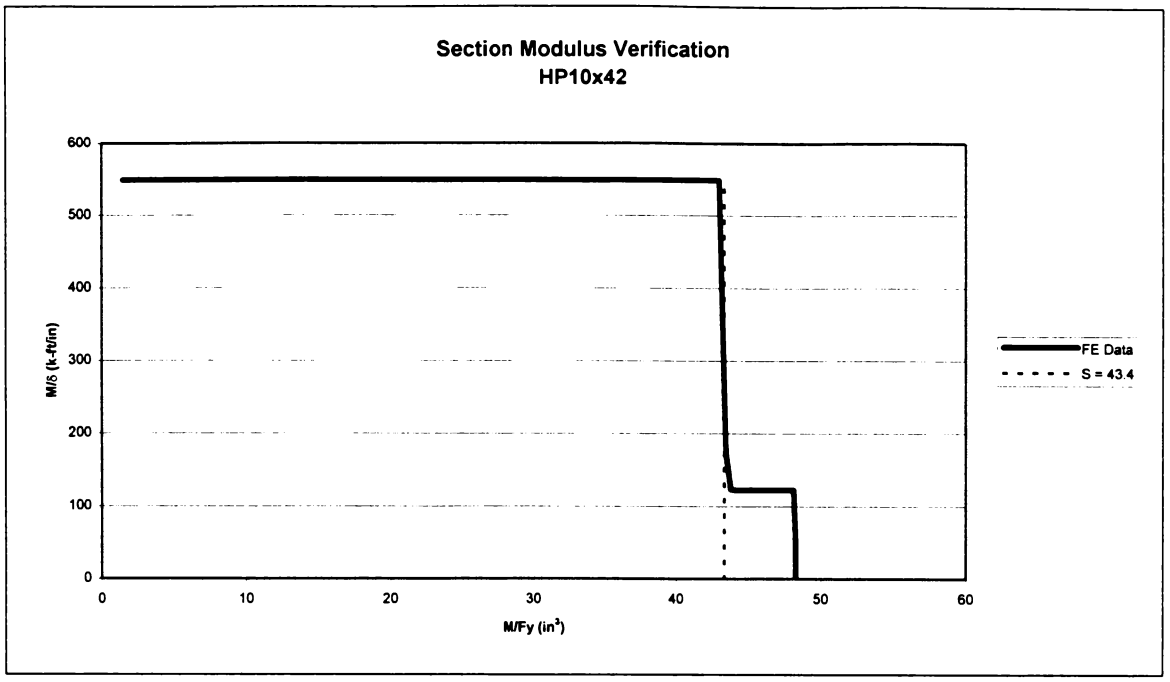


Figure 23: First Yield Location (HP10x42)

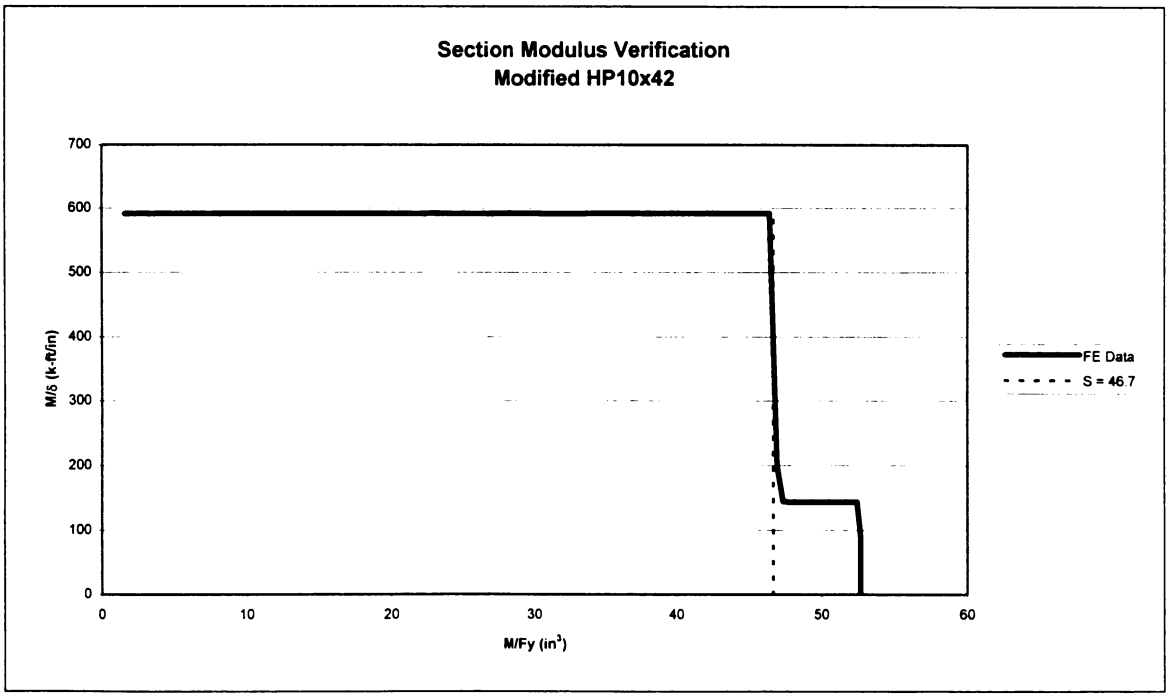


Figure 24: First Yield Location (Modified HP10x42)

length of the element. All of the E_t evaluation points along the length of the element (at a given elevation through its thickness) in the constant moment region of the beam experience yielding simultaneously and E_t at the integration points instantly changes from $E_{elastic}$ to zero. When the beam is subjected to a large moment gradient, the E_t evaluation points along the length of the element yield in a sequential manner and E_t at the integration points gradually transitions from $E_{elastic}$ to zero.

The second verification model consisted of a short column. Axially deflecting one end of the column until the compressive strain was greater than the yield strain of the material resulted in the yield axial force. Dividing the yield axial force obtained from the model by the yield stress, and then checking the resulting area against the area of the actual pile section, verified accurate representation of the cross-sectional area. Figures 25 and 26 illustrate the axial force versus axial strain results from the column verification models. A vertical line at the theoretical yield strain and a horizontal line at the theoretical yield load are also plotted for comparison to the finite element results. A summary of all results obtained from the section verification models is presented in Table 4.

Error Prediction

The ability to accurately predict expected error is crucial to developing a valid finite element model. Areas of particular concern when modeling beam-columns to failure include plastic moment prediction, second-order deflections, and accurate combined stress representation in the inelastic range. Basic knowledge of the numerical

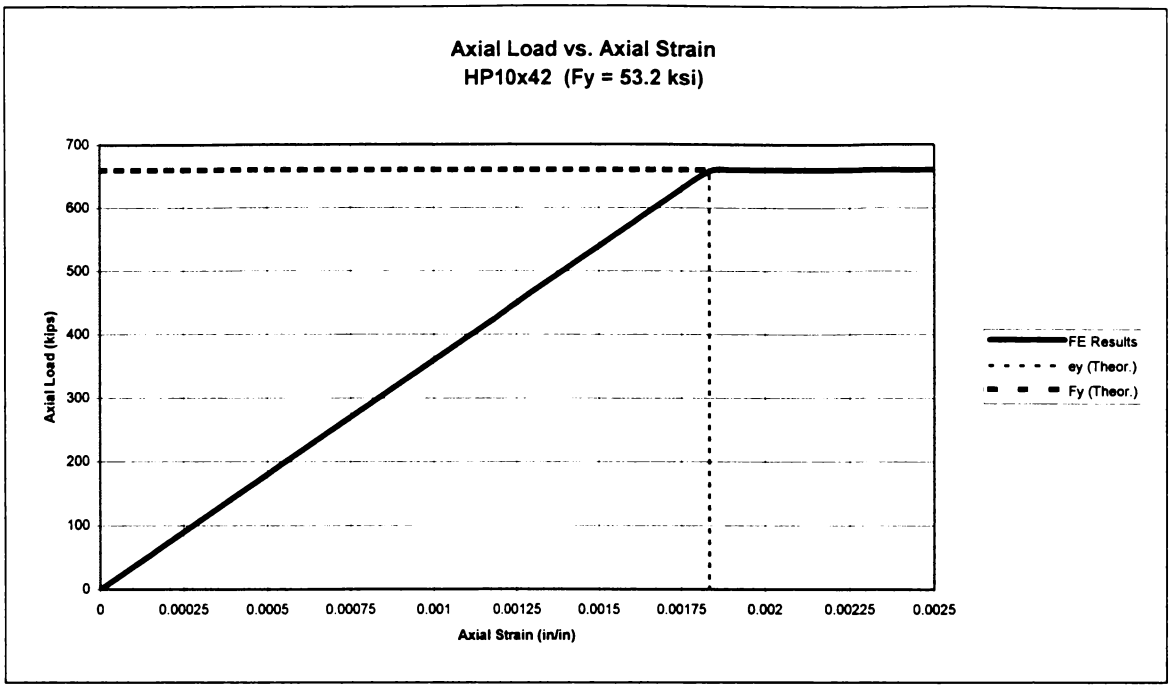


Figure 25: Load vs. Strain (HP10x42)

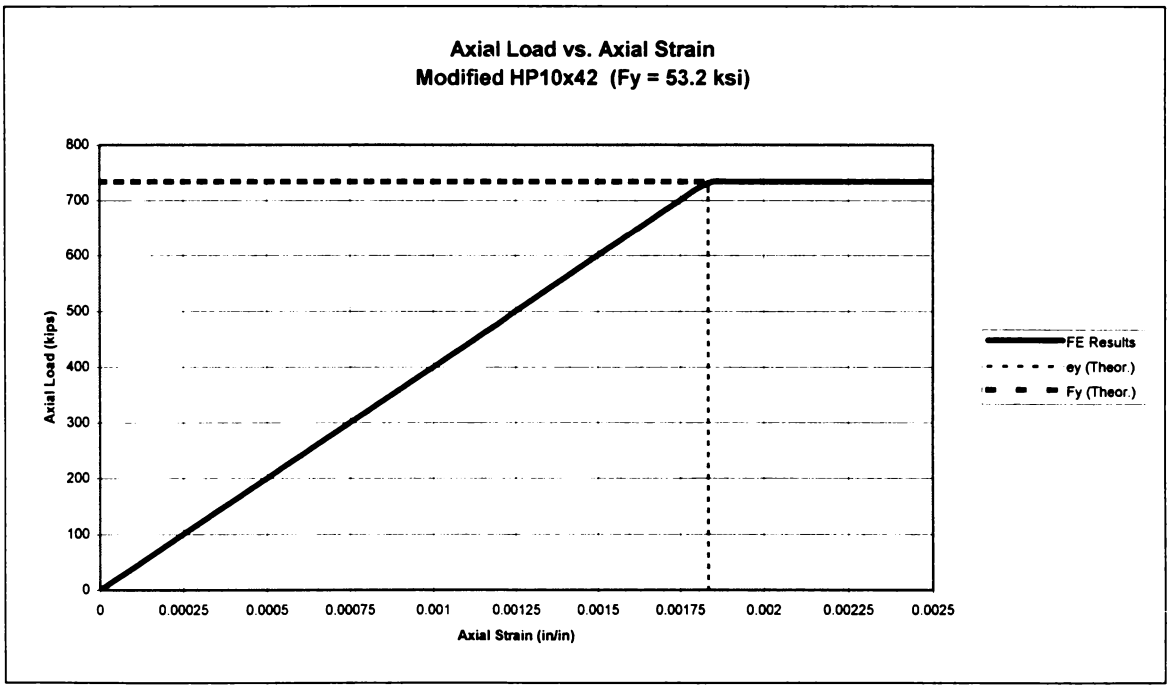


Figure 26: Load vs. Strain (Modified HP10x42)

Table 4: Section Verification Model Results Comparison (Third-Point Loading)

	HP10x42			Modified HP10x42		
	Actual	FE Result	% Diff.	Actual	FE Result	% Diff.
A (in^2)	12.4	12.4	0	13.8	13.8	0
I (in^4)	210	209.7	0.13	226.5	226.2	0.13
S (in^3)	43.4	43.24	0.36	46.7	46.43	0.58
Z (in^3)	48.3	48.30	0.01	52.9	52.68	0.42
M_p (k-ft)	214.13	214.15	0.01	234.52	233.55	0.42

integration procedure used to develop element results is necessary to predict and minimize calculation errors.

In the case of Beam23, the bending contribution to the stiffness matrix is defined as:

$$\left[K^B\right] = \int_L \left\{B_x^B\right\}\left(\int_{area} E_T y^2 d(area)\right)\left[B_x^B\right] dx \qquad \text{(Ansys 14.23-27)}$$

Two point Gauss rule is used to perform the integration along the length of the element, while integration through the thickness uses the 5-point rule. Stress evaluation is performed at the two ends and the mid-span of the element. Therefore, the tangent modulus evaluation is also performed at the two ends and the mid-span, and is assumed linearly distributed between evaluation points. The two Gaussian integration points are located a distance of 0.211325L (where L is the length of the element) inward from each end of the element. If the tangent modulus, E_T, is equal to the elastic modulus, the bending contribution of the stiffness matrix becomes the exact linear bending stiffness matrix. When the tangent modulus evaluation yields a reduced modulus at one end or the mid-span of the element, then E_T at the Gaussian integration points is assumed to be

linearly distributed between the adjacent E_T evaluation points. In a similar manner, nonlinear strains are linearly interpolated between evaluation points in order to calculate the bending restoring force at the integration points.

The resulting behavioral characteristics of the Beam23 element include accurate bending response in the elastic range, regardless of element length or moment gradient. However, once an inelastic condition is achieved, the accuracy of results is highly dependent on the combination of element length and moment gradient. Error approaches zero as either the element length or moment gradient approaches zero. Therefore, in order to achieve accurate results, the element length must remain relatively short in areas of inelastic bending with a large moment gradient. When the moment gradient is small, the element length can be increased to reduce computational time.

If an element is loaded such that the maximum moment occurs at one of the end nodes, then the magnitude of error in plastic moment prediction can be calculated as follows.

$$\%Error = \frac{0.211325L_e \frac{dM}{dx}}{M_p} x100\%$$

where: L_e = length of the element where yielding is occurring

$\frac{dM}{dx}$ = moment gradient across the element

In the case of a linear moment gradient, then

$$\frac{dM}{dx} = \frac{M_p}{L_0 - 0.211325L_e}$$

where, L_0 = distance from the maximum moment node to the point where M = 0.

A limited case study regarding maximum moment error prediction was performed using a 100 inch long simply supported beam loaded at the mid-span. To account for symmetry about the mid-span, only half of the beam was modeled. Error in the calculated maximum moment was predicted using the above equation and then compared to error calculated directly from the model results. The ability to accurately predict the magnitude of error in the maximum moment results can be seen in Table 5, which presents results when modeling the same beam with various values of L_e (the length of the element where yielding occurs). Also confirmed is the reality that the error is highly sensitive to the element length when the moment gradient is large. The third-point loaded model used for section property verification (shown in Table 4) confirmed that the error is negligible when the moment gradient is zero. Models Err_ver3 and Err_ver4 employed the same center element length, L_e, but Err_ver4 utilized much longer adjacent elements to help reduce computational time. These two models produced identical results, thereby indicating that plastic behavior of the model is not affected by the length of elements in the elastic areas of the model. Model Err_ver5 verified that the length of the yielding element could be reduced to a point where error is negligible, even in the presence of a large moment gradient.

Combined Stress Behavior

A beam element used to represent inelastic beam-column behavior must accurately respond to combined inelastic stresses. Accurate representation of the HP10x42 section properties A, I, and Z do not guarantee that the element will respond to

Table 5: Error Prediction Model Results (Mid-span Point Load)

Model Name	Total Number of Elements	L_e (in)	M_{max} (k-ft)	M_p (actual) (k-ft)	Error (%)	dM/dx (k-ft/in)	Predicted Error (%)
Err_ver1	1	50	271.78	214.13	26.92	5.43	26.79
Err_ver2	2	25	239.58	214.13	11.88	4.79	11.81
Err_ver3	4	12.5	226.14	214.13	5.61	4.52	5.58
Err_ver4	2	12.5	226.14	214.13	5.61	4.52	5.58
Err_ver5	3	1	215.05	214.13	0.43	4.30	0.42

combined stresses exactly as the actual pile does. Figure 27 presents results from a verification model consisting of a simply supported beam deflected vertically at its one-third points and then axially compressed while holding the vertical displacement constant. The initial load step determines the magnitude of moment present in the beam with no axial load. Then, as axial load is applied, the moment experienced by the beam remains relatively constant until first yielding occurs. When loaded beyond first yielding, the combined stresses in the beam converge to the plastic limit state. The model was run with various magnitudes of initial vertical deflection. As the axial load was increased, the solution began to converge to the plastic limit line.

The poor representation of the transition of yielding through the thickness of the 2D plastic beam element is again apparent in Figure 27. When the element is subjected to its inelastic bending capacity, the four integration points not located at the centroid of the member are experiencing inelastic strain. Therefore, the element's axial capacity under this strain condition is equal to the yield stress times the area located at the centroidal integration point, which is very small. As axial compression is increased, the

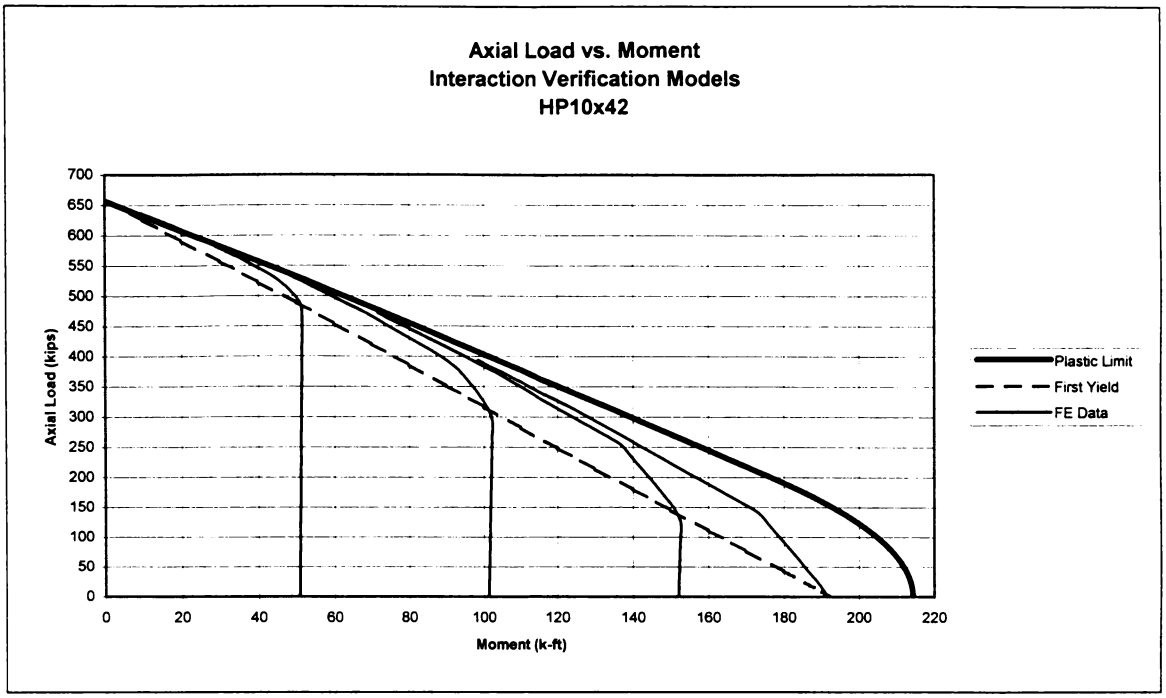


Figure 27: Axial Load vs. Moment for Interaction Verification Models

integration point that is experiencing tension during pure bending, and is adjacent to the centroidal integration point, must quickly achieve compressive strain to resist the applied axial force. The rapid change in direction of strain at this integration point causes a drastic reduction in the bending capacity. In the case of an actual steel member, the transition from tension to compression as axial load is applied in the presence of inelastic bending forces is much more gradual. The element's failure to accurately model the transition causes an underestimation of axial capacity in the presence of large bending forces. However, as the bending forces are reduced, the model's ability to represent interaction is enhanced, and it typically errs on the side of conservatism.

Second-Order Effects

A model's ability to accurately predict second-order effects can be demonstrated through the use of an elastic buckling model. Results from this model are then compared to P_{cr} calculated using Euler's elastic buckling equation. To illustrate the ability of Ansys 5.6 to predict second-order effects, a column with a fixed base and free head (flag pole column) was modeled using a purely elastic material. Three different lengths of the modified HP10x42 column were investigated, yielding KL/r values of 88.9, 97.8, and 106.7. A horizontal force of 0.1 kip was applied to the top of the column during the first load step, thereby generating an initial perturbation. The second load step involved axial displacement of the top node of the column. The axial displacement was increased in small increments until the column became unstable and buckling occurred. Figure 28 presents results from the finite element model along with a plot of the Euler buckling load for various values of KL/r. The results from the three different lengths of the column are tabulated along with the appropriate Euler solutions in Table 6. Finally, the case of KL/r = 106.7 was rerun with non-linear material properties included. Figure 29 illustrates that the effects of material non-linearity are only apparent in the post-buckling region of the load-deflection curve when buckling occurs due to elastic instability.

Soil Model Justification

Beam theory suggests that for a given moment diagram there exists a unique shear and load distribution along the length of the beam. The magnitude of the shear and

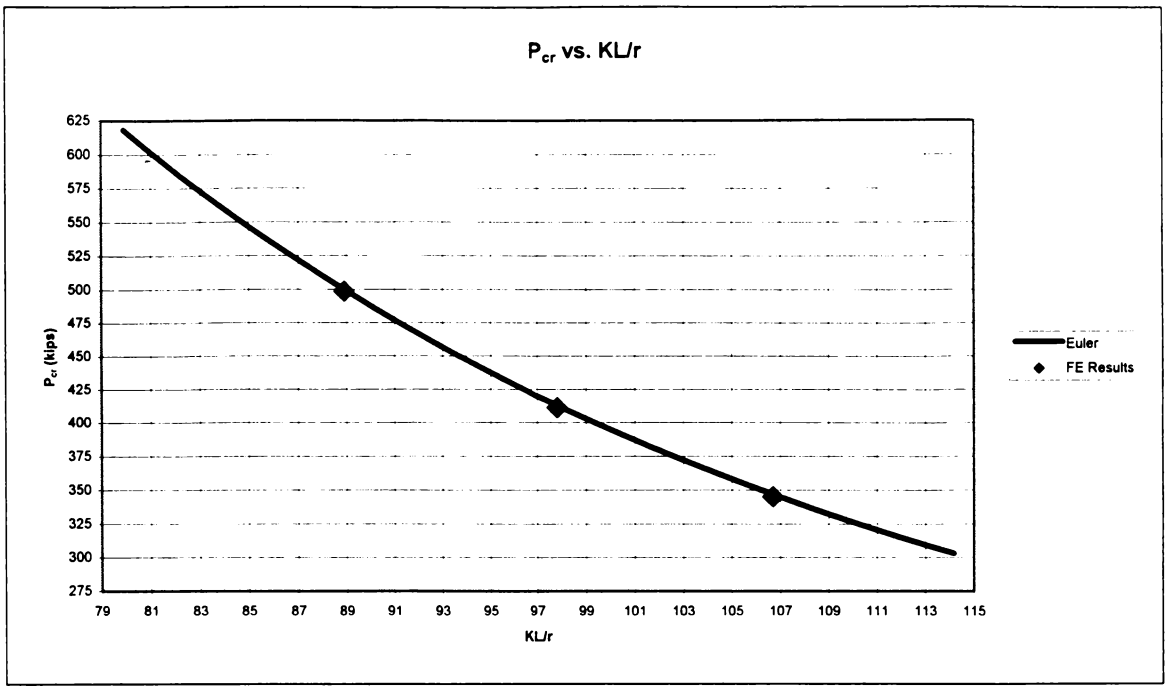


Figure 28: Comparison of Finite Element Buckling Capacity to Euler Solution

Table 6: Buckling Model Summary of Results

KL/r	Area (in^2)	FE P_{cr} (kips)	Euler P_{cr} (kips)	% Diff. (%)
88.9	13.8	498.5	499.8	0.25
97.8	13.8	411.4	413.0	0.38
106.7	13.8	345.1	346.9	0.53

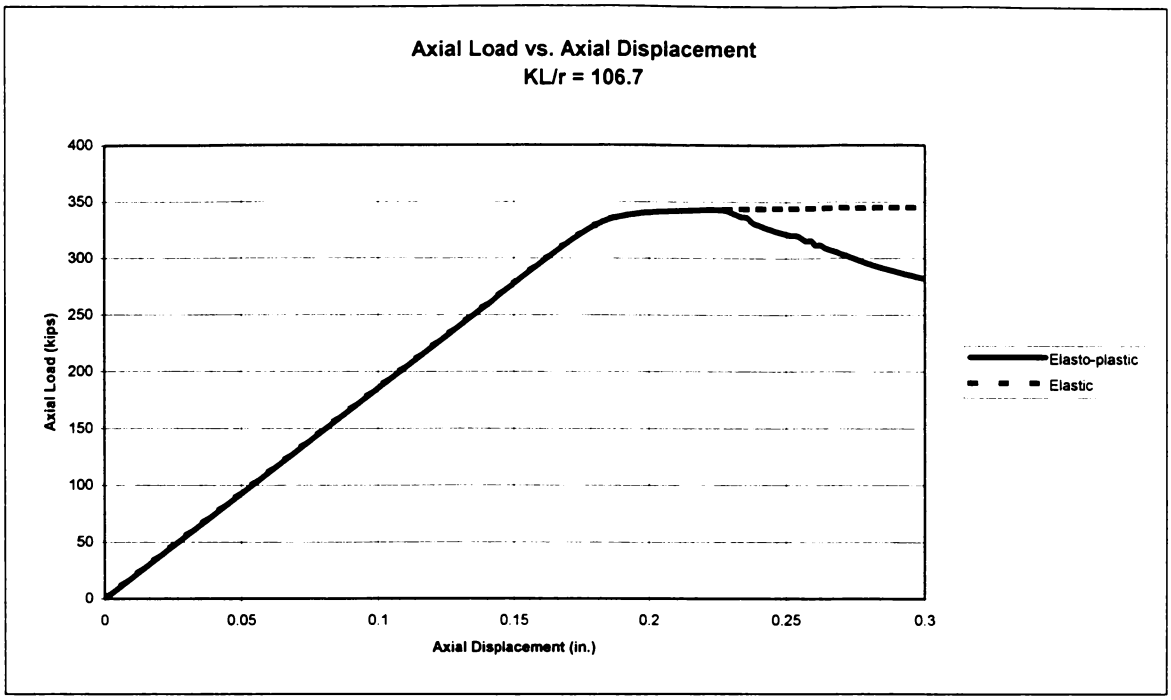


Figure 29: Comparison of Buckling with Elastic and Elasto-plastic Material

distributed load as a function of location along the beam are related to the moment distribution by the following equations.

$$V(x) = \frac{dM}{dx} \tag{6-1}$$

$$w(x) = \frac{dV}{dx} = \frac{d^2M}{dx^2} \tag{6-2}$$

When the distributed load is approximated through the use of point loads provided by discrete springs at each node, equation (6-2) is rewritten as follows.

$$w(x)dx = k_e\Delta = dV \tag{6-3}$$

where: dx = the distance between nodes

k_e = the effective spring constant for a given deflection

Δ = nodal deflection

Elastic theory also suggests that slope and deflection are functions of the distribution of moment along the length of the beam.

$$\theta(x) = \theta_0 + \int \frac{M}{EI} dx \tag{6-4}$$

$$\Delta(x) = \Delta_0 + \int \theta dx \tag{6-5}$$

Therefore, for a given moment diagram and boundary conditions for slope and deflection, there exists a unique slope diagram and deflected shape.

Elastic theory proves that shear distribution, and therefore change in shear (dV), is directly correlated to moment distribution. This theory also proves that beam deflection is directly correlated to moment distribution. Therefore, it is concluded that since Δ and dV are unique to each moment diagram, then, based upon $k_e\Delta = dV$, a unique k_e at each node exists. Hence, moment versus depth data along with shear and deflection data at the top of the pile obtained from field tests can be used to solve for the unique soil response, which is ultimately determined by the soil properties.

Soil Model

The soil is modeled using nonlinear discrete springs at each node. A force displacement curve for each spring is obtained by using a finite difference approach to solve the differential equation governing beam-column behavior. Moment versus depth along with shear and displacement data at the top of the pile were acquired from field tests and are used as the boundary conditions to solve for the deflection and soil reaction

per unit length of pile at each node. A slightly modified version of the differential equation for a beam-column on a continuous foundation as derived by Hetenyi (1946) is as follows.

$$E_p I_p \frac{d^4 y}{dx^4} + P_x \frac{d^2 y}{dx^2} - p = 0$$

where: E_p = modulus of elasticity of the pile material

I_p = moment of inertia of the pile in the direction of bending

P_x = axial load on the pile

p = soil reaction per unit length of pile

Based on Hetenyi's work, Reese (2001) presents a finite difference approach to solving the differential equation for a pile subdivided into increments of length *h* as follows.

$$y_{m-2}R_{m-1} + y_{m-1}(-2R_{m-1} - 2R_m + P_x h^2) + y_m(R_{m-1} + 4R_m + R_{m+1} - 2P_x h^2) + p_m h^4$$

$$+ y_{m+1}(-2R_m - 2R_{m+1} + P_x h^2) + y_{m+2}R_{m+1} = 0 \qquad (1)$$

where: y_m = deflection at node m

$R_m = E_p I_p$ at node m

P_x = axial load on the pile

h = distance between nodes

p_m = soil reaction per unit length of pile at node m

LPILE uses the above finite difference equation to solve for the response of a laterally loaded pile. In LPILE, the only unknowns in the above equation are the nodal deflections. Based on soil parameters input by the user, LPILE calculates an appropriate

value for p_m based on its generation of theoretical p-y curves. For the purpose of developing spring data, the above finite difference equation can be used in conjunction with moment versus depth data to solve for p_m as an unknown.

If the length of pile is divided into *n*-1 segments, thereby creating *n* nodes along the length of pile, then the finite difference approach yields *n* equations with *n+4* deflection unknowns and *n* number of p_m unknowns. Two of the four additional deflection unknowns are located at the two imaginary nodes above the top of the pile, and the remaining two correspond to the two imaginary nodes below the bottom of the pile. When equation (1) is written for each non-imaginary node, a total of *n* equations containing a total of *2n+4* unknowns are created. Additional n equations can be developed from the following finite difference equation for the moment at a node along with moment versus depth data obtained from field tests.

$$\frac{R_m}{h^2}(y_{m-1} - 2y_m + y_{m+1}) = M_m$$

The addition of the finite difference equation for the moment at each node increases the total number of equations to *2n*, thereby reducing the excess number of unknowns to four.

Four boundary conditions, two at the top of the pile and two at the bottom of the pile, are used to attain a solution. Horizontal shear and deflection data for the top of the pile were obtained from field tests and are used as boundary conditions at the pile head. At the tip of the pile, the horizontal shear and deflection are assumed to be zero and used as the remaining two boundary conditions. Shear is calculated in the finite difference form as follows.

$$\frac{R_m}{2h^3}(y_{m-2} - 2y_{m-1} + 2y_{m+1} + y_{m+2}) + \frac{P_x}{2h}(y_{m-1} - y_{m+1}) = V_m$$

A computer code written in Matlab was developed by the author to solve for the deflected shape and soil reaction for a laterally loaded pile where moment versus depth and horizontal shear and deflection boundary conditions are known. The code, presented in Appendix A, creates a coefficient matrix based on the finite difference equations and information regarding h and *n* input by the user. Moment versus depth and boundary condition data are then read into the program from a text file and a solution vector is calculated. The solution vector is then subdivided into two sub-vectors, one containing only the deflection data and the other containing only the soil reaction per unit length at each node. The soil reaction at each node can then be calculated by scalar multiplication of the soil reaction per unit length by the distance between nodes (with the exception of the top and bottom nodes which only have a tributary length of h/2). Nodal deflection and soil reaction (nodal force) data are then used to develop spring data for future use in the finite element models. A sample of p-y curves obtained from the previously mentioned Matlab program is presented in Figure 30.

In order to define the soil p-y curves, a non-zero nodal deflection at the elevation being investigated must occur. The experimental data did not produce significant pile displacement at elevations below approximately 6 feet beneath the ground surface. Therefore, an assumption was made that the p-y curve generated for a depth of 76.5 inches below the ground surface was applicable to all nodes below 76.5 inches. Figure

31 illustrates the relationship between the initial soil modulus (calculated from the p-y curves) and the depth of the soil for the upper 99 inches below the ground elevation.

These spring data are site, soil, and pile specific and only represent the behavior of the system used to collect the field data. However, these data can be used as a baseline from which to draw conclusions regarding the behavior of the system when soil stiffness is reduced to a small percentage of the baseline stiffness.

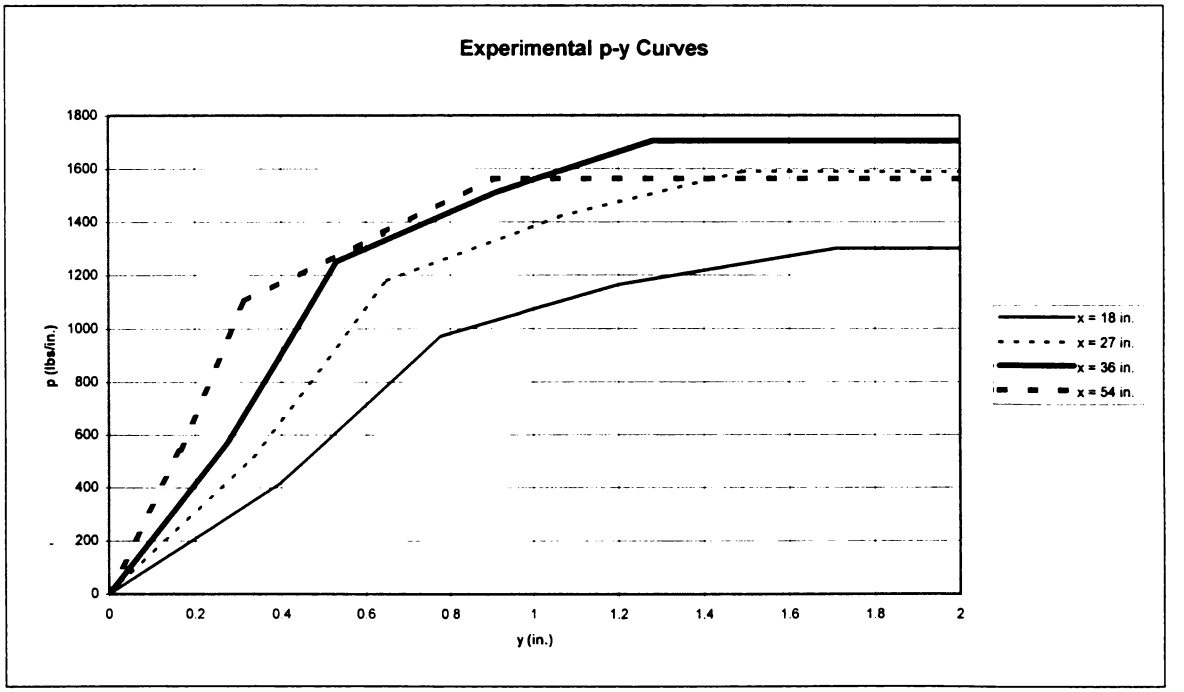


Figure 30: Pile 5 Sample p-y Curves Obtained From Experimental Data

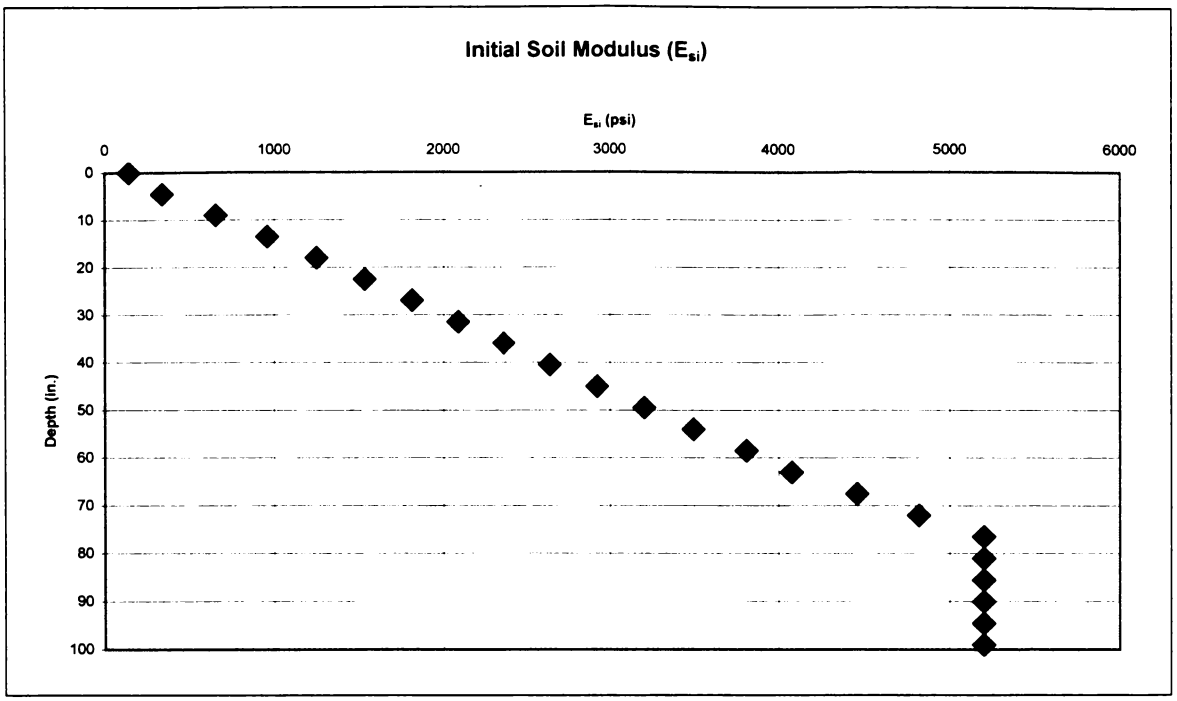


Figure 31: Pile 5 Initial Soil Modulus vs. Depth Obtained From Experimental Data

CHAPTER 7

MODELING OF PILE BEHAVIOR

Introduction

The objective of the finite element modeling described in this chapter is to determine the minimum amount of lateral support required from surrounding soil to prevent laterally loaded piles from experiencing inelastic beam-column buckling when subjected to axial load. Baseline soil properties were determined as described in Chapter 6 from a set of field test data collected in East Tennessee. All soil strength references in this chapter are in terms of percentage of the full strength value of the soil surrounding the tested pile.

Beam-column failure typically occurs due to a combination of instability and inelastic bending (Maleck, 2001). Euler buckling cannot predict this type of combined failure. The bifurcation point predicted by the classical Euler solution does not account for the fact that portions of the column become inelastic prior to buckling (Salmon and Johnson, 1990). Therefore, the Euler buckling solution is an upper boundary that is not achieved by typical length columns. Figure 28 presents the Euler buckling load of the modified HP10x42 as a function of KL/r, while Figure 32 illustrates the same information as a function of K, with L and r equal to values consistent with the tested pile.

In order to predict the true capacity of a beam-column, material non-linearity and stability issues must be accounted for. Nonlinear buckling analysis models were used to generate all results presented herein. These models account for both inelastic material

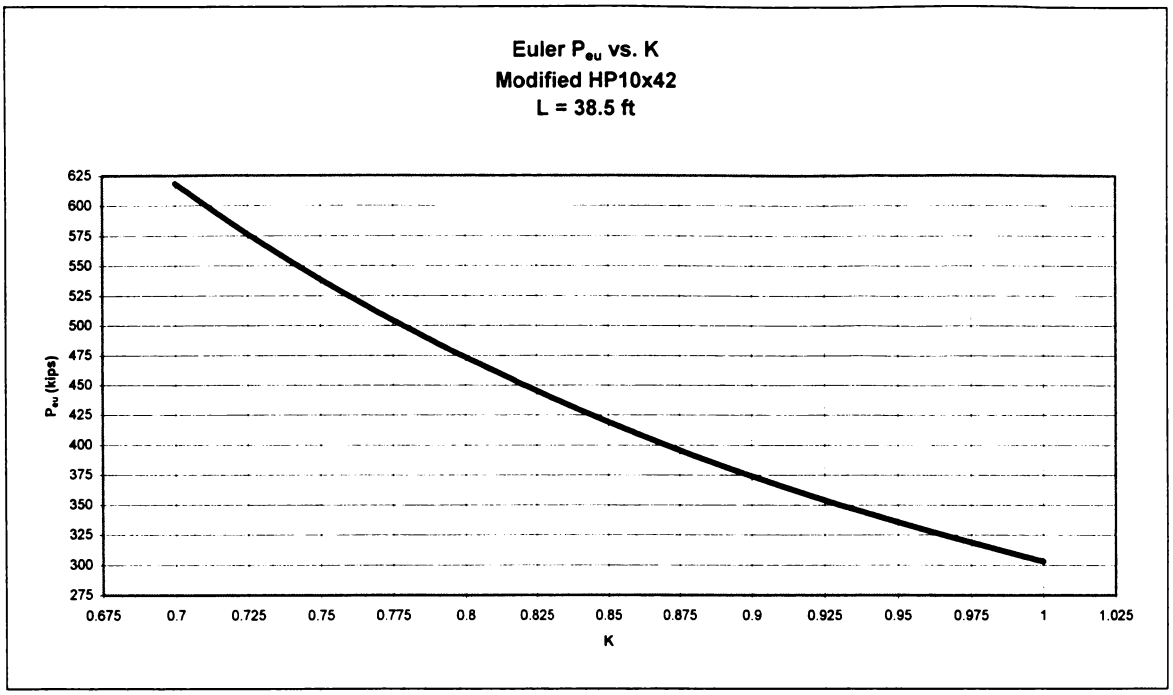


Figure 32: Euler buckling load vs. K for modified HP10x42 with L = 38.5 ft.

behavior and instability due to second order effects for a given initial perturbation. In the absence of sufficient lateral support to control second order deflections, the addition of axial load causes an increase in lateral deflection, which in turn causes increased moment due to additional eccentricity between the point of axial load application and the centroid of the member at its point of maximum deflection. This type of behavior continues until the lack of stability causes inelastic bending in the column.

The models predict failure due to instability, total yielding of the cross section, or a combination thereof. Failure possibilities not accounted for by the models include (1) reduced capacity due to residual stresses and (2) local buckling of elements of the cross section. Each pile was assumed continuously braced in the weak axis direction, as is

typical in the design of piles supporting integral abutments; therefore, lateral torsional buckling was not considered.

Model Specifics

All finite element modeling was performed using Ansys 5.6. The pile was modeled using 2-D plastic beam elements attached to non-linear springs at each node to represent the surrounding soil. Node spacing below the ground surface was 4.5 inches. Each of the 18 springs located in the upper 76.5 inches below the ground surface possessed its own force-deflection properties as determined by the methods described in Chapter 6. The spring defined at the 76.5 inch depth was used at all nodes below a depth of 76.5 inches. A diagram of the model is shown in Figure 33. The non-linear springs were defined up to a deflection that corresponded to field data collected for a lateral pile displacement at the ground elevation of 2.4 inches. The springs were conservatively assumed to be purely plastic for any deflection greater than that corresponding to the 2.4 inch field data. Each model included geometric non-linearity and material non-linearity (for both the pile and the soil). Model dimensions were representative of the dimensions of the test pile used to collect the field data. Load was applied at a distance of one foot above the ground surface, and the pile extended approximately 37.5 feet into the ground.

A pinned connection was used at the bottom tip of the pile to reduce computational time. The pinned connection was not believed to significantly affect results since the lateral deflection at an elevation of 37.5 feet below ground is near zero

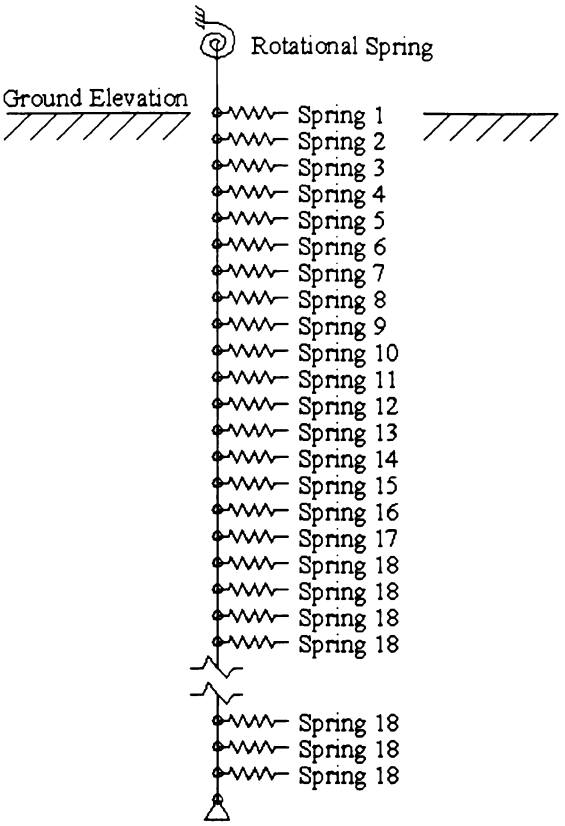


Figure 33: Finite Element Model Illustration

when surrounding soil is present. Also, the pinned connection provided the possibility to perform an analysis without surrounding soil.

A node spacing of 4.5 inches was used below the ground surface. Above the ground surface, node spacing decreased from 4 inches at ground elevation to 1 inch at the top of the pile. The node spacing at the top of the pile was reduced in an effort to minimize error when the top element experienced inelastic behavior in the presence of a large moment gradient. Node spacing did not require reduction in any areas below the ground surface because the moment gradient in the inelastic regions of the pile below ground is rather small.

Pile Loading

The top of the pile was deflected 1.145 inches, which corresponds to 1 inch of lateral displacement of the pile at the ground surface as determined from the field test data. A pile supporting an integral abutment is laterally supported at the abutment by the superstructure. Therefore, once the lateral displacement at the top of the pile is applied, the lateral displacement is held constant. After the application of the lateral load was complete, the top node was deflected downward until failure was achieved. The use of displacement to apply the axial load made it possible to obtain axial load versus axial deflection results in the non-linear range. Achieving results beyond the peak axial load would not have been possible if the axial load was applied as a force.

In order to study the effects of soil stiffness on the behavior of a pile, the soil stiffness was reduced to a percentage of the original value by altering the force data used to define the force-deflection curves for the soil, and the model run was reinitiated. Figure 34 shows an example soil spring force-deflection curve for the baseline soil and a second soil having a stiffness equal to 10% of the baseline soil stiffness. The reduced stiffness curve was obtained by multiplying each of the baseline soil force values by 0.10. Values of soil stiffness investigated included 100%, 10%, 1%, 0.1%, and 0% (no soil), all relative to the baseline soil stiffness obtained from the field data.

Three different rotational boundary conditions at the top of the pile were used during modeling. During the first set of tests, the moment at the pile-abutment connection obtained from the field data was applied to the top of the pile. The applied moment was held constant during the application of the axial deflection. However, the

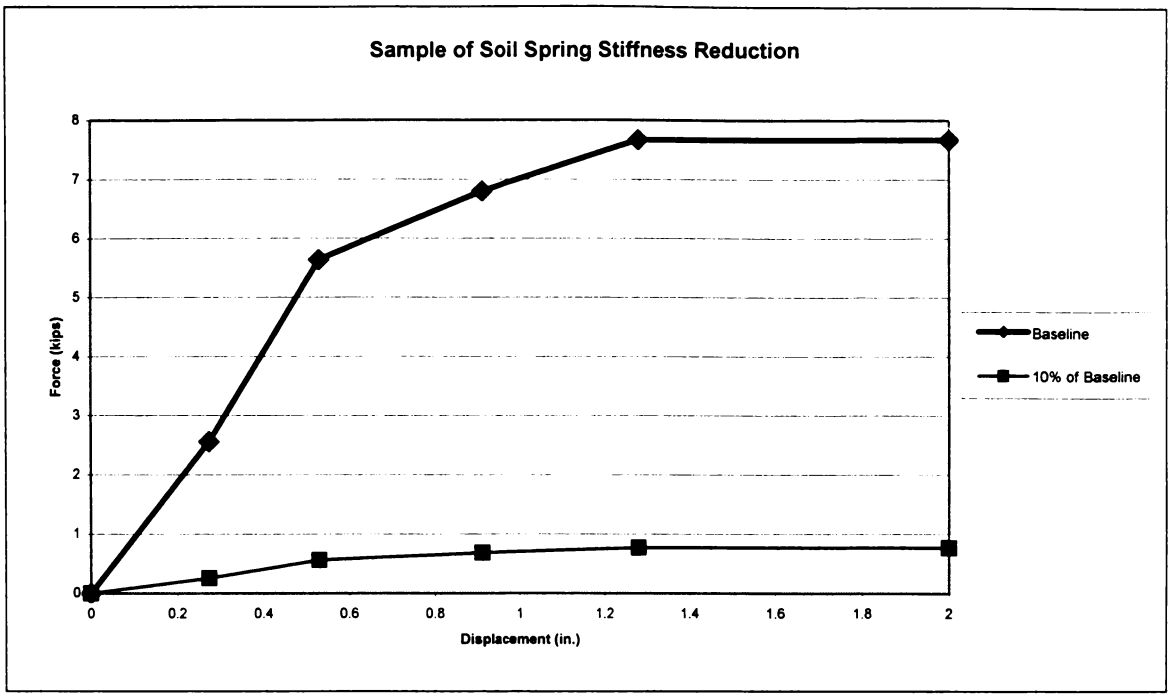


Figure 34: Sample of Soil Spring Stiffness Reduction

moment distribution, including the magnitude of the moment at the top of the pile, is a function of pile stiffness, soil stiffness, and the rotational stiffness of the pile-abutment connection. As the soil stiffness is reduced, while pile stiffness and rotational stiffness are held constant, the magnitude of the moment at the top of the pile is also reduced. Also, as axial load is applied to the pile, second order effects cause a slight change in the moment at the pile-abutment connection. Therefore, the application of a constant moment at the top of the pile for various values of soil stiffness is not the most appropriate method of modeling pile response.

The test pile used to collect field data incorporated an abutment with a rotational stiffness that was representative of a typical jointless bridge support. The rotational stiffness of an actual pile-abutment connection is a function of the moment of inertia of

the superstructure, length of spans, and number of spans. Therefore, rotational stiffness values are somewhat "bridge specific."

After the lateral displacement and moment were applied at the top of the pile to the first model, which represented the field test pile, data were obtained for the nodal rotation of the node at the top of the pile. From the rotation data and magnitude of moment applied to the pile, an estimate of the rotational stiffness at the top of the pile was obtained. The second set of models utilized a rotational spring at the top of the pile to represent the rotational stiffness of the pile-abutment connection. A rotational stiffness value of 18200 k-ft./rad was used for the rotational boundary condition at the top of the pile in the second set of models. When a rotational spring was used to control pile-head rotation, the magnitude of the moment at the top of the pile depended on the magnitude of the soil stiffness, and therefore was different for each set of soil springs investigated. As axial deflection was applied to the pile, the magnitude of moment at the top of the pile was able to change depending upon second order effects.

A third set of models was created with a fixed connection at the top of the pile. This set of models represents a "worst case" scenario for moment at the pile head. As with the second set of models, the moment at the top of the pile was dependent upon the soil stiffness. As the soil stiffness decreased, so did the magnitude of moment at the pile head.

In addition to the three sets of models mentioned above, a second set of rotational stiffness boundary condition models that incorporated a gap between the soil and the pile from the ground surface to a depth of six feet below ground were investigated. The gap

was assumed to be caused by only partial recovery of soil strain upon unloading. The assumed recovery percentage used for these models was 50%. Deflection results for the upper six feet of pile were obtained from the initial load step for the rotational stiffness models and then multiplied by 0.5. The force-displacement curve for each nonlinear spring located in the upper six feet was then offset such that the spring reaction force was zero until pile displacement reached a value equal to 50% of the maximum displacement experienced during the original load cycle. Lateral and axial load were then applied in the same manner as in the previously mentioned models.

For each model, data were obtained regarding initial and final moment distribution and deflected shape, as well as axial load versus axial deflection. In the cases where moment at the top of the pile was not held constant, moment reversal at the pile head can be seen as the pile becomes unstable. The deflected shape change illustrates the soil's ability to control later deflection below the ground elevation after the axial load is applied. Finally, axial load versus axial deflection data are used to determine when axial capacity is lost due to inadequate lateral support.

Constant Moment Model Results

The first set of models incorporated an applied moment at the pile head that remained constant throughout all load applications. The magnitude of the moment was equal to that obtained from field test data for a lateral pile deflection of 1 inch at the ground elevation. Figure 35 illustrates the relationship between axial load and axial deflection for various values of soil stiffness when the moment at the top of the pile is

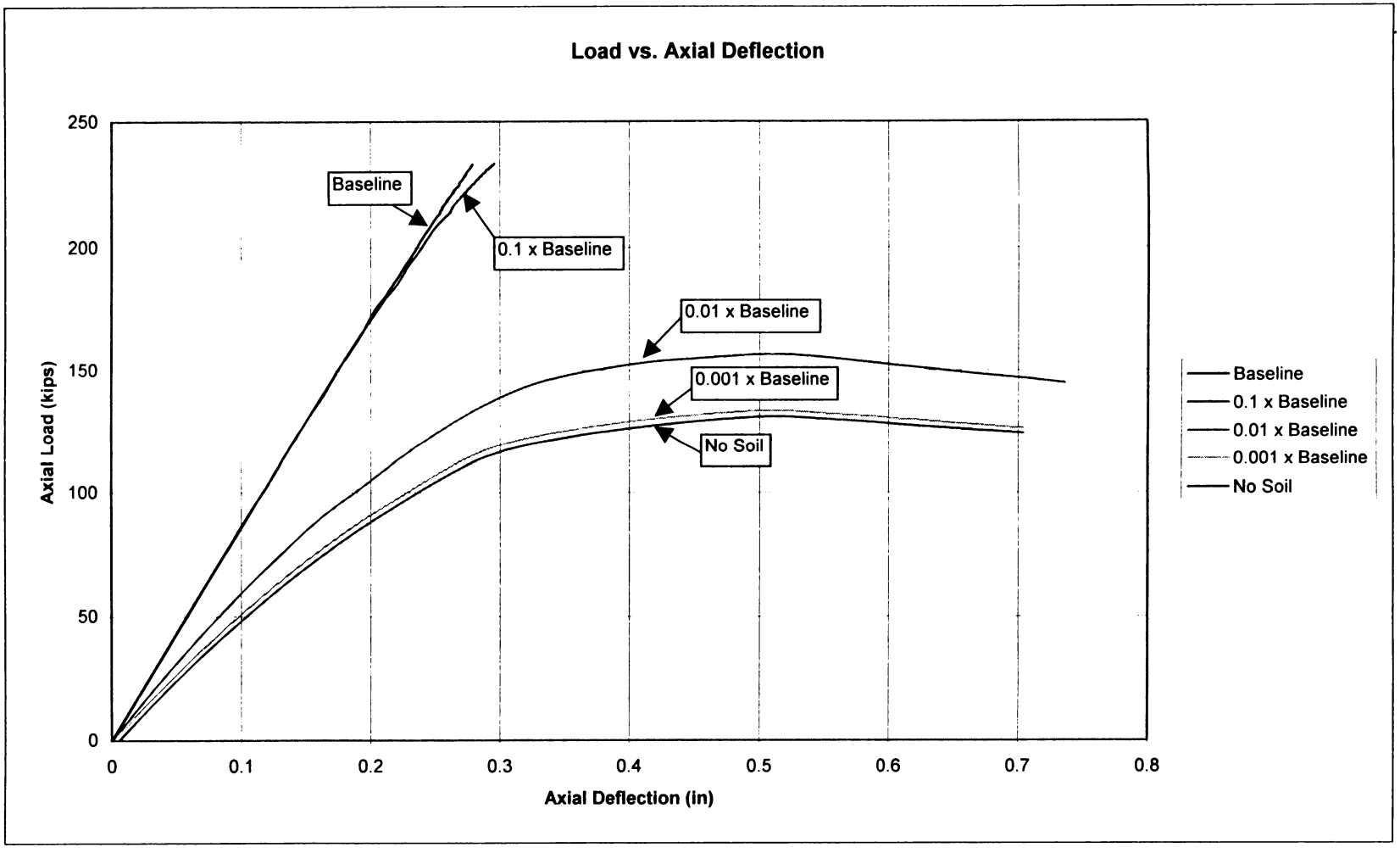


Figure 35: Load vs. Axial Deflection: Constant Moment Models

held constant. Table 7 provides a summary of the results obtained from each of the "constant moment" models. When the soil stiffness is reduced to 1% of the baseline, sufficient lateral support to control second order deflection in the lower portion of the pile no longer exists. The maximum moment in the lower portion of the pile is magnified from 158.5 k-ft to 205.3 k-ft after the application of the axial load. As the soil stiffness is reduced, the magnitude of moment magnification increases.

Figures 36 through 45 show the initial and final moment distribution and deflected shape for each of the constant moment models. The deflected shape plots for each of the models, other than the baseline model, show a slope at the top of the pile inconsistent with the actual response of a laterally loaded pile. This anomaly is due to an applied moment at the top of the pile that is greater than the natural moment generated from lateral deflection. Changing the boundary condition at the top of the pile to include a rotational spring to control pile head rotation to a value consistent with the rotational stiffness of a typical pile-abutment connection leads to a more accurate response.

Discussion of Constant Moment Model Results

Observing the change in deflected shape of each pile as axial load is applied and then studying the resulting change in moment distribution can help one to understand the behavior that leads to failure of the models. Exact results pertaining to moment magnification, predicted plastic limit axial capacity based on initial bending condition, and actual axial capacity predicted by the models is presented in Table 7. The pile is said to have a reduced axial capacity when the finite element model capacity is less than the

Table 7: Constant Moment Model Results

	Top of Pile				Lower Portion of Pile					
	Initial Load Step		Final Load Step		Initial Load Step		Final Load Step			
Soil Strength (% of Base)	Initial Moment (k-ft)	Plastic Limit Axial Load (kips)	Final Moment (k-ft)	Plastic Limit Axial Load (kips)	Initial Moment (k-ft)	Plastic Limit Axial Load (kips)	Final Moment (k-ft)	Plastic Limit Axial Load (kips)	FE Model Axial Load (kips)	Reduced Capacity?
100	-165.2	231.0	-164.5	232.9	98.6	483.6	100.3	479.2	232.9	No
10	-165.2	231.0	-164.6	232.6	28.8	661.8	31.5	655.0	233.3	No
1	-165.2	231.0	-165.2	231.0	-158.5	325.4	-205.3	190.3	144.8	Yes
0.1	-165.2	231.0	-165.2	231.0	-160.6	319.7	-210.3	171.8	126.3	Yes
0	-165.2	231.0	-165.2	231.0	-160.9	318.9	-210.8	169.9	124.3	Yes

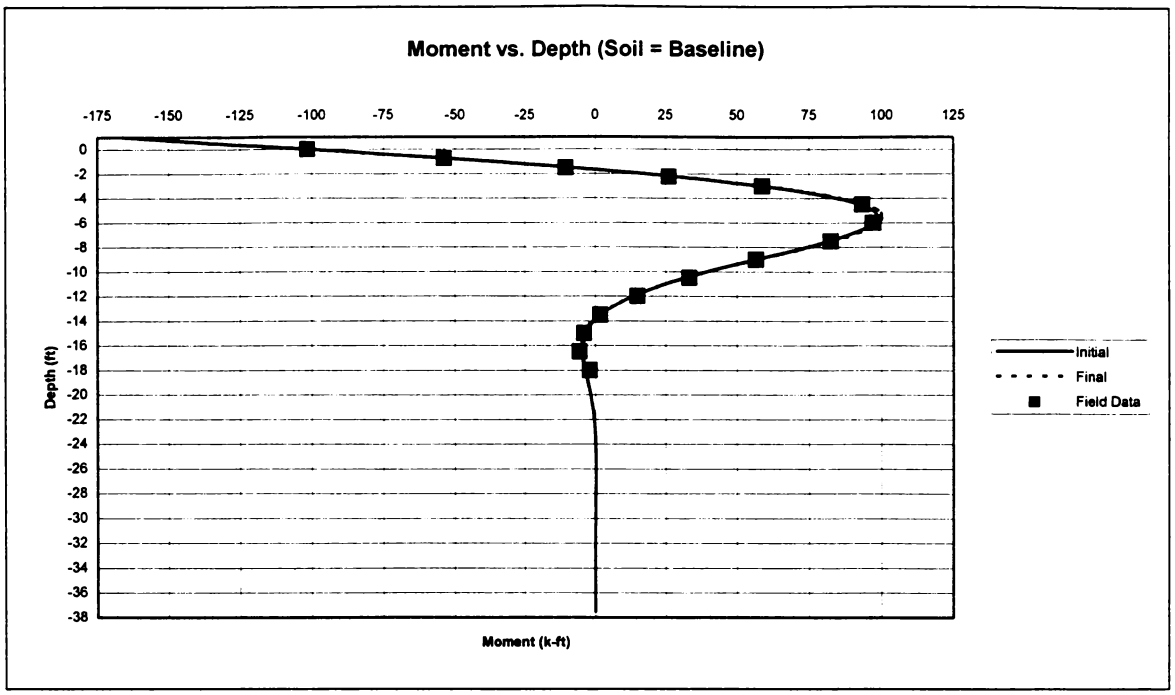


Figure 36: Moment vs. Depth, Constant moment boundary condition (Soil = Baseline)

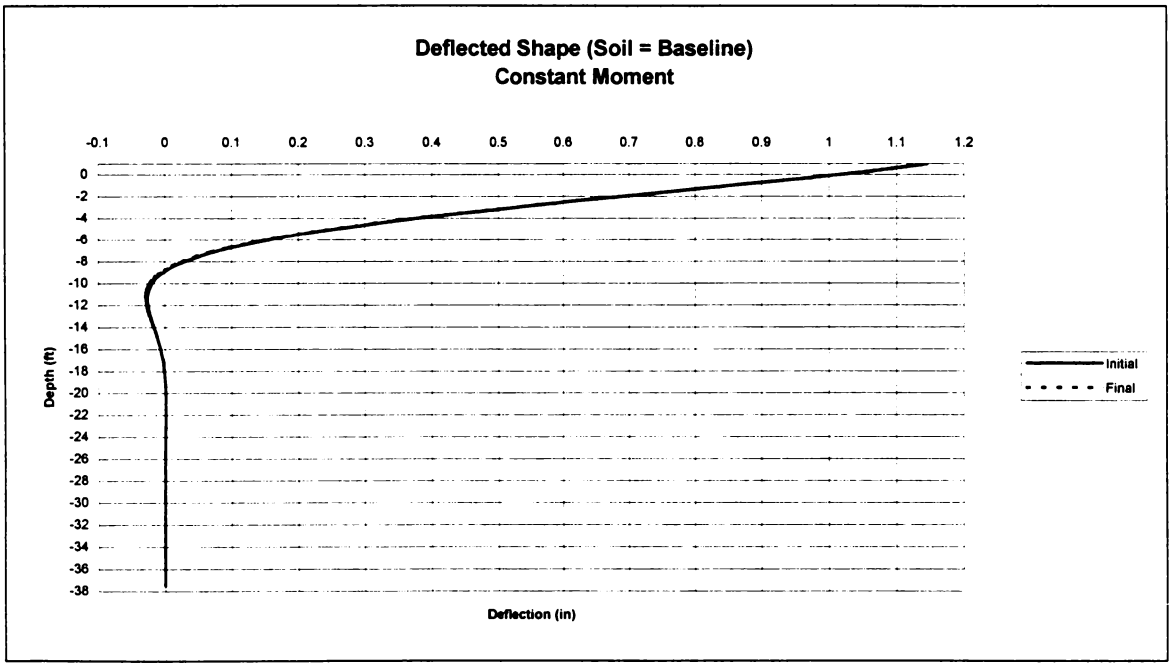


Figure 37: Deflected Shape, Constant moment boundary condition (Soil = Baseline)

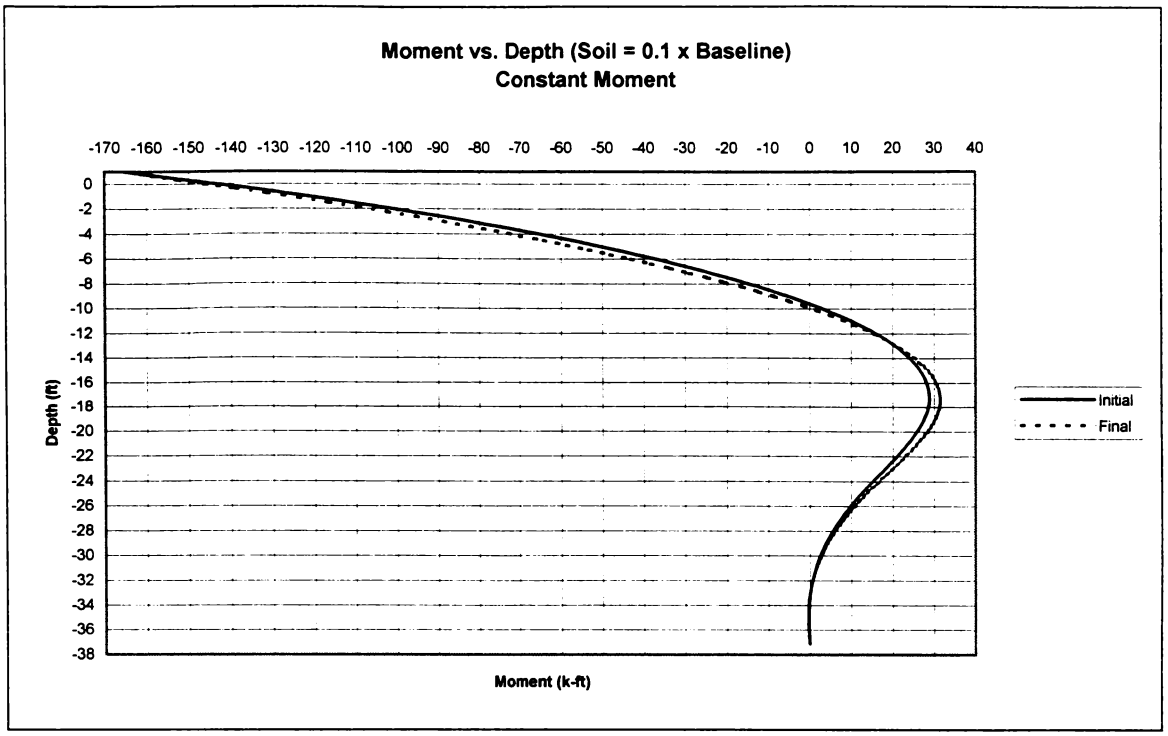


Figure 38: Moment vs. Depth, Constant moment boundary condition (Soil = 10% of Baseline)

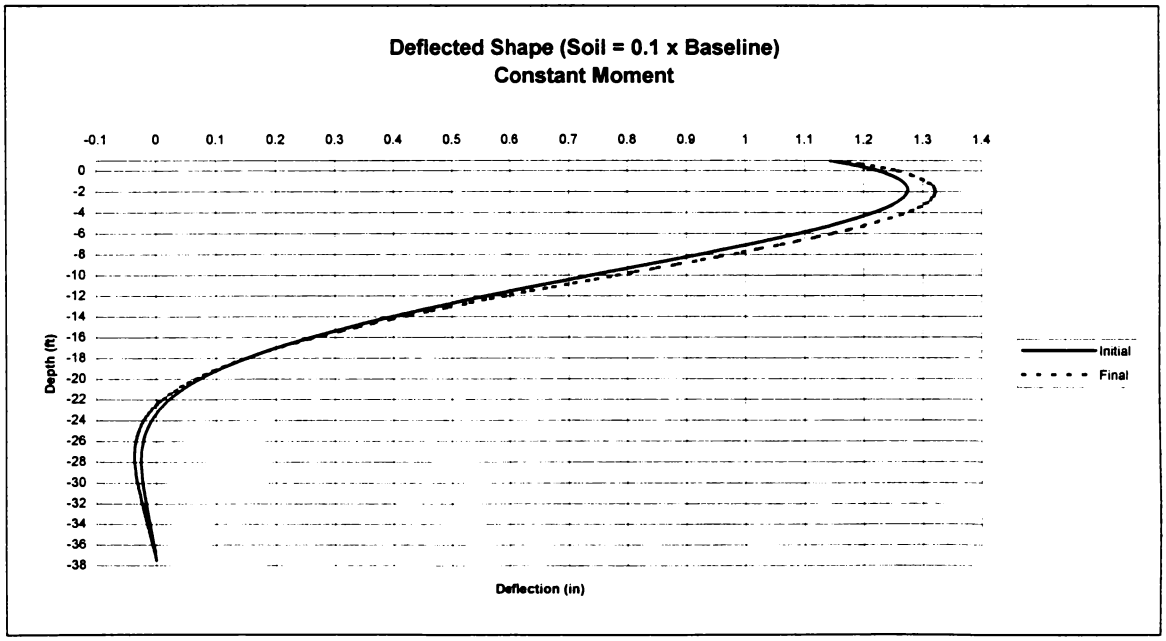


Figure 39: Deflected Shape, Constant moment boundary condition (Soil = 10% of Baseline)

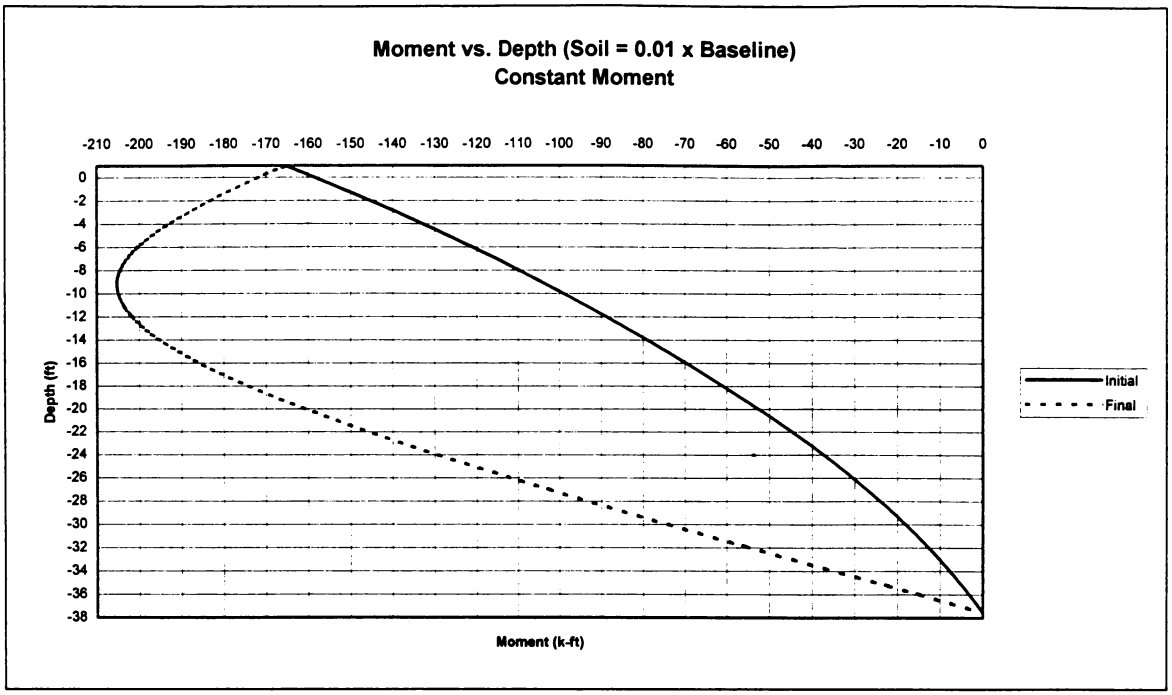


Figure 40: Moment vs. Depth, Constant moment boundary condition (Soil = 1% of Baseline)

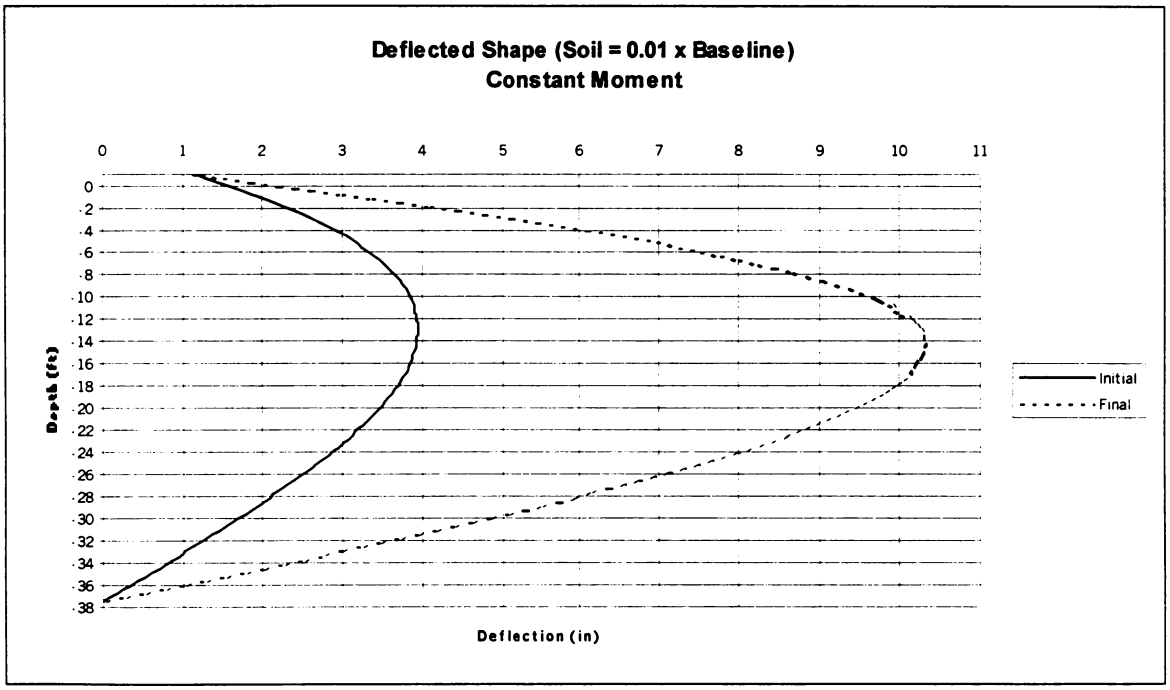


Figure 41: Deflected Shape, Constant moment boundary condition (Soil = 1% of Baseline)

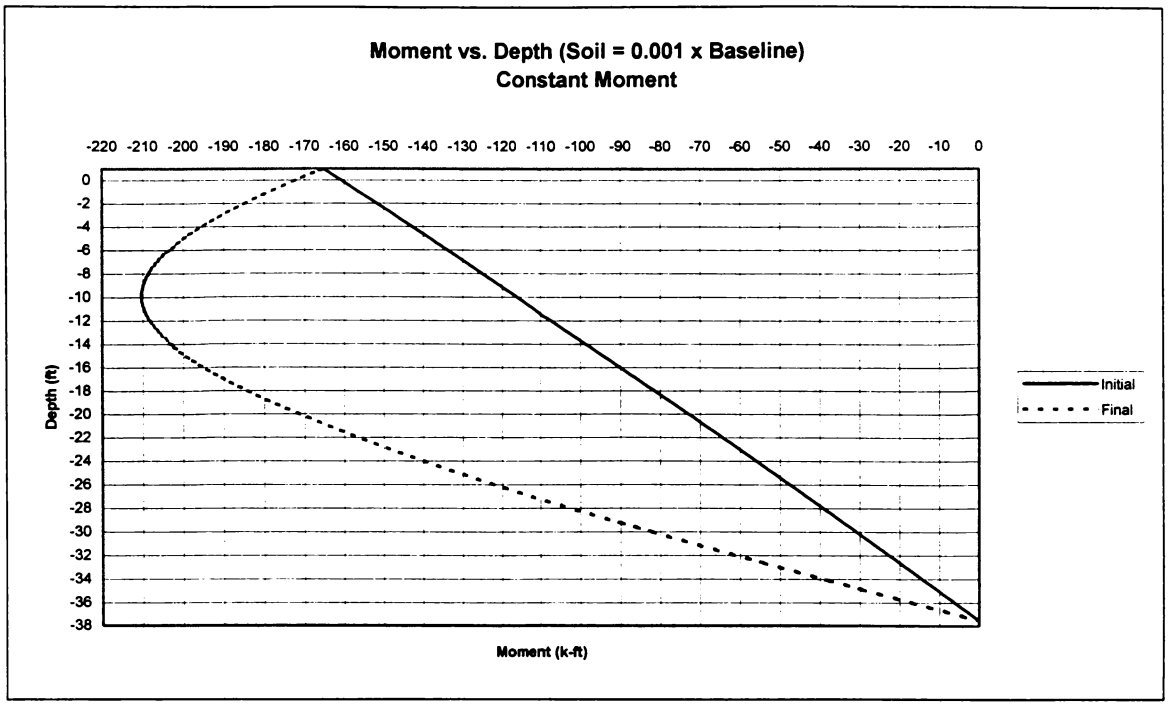


Figure 42: Moment vs. Depth, Constant moment boundary condition (Soil = 0.1% of Baseline)

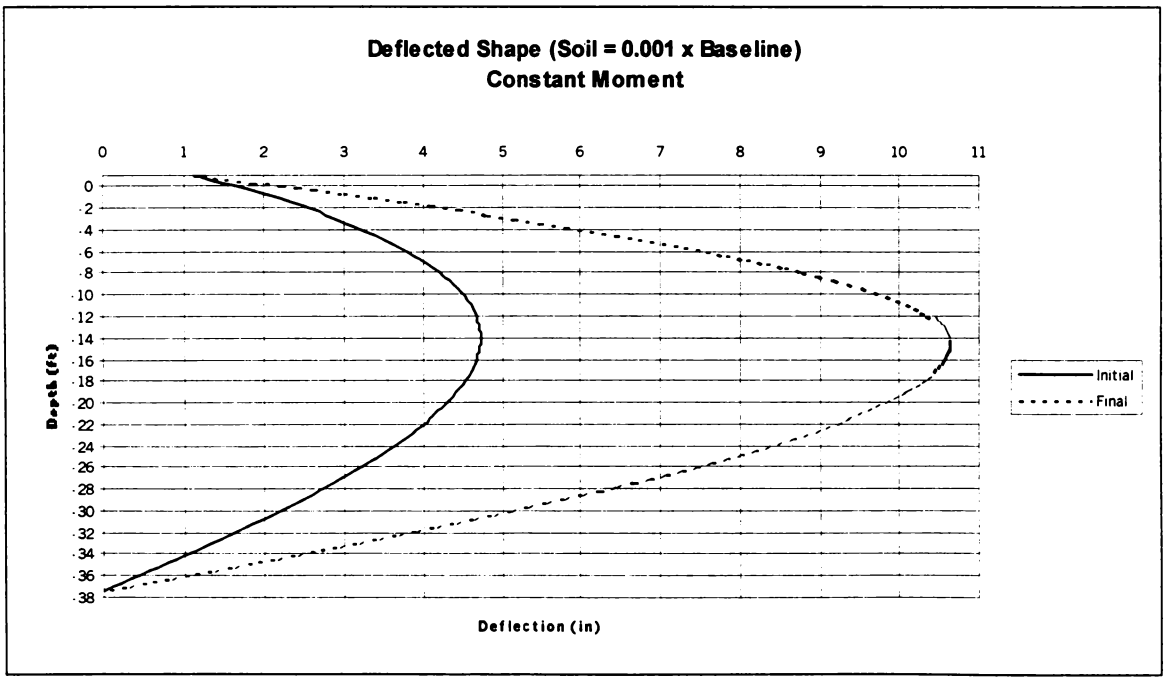


Figure 43: Deflected Shape, Constant moment boundary condition (Soil = 0.1% of Baseline)

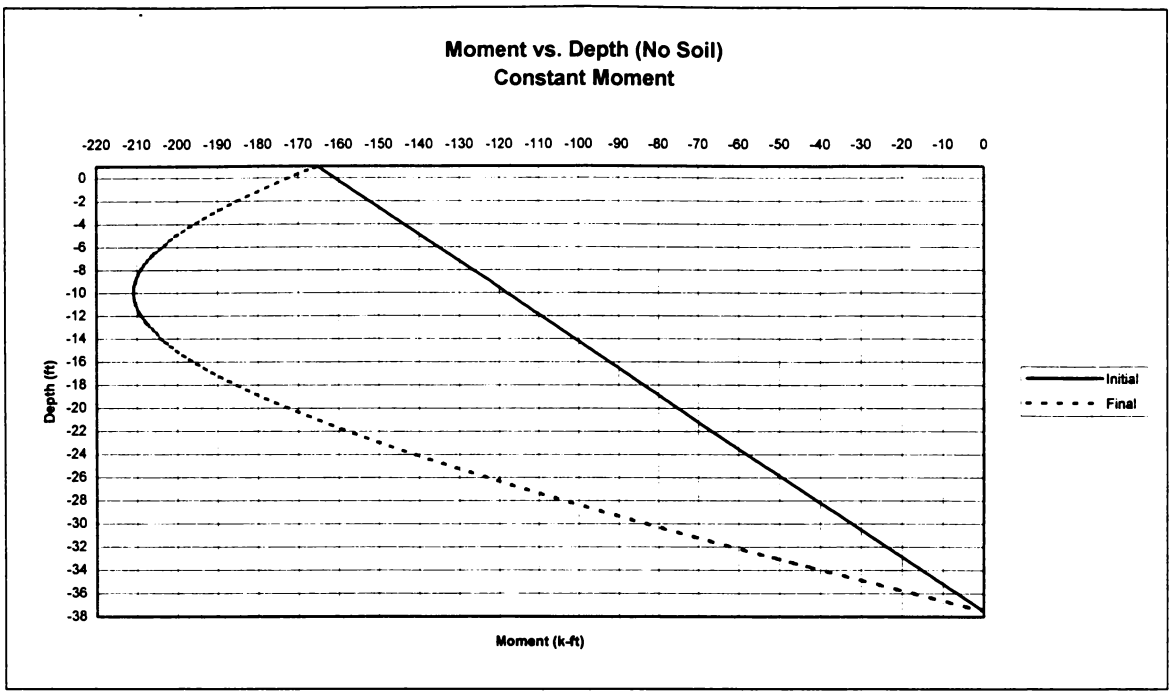


Figure 44: Moment vs. Depth, Constant moment boundary condition (No Soil)

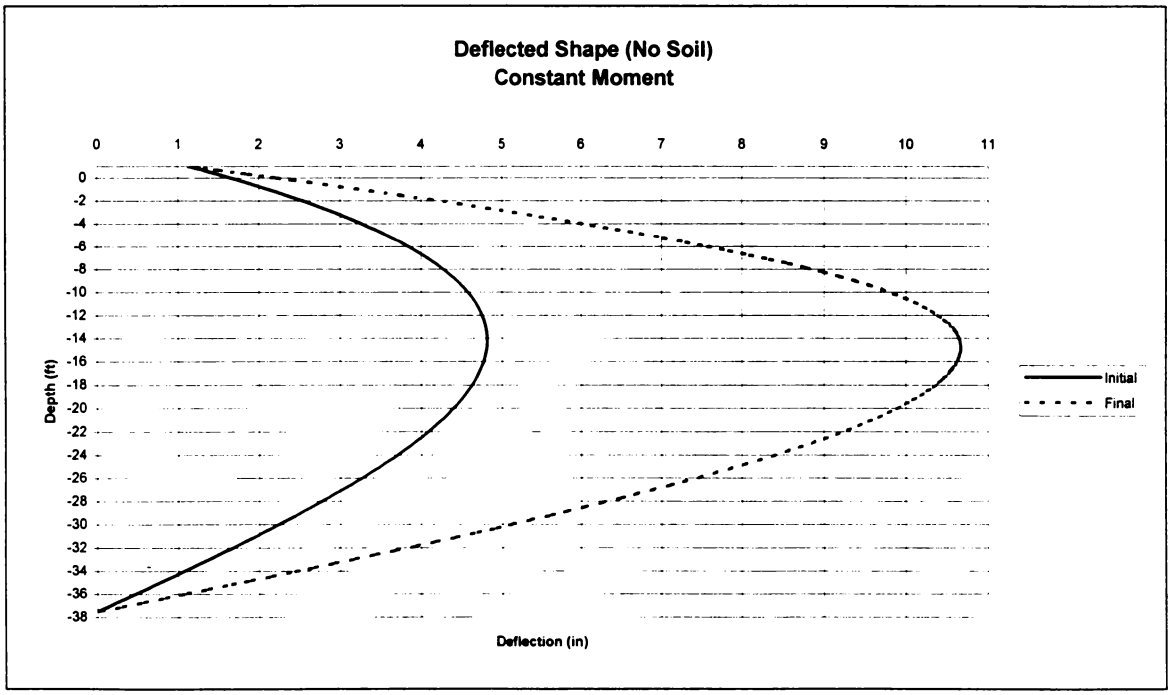


Figure 45: Deflected Shape, Constant moment boundary condition (No Soil)

minimum of the initial plastic limit axial capacities (which are highlighted along with the finite element model capacity) for a given soil strength. Reduced capacity failure is caused by significant moment magnification in either the upper or lower portion of the pile upon the addition of axial load.

In the case of the baseline soil, an insignificant change in the deflected shape occurs after the application of axial load. Therefore, moment magnification due to second order effects is minimal, and the failure load is very near the predicted plastic limit capacity. The plastic limit appears to be an appropriate predictor for this particular case due to sufficient lateral support provided by the soil to prevent instability issues. When the soil stiffness is reduced to 10% of the baseline, the behavior remains basically the same.

Upon further reduction of the soil stiffness to a value equal to 1% of the baseline, a noticeable change in the deflected shape occurs when the axial load is applied. The change in deflected shape is caused by the incapability of the soil to control lateral displacement caused by second order effects, thereby creating instability issues. As lateral displacement is increased due to instability, the second order moment increases until inelastic bending occurs in the highly deflected region of the pile. When the soil stiffness is further reduced, the instability issues become more prevalent. Therefore, the cases of a soil stiffness of 0.1% of the baseline and no soil fail in the same manner at a smaller axial load.

Two anomalies are apparent when studying the deflected shape curves and moment versus depth diagrams for the constant moment models. The first anomaly

pertains to the rotation of the pile head. When an integral abutment experiences lateral displacement, the pile behaves similarly to a laterally loaded column with a nearly fixed connection at the top of the column. A column laterally loaded to the right experiences rotation directly below the top connection in a direction of up and to the right. When experiencing rotation in this manner, the column's deflection directly below the top connection is slightly less than the deflection at the top of the pile. This type of behavior did not occur in the constant moment models (other than the baseline model) due to an excessively large moment applied to the top of the pile. This problem was solved in the second set of models by replacing the applied moment at the top of the pile with a rotational stiffness boundary condition and allowing the naturally occurring moment at the pile head to be calculated.

The second anomaly involved the boundary condition at the base of the pile. When the soil stiffness is reduced to 1% of the baseline, or less, the deflected shape curves indicate that the naturally occurring deflection at a depth of 37.5 feet below the ground surface may not be zero. This anomaly implies that the weaker soil does not have the capability of supplying a large enough lateral load to resist lateral deflection at, or above, the tip of the pile. Shear results from the finite element models show a non-zero shear at the base of the pile, thereby verifying that the weakened soil is not capable of resisting the lateral load and maintaining zero deflection at the pile tip. In the cases of the baseline soil and 10% of the baseline soil, shear at the tip of the pile is very near zero, and it is assumed that the pinned connection at the base of the pile does not affect results.

Rotational Spring Model Results

The second set of models incorporated a rotational spring at the top of the pile to represent the pile-abutment connection. Lateral displacement of the top node was applied to the model as the first load step. The moment distribution, including the magnitude of moment at the top of the pile, was dependent upon the strength of the soil. Axial displacement of the top node was then applied during the second load step, and axial capacity was determined. Figure 46 shows the relationship between axial load and axial deflection for various values of soil stiffness. Table 8 presents the initial and final moment data, as well as the expected axial capacity based upon the plastic limit, and the true axial capacity as determined from the finite element model. With the rotational spring at the top of the pile, moment magnification significant enough to cause a reduction in axial capacity does not occur until the soil stiffness is reduced below 1% of the baseline. The "rotational spring" models are somewhat more stable, and therefore indicate a higher axial capacity, than the "constant moment" models due to a significant reduction in the magnitude of moment distributed along the length of the pile. Figures 47 thru 55 present the moment diagrams and deflected shape diagrams for each of the "rotational spring" models.

Discussion of Rotational Spring Model Results

Table 8 presents results from a set of models that incorporated a rotational spring at the top of the pile to represent the pile-abutment connection. When lateral load was applied to the top of the pile, the rotational spring resisted rotation, thereby inducing

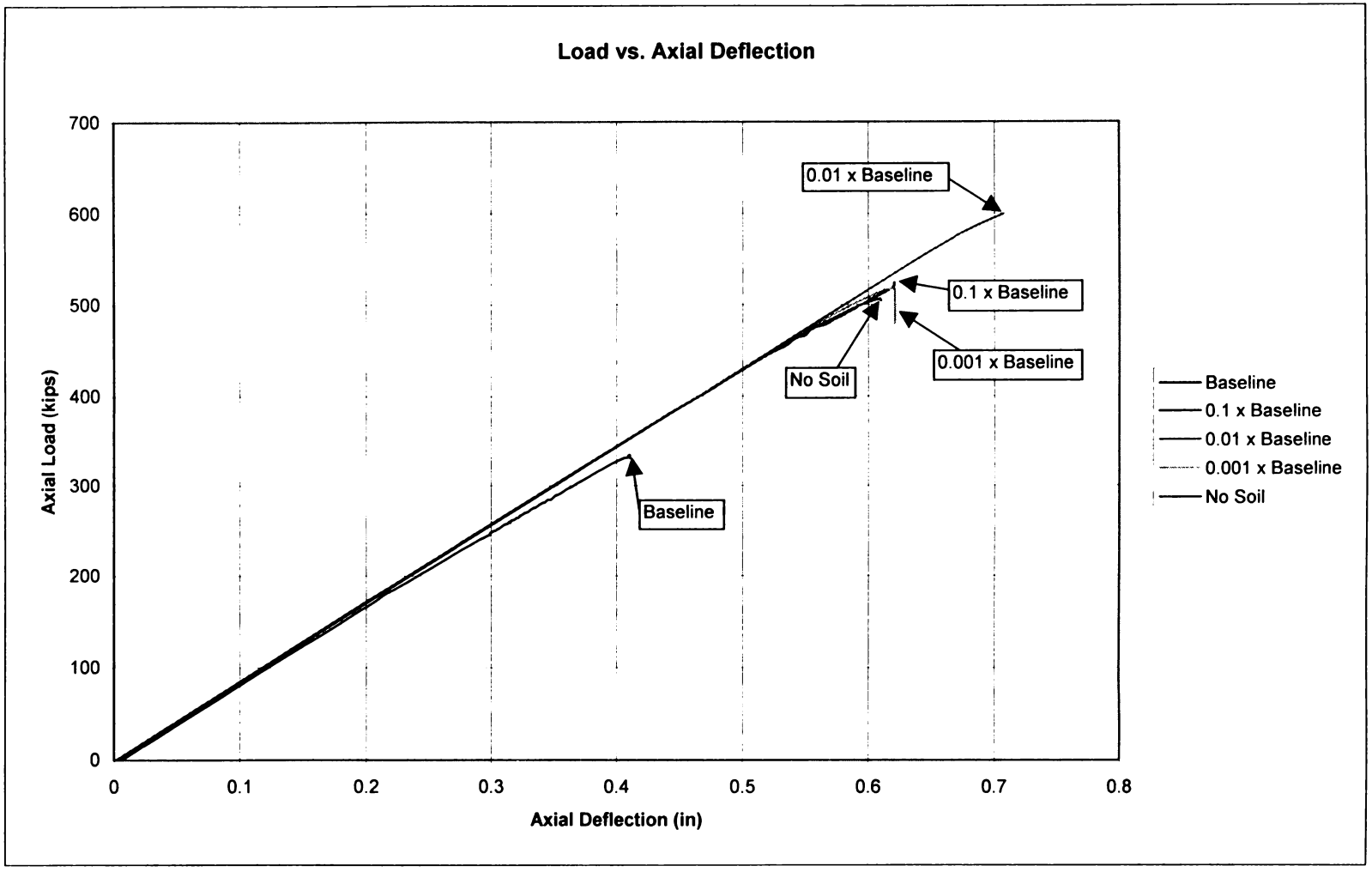


Figure 46: Load vs. Axial Deflection: Rotational Spring Models

Table 8: Rotational Spring Model Results

	Top of Pile				Lower Portion of Pile					
	Initial Load Step		Final Load Step		Initial Load Step		Final Load Step			
Soil Strength (% of Base)	Initial Moment (k-ft)	Plastic Limit Axial Load (kips)	Final Moment (k-ft)	Plastic Limit Axial Load (kips)	Initial Moment (k-ft)	Plastic Limit Axial Load (kips)	Final Moment (k-ft)	Plastic Limit Axial Load (kips)	FE Model Axial Load (kips)	Reduced Capacity?
100	-165.2	231.0	-134.4	313.3	98.6	483.6	102.0	474.8	333.6	No
10	-67.2	488.2	-56.5	515.5	28.1	663.6	34.1	648.5	521.3	No
1	-23.5	598.7	-24.8	595.5	7.8	714.2	19.2	685.8	598.4	No
0.1	-9.2	634.5	48.1	536.8	-8.7	712.0	-61.8	578.3	517.0	Yes
0	-7.3	639.2	53.1	524.1	-7.1	716.0	-66.7	565.8	504.6	Yes

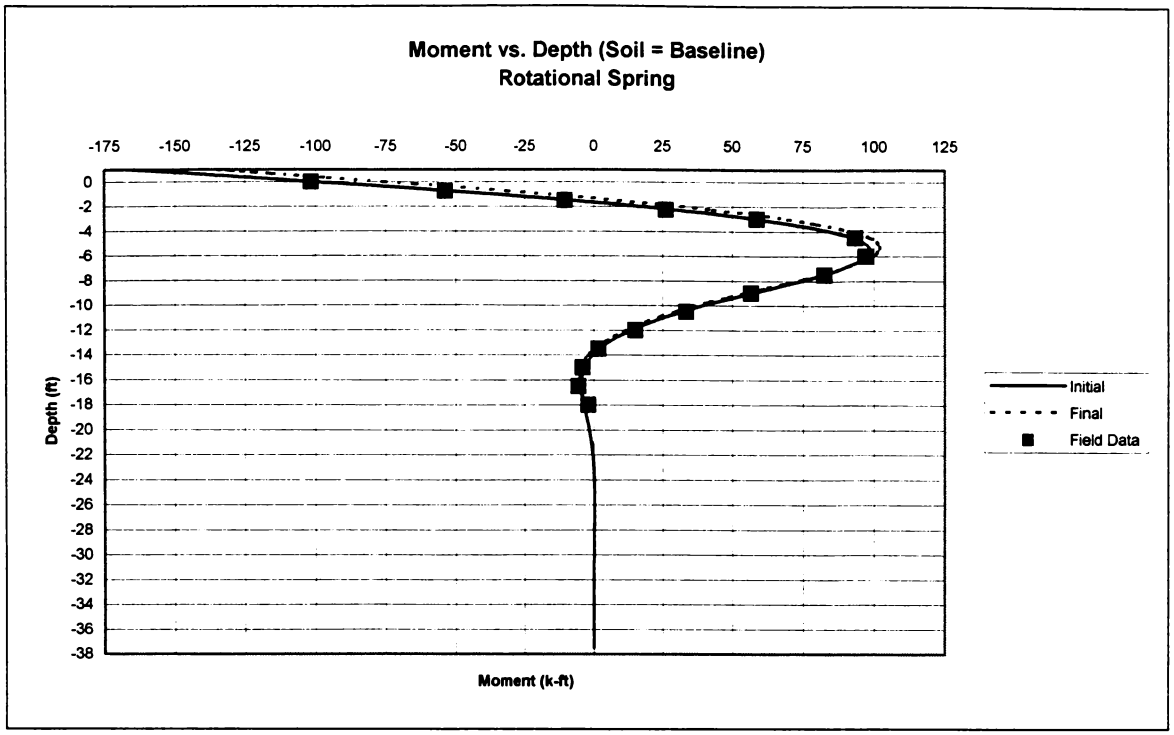


Figure 47: Moment vs. Depth, Rotational spring boundary condition (Soil = Baseline)

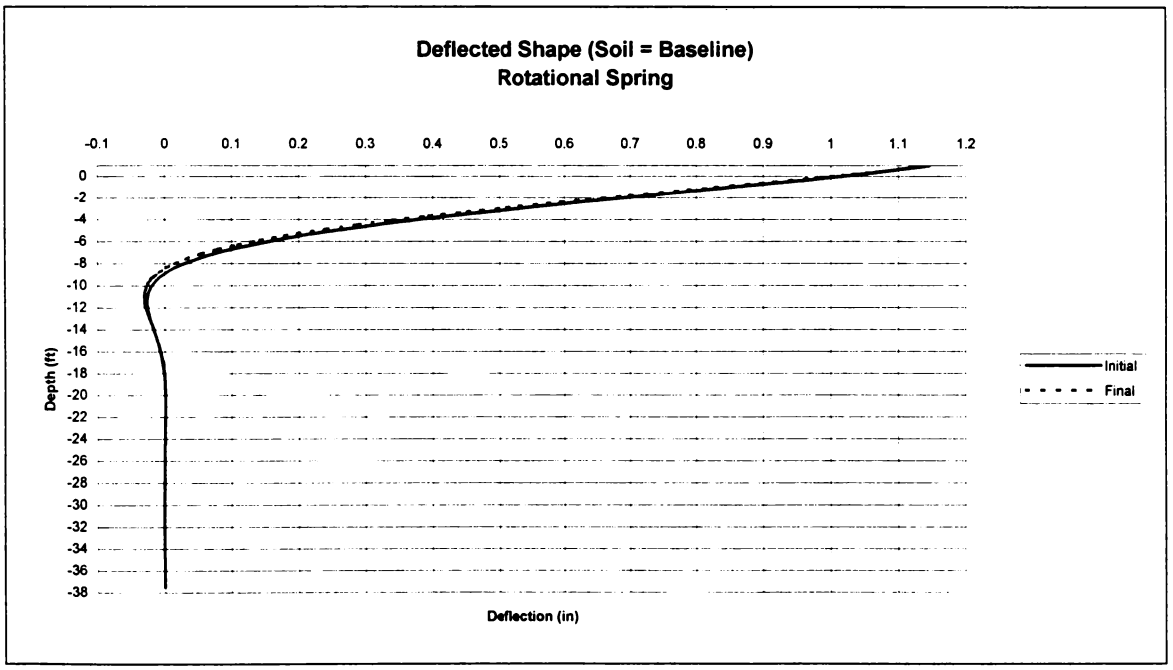


Figure 48: Deflected Shape, Rotational spring boundary condition (Soil = Baseline)

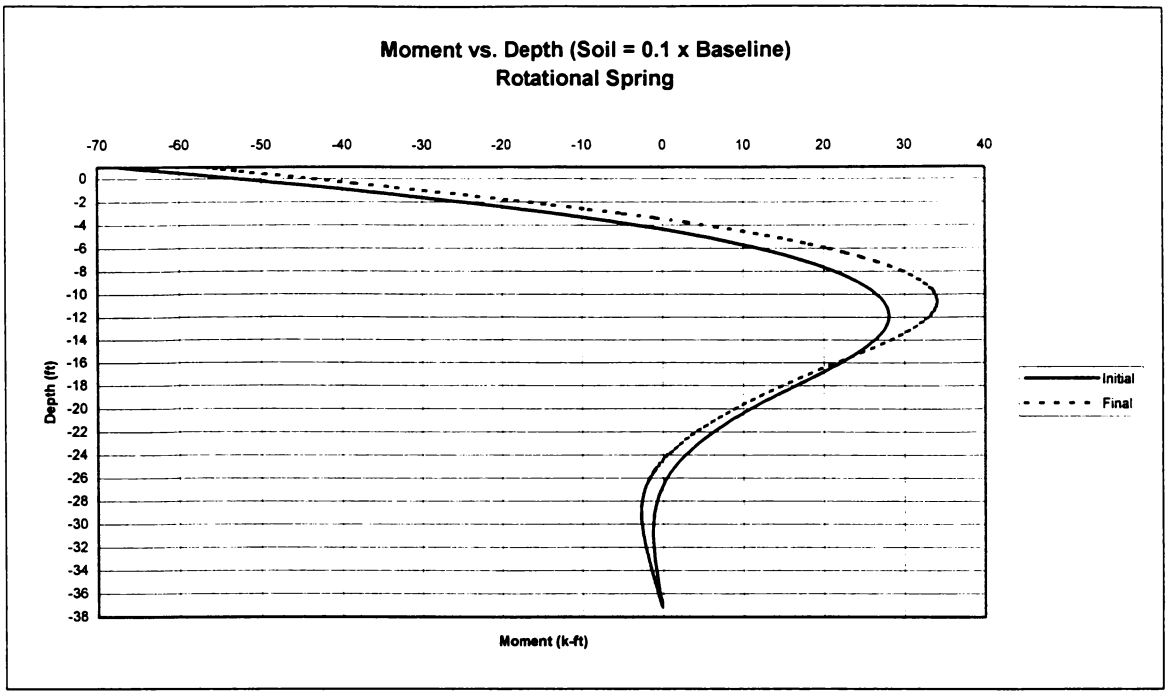


Figure 49: Moment vs. Depth, Rotational spring boundary condition (Soil = 10% of Baseline)

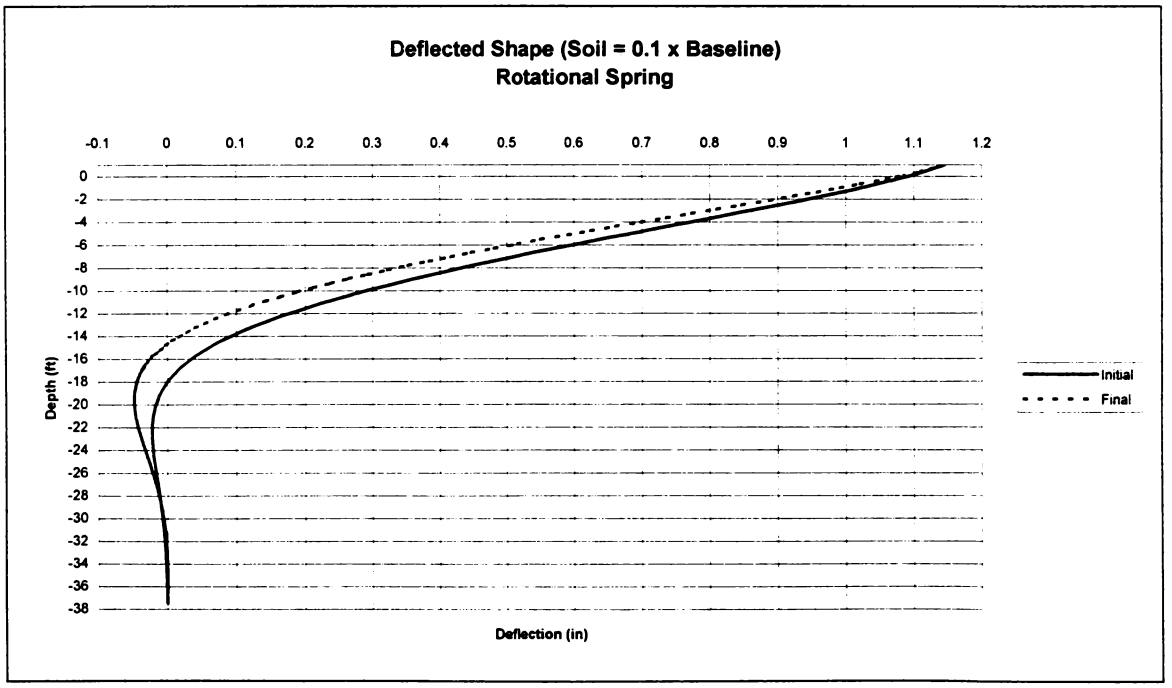


Figure 50: Deflected Shape, Rotational spring boundary condition (Soil = 10% of Baseline)

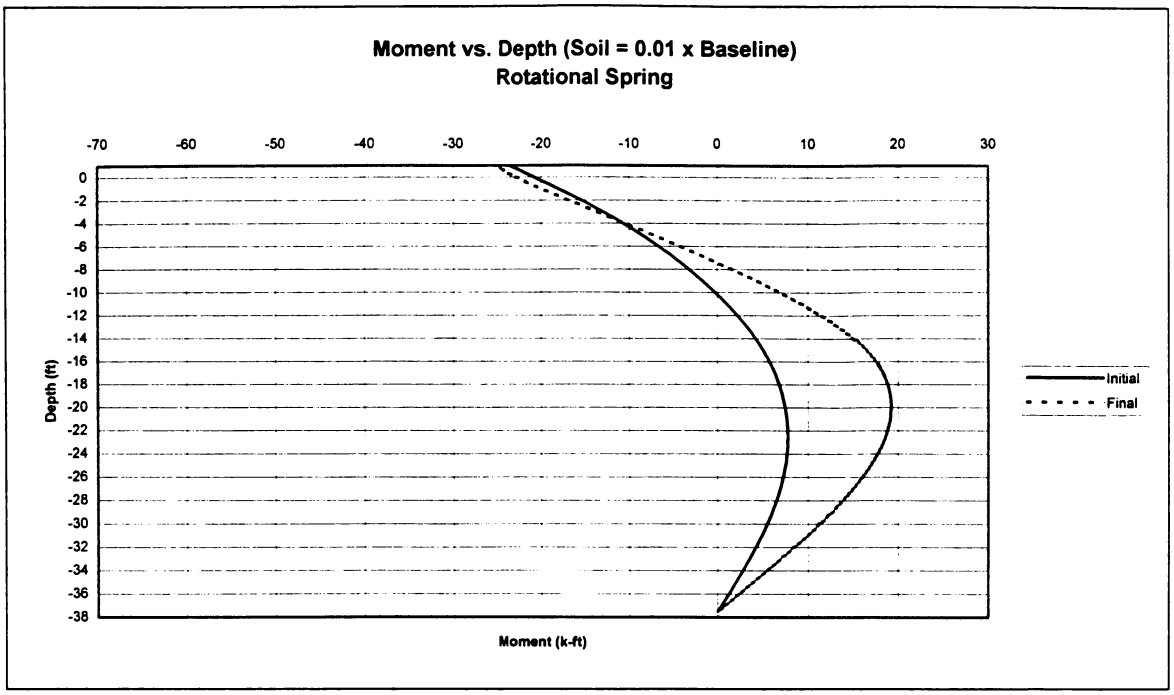


Figure 51: Moment vs. Depth, Rotational spring boundary condition (Soil = 1% of Baseline)

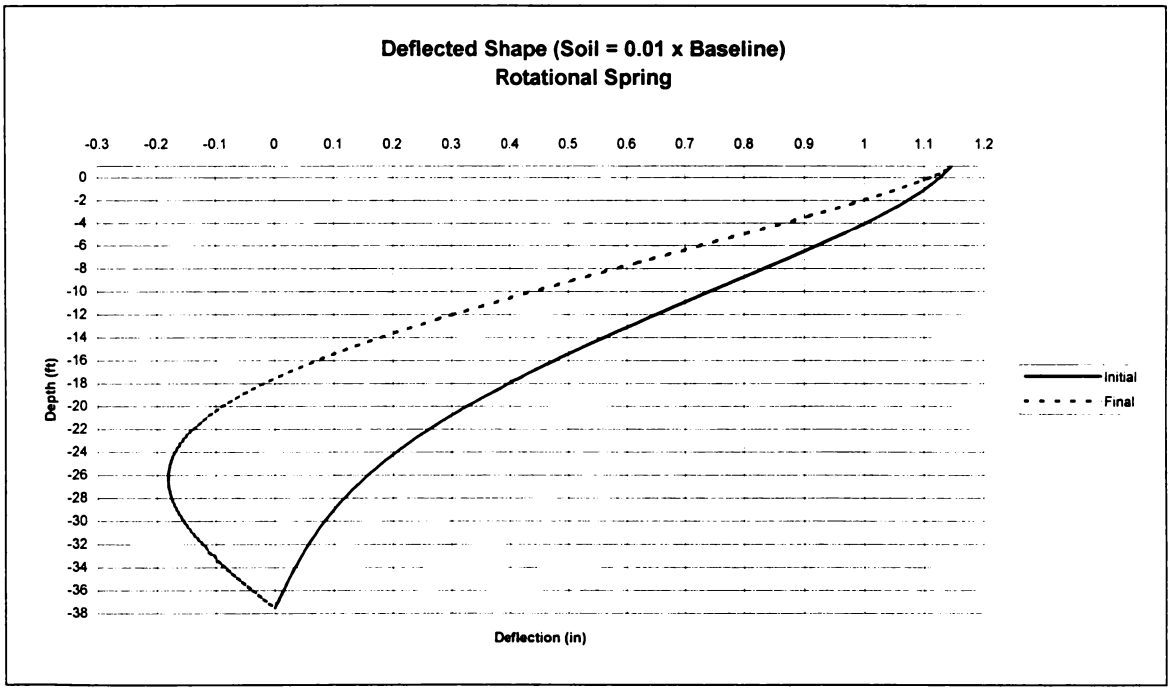


Figure 52: Deflected Shape, Rotational spring boundary condition (Soil = 1% of Baseline)

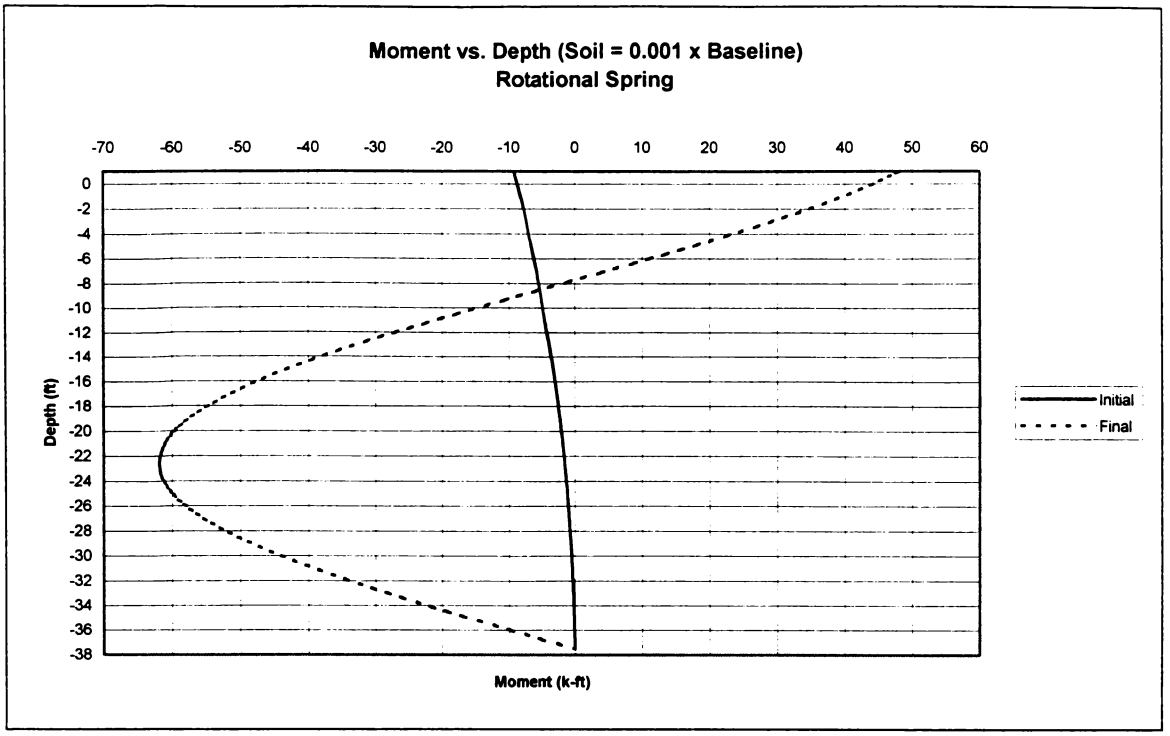


Figure 53: Moment vs. Depth, Rotational spring boundary condition (Soil = 0.1% of Baseline)

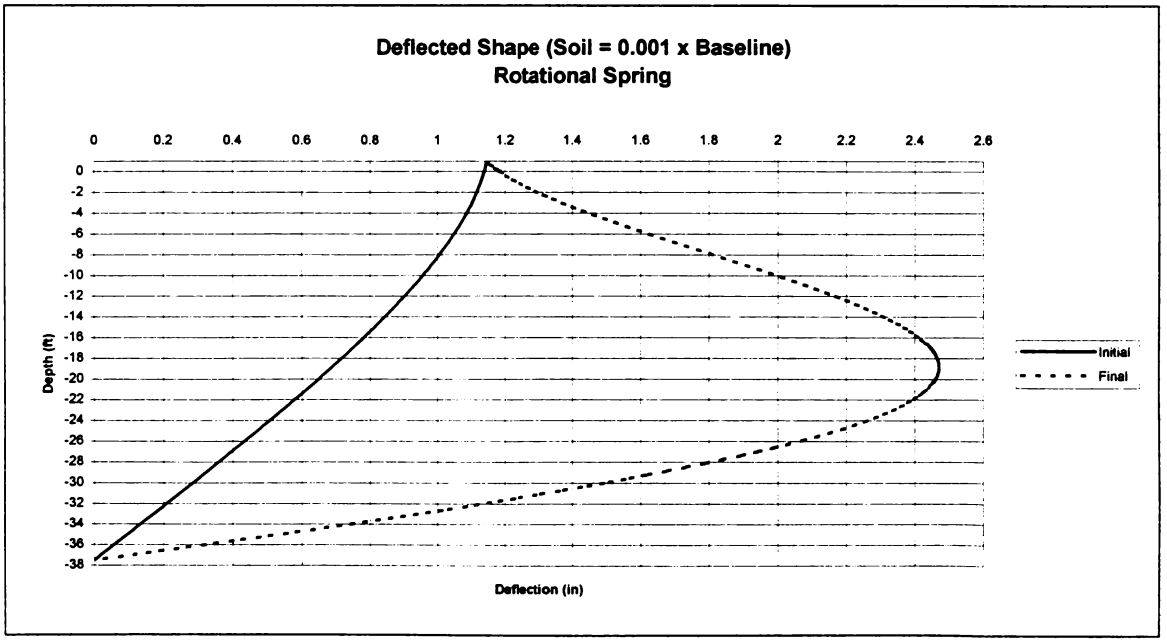


Figure 54: Deflected Shape, Rotational spring boundary condition (Soil = 0.1% of Baseline)

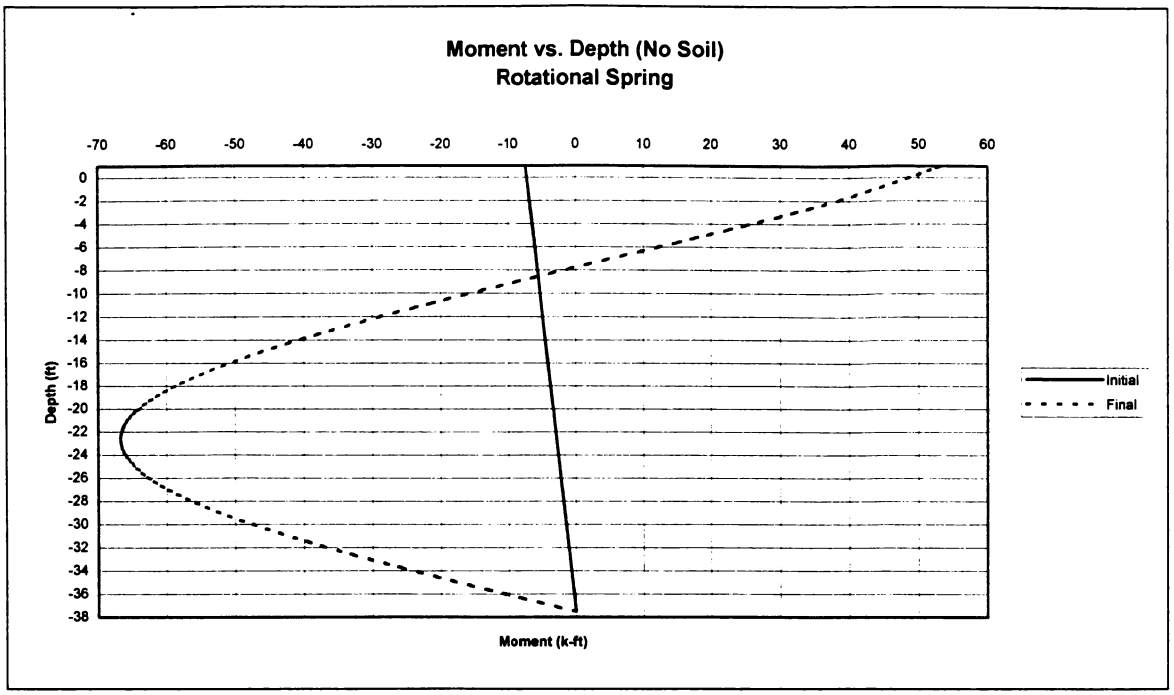


Figure 55: Moment vs. Depth, Rotational spring boundary condition (No Soil)

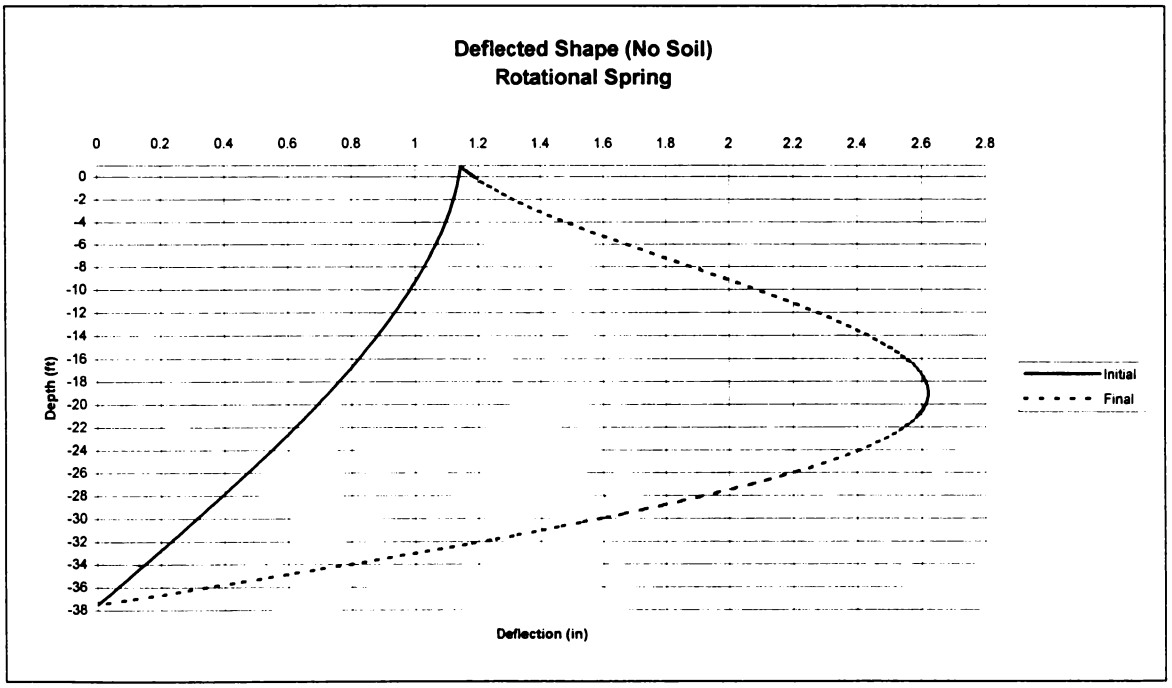


Figure 56: Deflected Shape, Rotational spring boundary condition (No Soil)

moment into the top of the pile. As axial load was applied to the pile, the moment at the pile head was not held constant, and could therefore change due to second order effects.

The deflected shape curves presented in Figure 48 indicate that very little change occurs upon the application of axial load to the baseline soil case. However, Figure 47 shows a partial reduction in moment at the top of the pile. The reduction in moment is caused by the decrease in lateral load required to maintain the lateral displacement after axial load is applied to the out-of-plumb pile. The reduced lateral load overcompensates the second order moment induced at the pile head. Moment in the lower portion of the pile is insignificantly magnified in the presence of sufficient lateral support to prevent instability. The finite element model indicates an axial capacity approximately 100 kips greater than that initially predicted by the plastic limit curve, based on the initial moment induced in the pile, due to the moment reduction at the top of the pile. When soil strength is reduced to 10% of the baseline, the same type of behavior occurs with the exception that the moment reduction is not as large, thereby causing the model predicted axial capacity to only be approximately 30 kips larger than the initially predicted value.

The model utilizing a soil strength of 1% of the baseline produced results approximately equal to the predicted plastic limit capacity. Moment at the top of the pile remained basically unchanged throughout the application of the axial load. The maximum moment in the lower portion of the pile was slightly magnified, but remained less than the moment at the pile head. Therefore, failure occurred at the pile head prior to buckling. Inconsistent with the constant moment model with 1% soil strength, the rotational stiffness boundary condition model resulted in a shear value at the bottom tip

of the pile near zero, implying that the pinned connection at the base of the pile did not significantly affect results for this case.

When soil stiffness was reduced below 1% of the baseline, the horizontal load at the top of the pile required to maintain the initial lateral displacement changed direction and became relatively large after axial load was applied to the out of plumb pile. This horizontal force reversal overcame the second order moment generated at the top of the pile by the axial load and caused a reversal in the moment at the pile head. The final moment at the top of the pile was more than five times larger in magnitude than the original moment after the application of the first load step. The maximum moment in the lower portion of the pile was also greatly magnified, but due to the increased section properties of the pile in the lower region, failure occurred at the pile head. Axial capacity for each of these two cases (0.1% of baseline and no soil) was more than 100 kips less than the predicted plastic limit capacity.

Fixed Rotation Model Results

Axial capacity of a laterally loaded pile is largely dependent upon the magnitude of moment generated in the pile when the top of the pile experiences lateral displacement. Subsequently, the magnitude of moment generated along the length of the pile is dependent upon the rotational stiffness of the pile head. A "worst case" scenario would occur if the pile head were truly "fixed" against rotation.

A third set of models was used to investigate the response of the same pile with a fixed connection at the pile-abutment interface. Results regarding axial load versus axial

deflection for the fixed head models are presented in Figure 57. Table 9 presents the initial and final moment at the top of the pile and the lower portion of the pile, as well as the theoretical plastic limit and the finite element model capacity results. In the case of the baseline soil, the plastic moment was achieved at the top of the pile during the first load step. Therefore, no axial load was applied to the pile for the baseline case. From the results presented in Table 9, one can deduce that until the soil strength is reduced to a value less than 1% of the baseline soil, moment magnification from second order effects is not significant enough to reduce the axial capacity of the pile. Moment versus depth and deflected shape curves for each of the "fixed rotation" models is presented in Figures 58 thru 65.

Discussion of Fixed Pile Head Model Results

The "worst case" scenario for generating the maximum moment at the top of the pile occurs when the pile-abutment connection totally eliminates pile head rotation. A truly fixed connection is not possible in practice, but when the rotational stiffness of a connection is extremely large, pile behavior can closely represent the fixed rotation case. The third set of models incorporated a boundary condition at the top of the pile that eliminated pile head rotation. When the baseline soil model was used, the pile's plastic moment was reached during the first load step (application of lateral load), and therefore no axial load could be applied to the pile.

The other four soil cases investigated responded very similarly to the rotational stiffness boundary condition models. The initial load step for each model generated

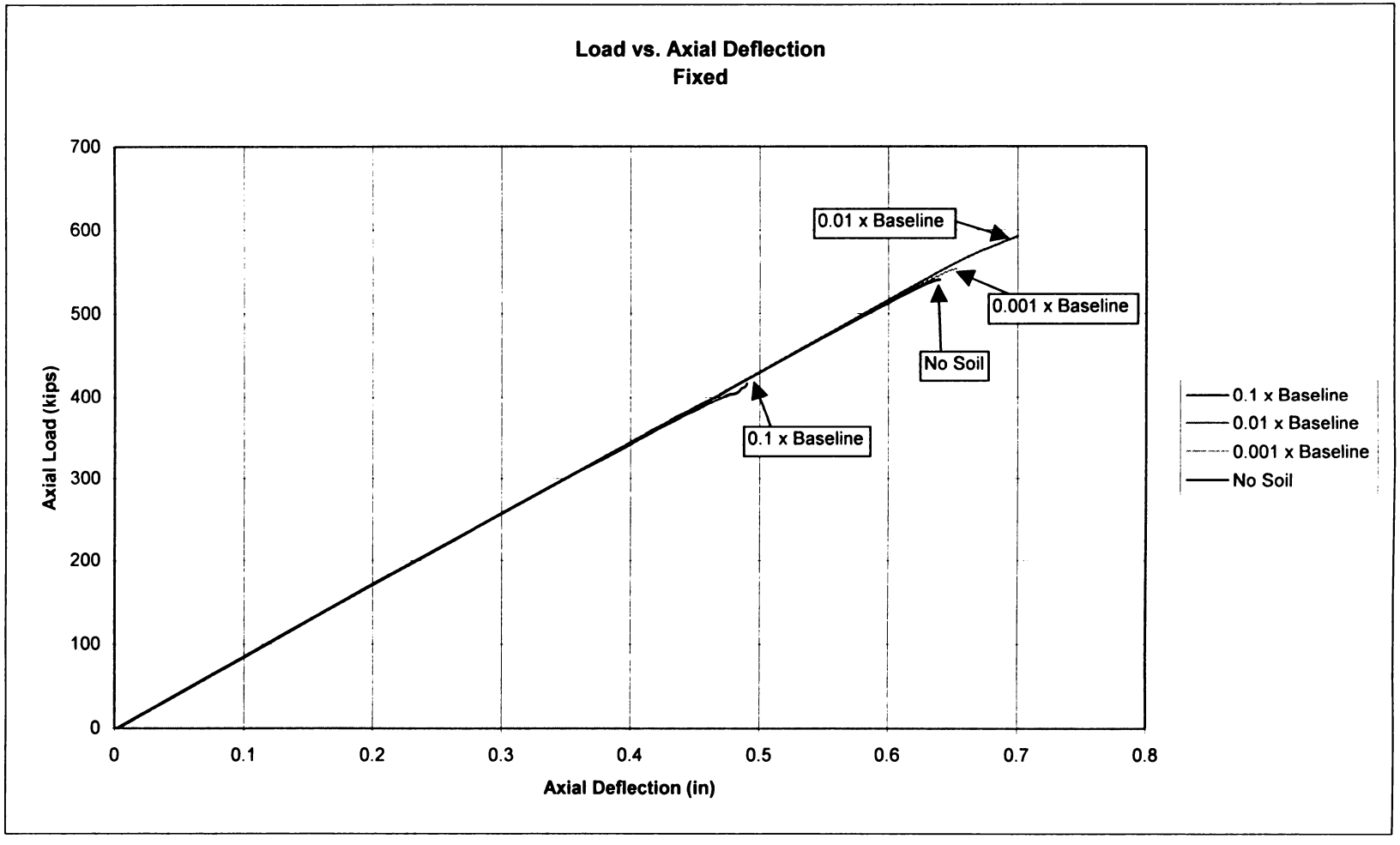


Figure 57: Load vs. Axial Deflection: Fixed Pile Head Models

Table 9: Fixed Pile Head Model Results

	Top of Pile				Lower Portion of Pile					
	Initial Load Step		Final Load Step		Initial Load Step		Final Load Step			
Soil Strength (% of Base)	Initial Moment (k-ft)	Plastic Limit Axial Load (kips)	Final Moment (k-ft)	Plastic Limit Axial Load (kips)	Initial Moment (k-ft)	Plastic Limit Axial Load (kips)	Final Moment (k-ft)	Plastic Limit Axial Load (kips)	FE Model Axial Load (kips)	Reduced Capacity?
100	-234.5	0.0	N/A	N/A	N/A	N/A	N/A	N/A	N/A	N/A
10	-99.2	405.7	-90.3	428.8	27.1	666.1	30.6	657.3	414.8	No
1	-29.0	585.0	-27.1	589.7	6.9	716.5	18.0	688.8	592.5	No
0.1	-11.0	629.9	37.9	562.6	-10.4	707.8	-45.3	620.2	553.5	Yes
0	-8.7	635.6	42.5	551.0	-8.5	712.5	-49.0	610.9	540.5	Yes

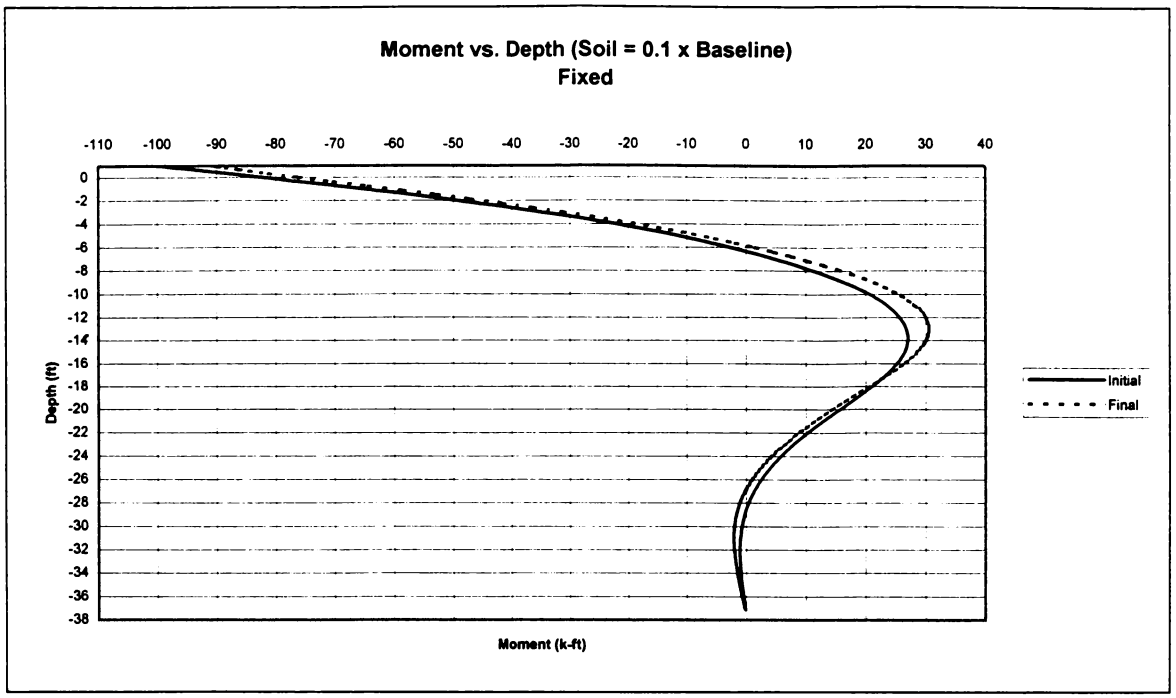


Figure 58: Moment vs. Depth, Fixed pile head boundary condition (Soil = 10% of Baseline)

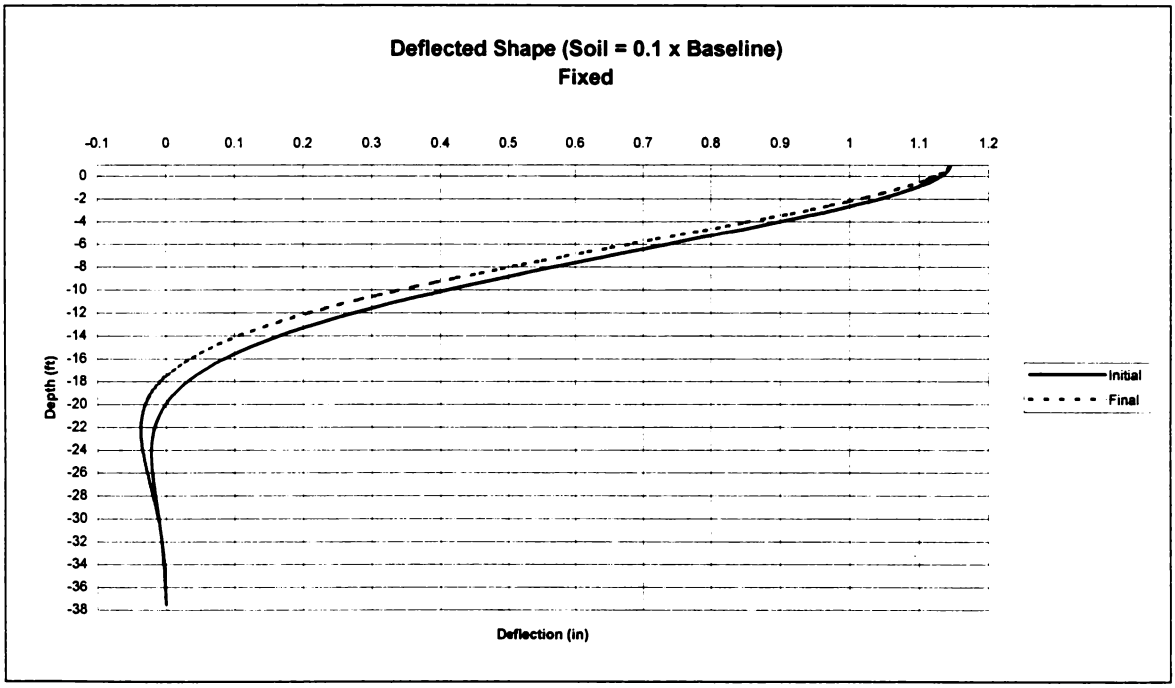


Figure 59: Deflected Shape, Fixed pile head boundary condition (Soil = 10% of Baseline)

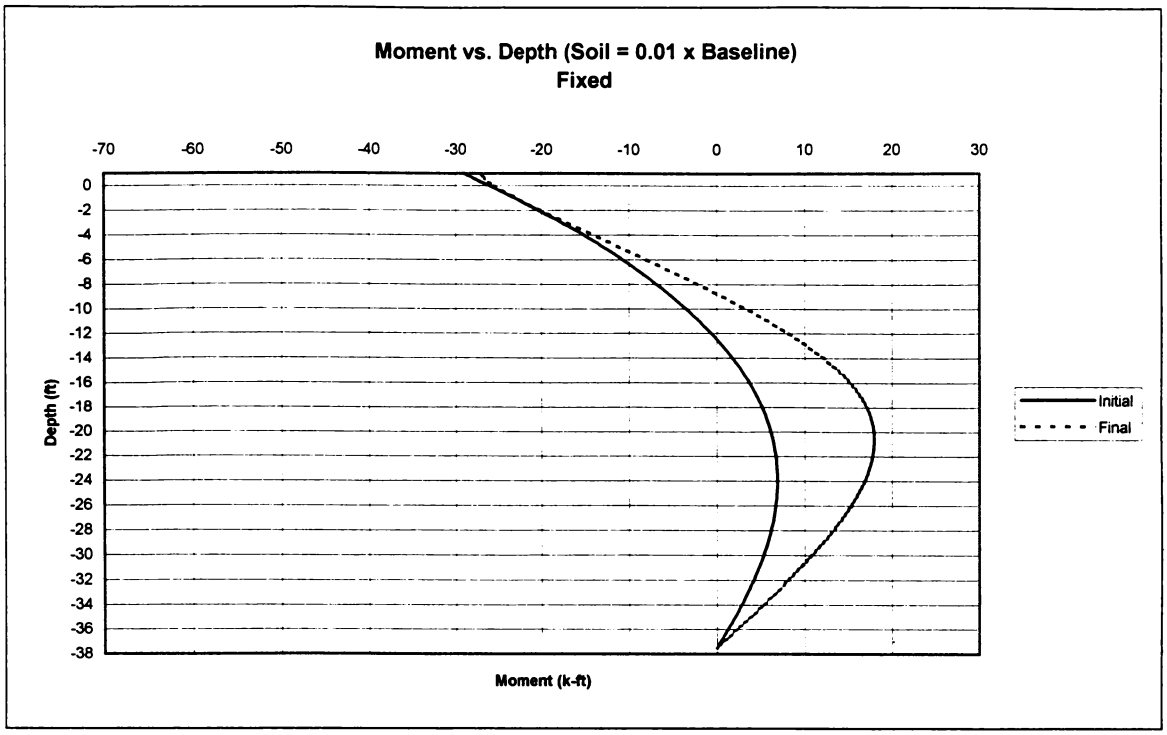


Figure 60: Moment vs. Depth, Fixed pile head boundary condition (Soil = 1% of Baseline)

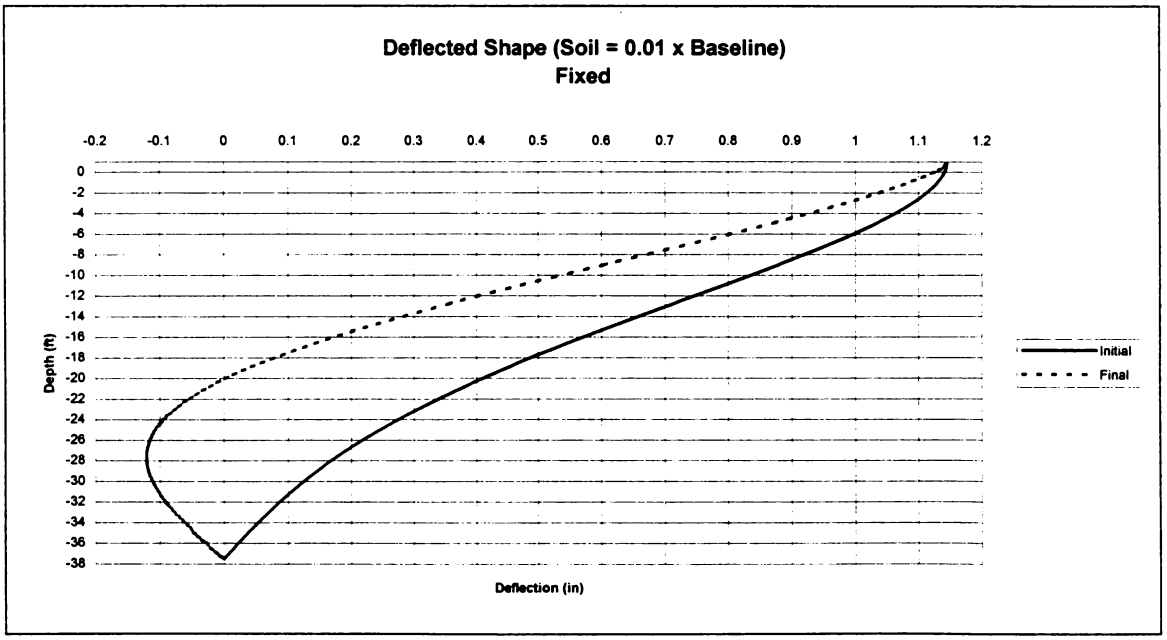


Figure 61: Deflected Shape, Fixed pile head boundary condition (Soil = 1% of Baseline)

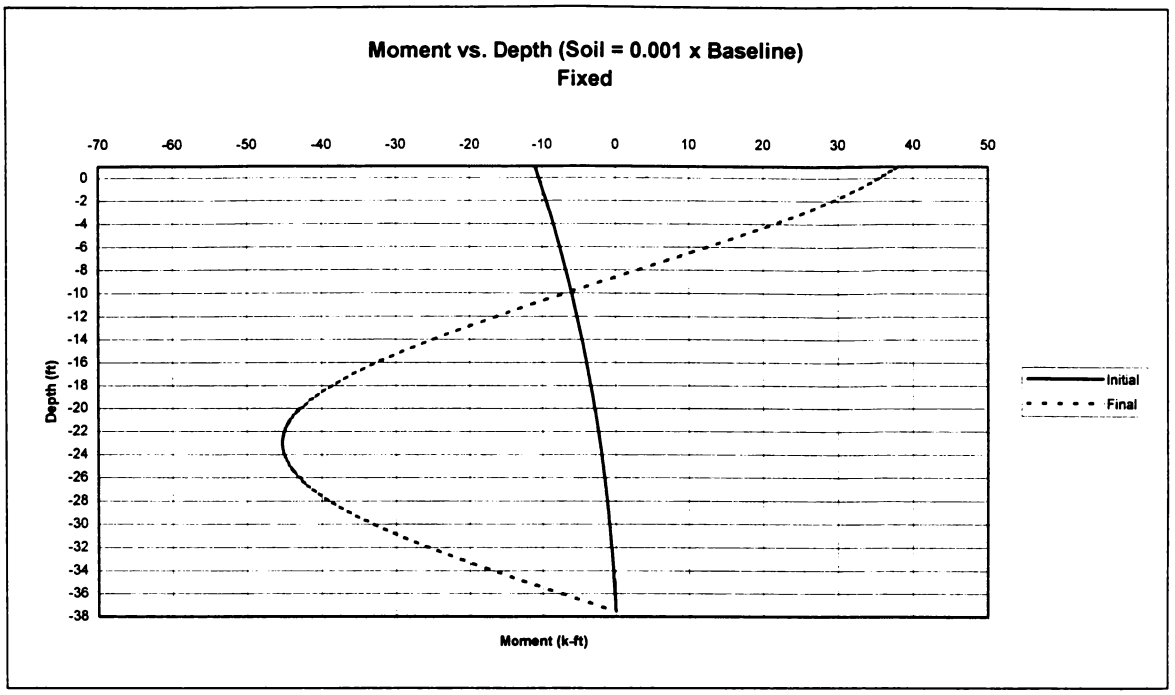


Figure 62: Moment vs. Depth, Fixed pile head boundary condition (Soil = 0.1% of Baseline)

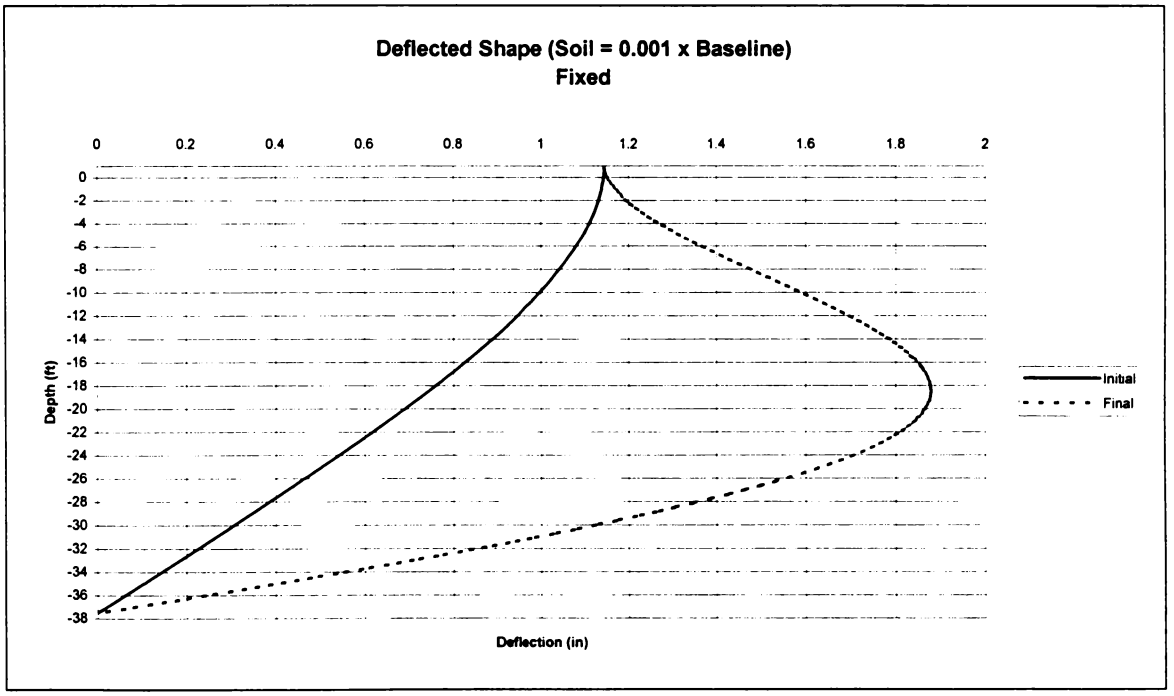


Figure 63: Deflected Shape, Fixed pile head boundary condition (Soil = 0.1% of Baseline)

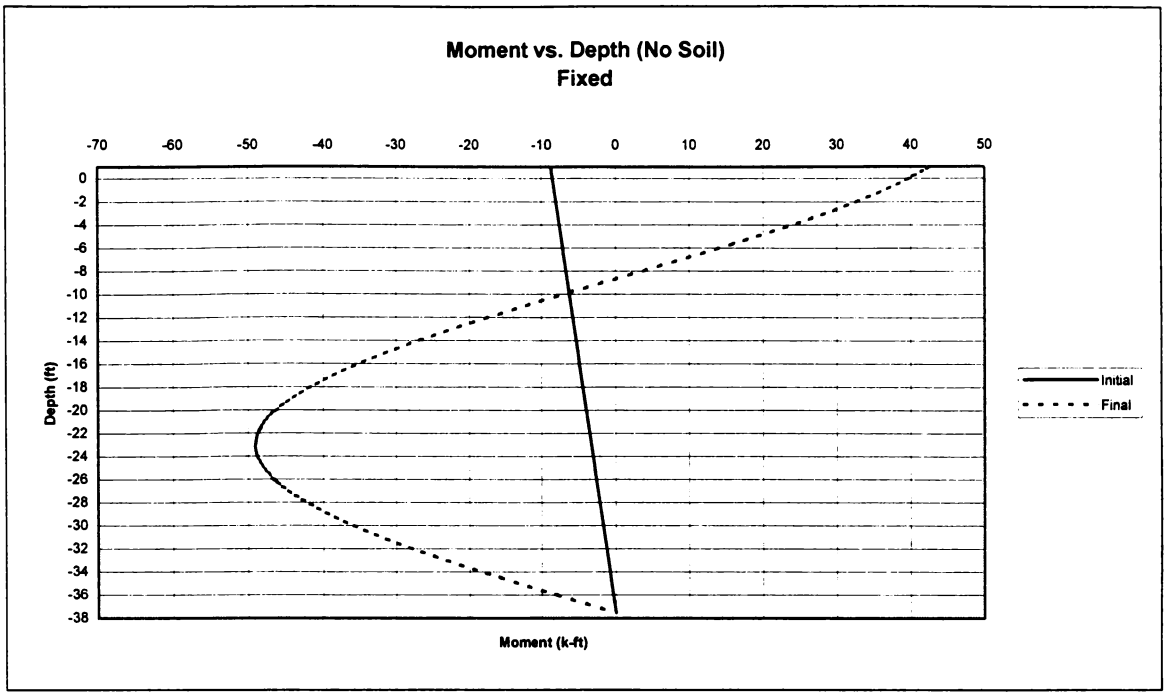


Figure 64: Moment vs. Depth, Fixed pile head boundary condition (No Soil)

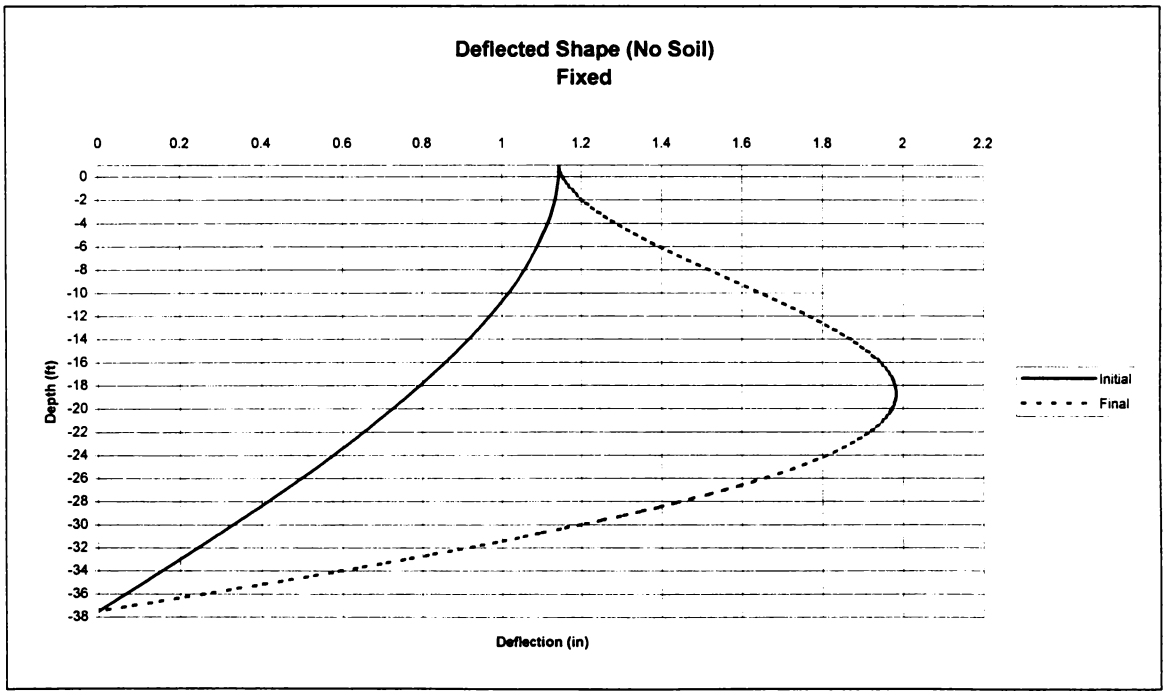


Figure 65: Deflected Shape, Fixed pile head boundary condition (No Soil)

slightly higher moment magnitudes at the top of the pile than did the rotational stiffness models. When soil stiffness was set to 10% and 1% of the baseline, the moment at the top of the pile slightly decreased as the axial load increased. Again, this phenomenon was due to a decrease in the lateral force required to maintain the initial lateral displacement of the pile head. The maximum moment in the lower portion of the pile increased minimally after axial load application due to the soil's ability to prevent instability issues.

When surrounded by a soil equivalent to 0.1% of the baseline or no soil at all, the reduction of lateral force required to maintain the initial lateral displacement reversed direction and caused a reversal of moment at the pile head. Failure ultimately occurred when the magnitude of moment at the top of the pile increased to a value consistent with the plastic limit moment associated with the applied axial load. Moment magnification caused failure prior to achieving an axial load initially predicted by the plastic limit curve.

50% Gap Model Results

The final set of models incorporated a rotational spring at the top of the pile to represent the pile-abutment connection and a gap between the pile and soil in the upper six feet equal to 50% of the initial lateral displacement experienced by the original rotational spring models. The gap depth of six feet was chosen based on the rotational spring model deflected shape curve for the baseline soil case (Figure 48). The horizontal displacement at the six foot elevation presented in Figure 48 is approximately 0.15

inches. An assumption was made that for any horizontal displacement less than 0.15 inches, full recovery of the soil would occur and no gap would be present. It was then conservatively assumed that nearly all of the soil displacement at the ground elevation would be unrecoverable. For simplicity of implementation into the finite element model, an average recovery of 50% was then assumed for the upper six feet of pile.

Upon pile-soil contact, the soil in the region where the gap was present was assumed to retain its original load-displacement curve. A typical force-displacement curve for the soil in the region of the gap is shown in Figure 66. Load was applied to the 50% gap models in the same manner as described for the rotational stiffness boundary condition models. Table 10 presents the initial and final moment data, as well as the expected axial capacity based upon the plastic limit, and the true axial capacity as determined from the finite element model. A comparison of initial moment versus depth between the rotational stiffness models and the gap models is shown in Figures 67 and 68, while a comparison of the initial deflected shapes is shown in Figures 69 and 70. Figures 71 thru 74 illustrate initial and final moment versus depth and deflected shape curves for the gap models. With the presence of a gap between the pile and the soil at the upper elevations, the moment magnitude at the top of the pile and in the lower region of the pile is reduced. This phenomenon is more evident in the case of a very stiff soil. The reduction in moment at the top of the pile allows for a slight increase in axial capacity. No evidence was apparent supporting the intuitive thought that the gap would provoke instability.

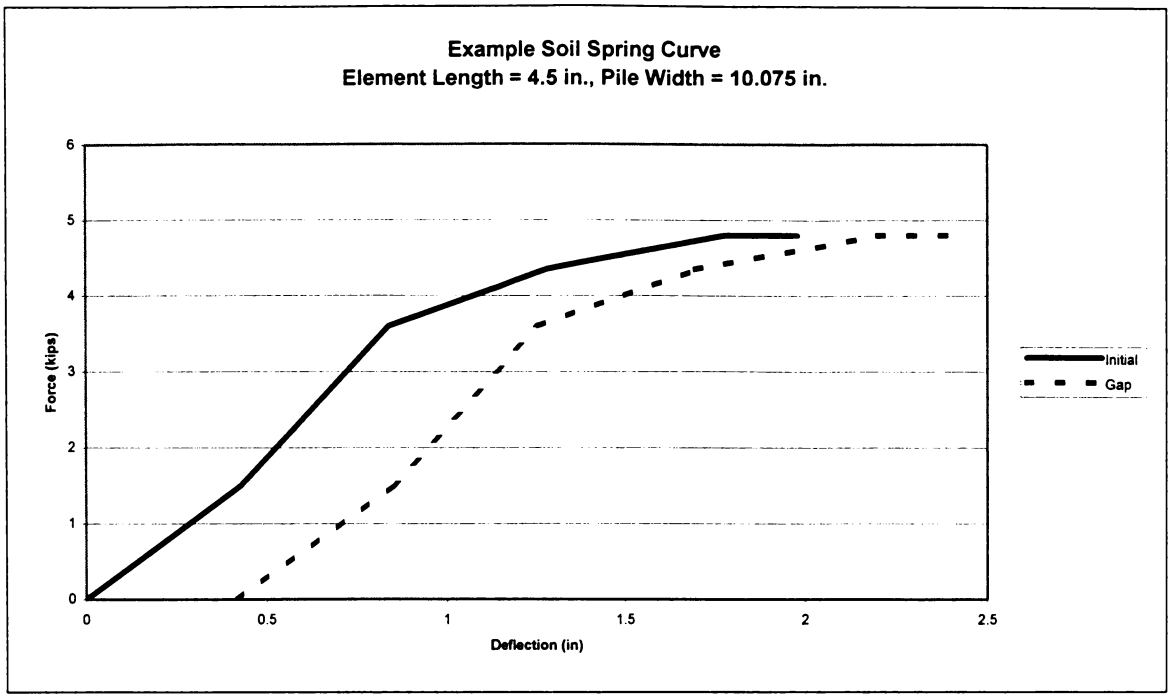


Figure 66: Example Soil Spring Curve (with and without gap)

Table 10: 50% Gap Model Results

	Top of Pile				Lower Portion of Pile					
	Initial Load Step		Final Load Step		Initial Load Step		Final Load Step			
Soil Strength (% of Base)	Initial Moment (k-ft)	Plastic Limit Axial Load (kips)	Final Moment (k-ft)	Plastic Limit Axial Load (kips)	Initial Moment (k-ft)	Plastic Limit Axial Load (kips)	Final Moment (k-ft)	Plastic Limit Axial Load (kips)	FE Model Axial Load (kips)	Reduced Capacity?
100	-139.6	299.5	-127.9	330.5	79.3	533.5	80.8	529.6	327.1	No
10	-62.9	499.2	-50.7	530.2	27.5	665.1	33.3	650.5	521.3	No

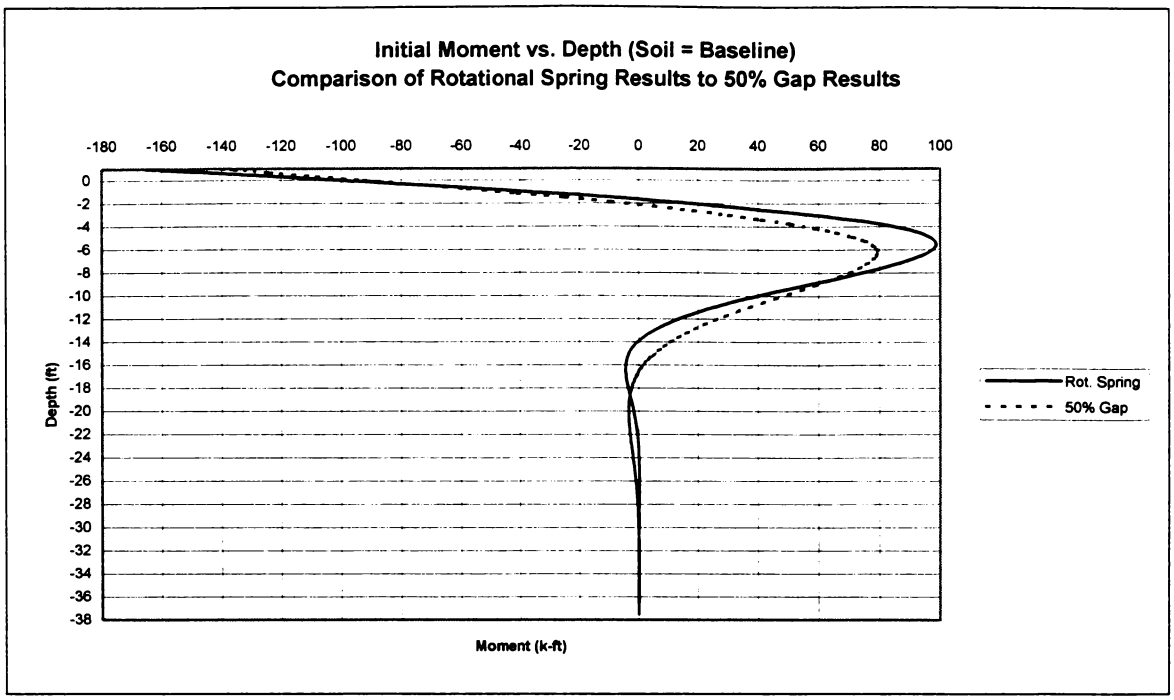


Figure 67: Initial Moment vs. Depth Comparison (Soil = Baseline)

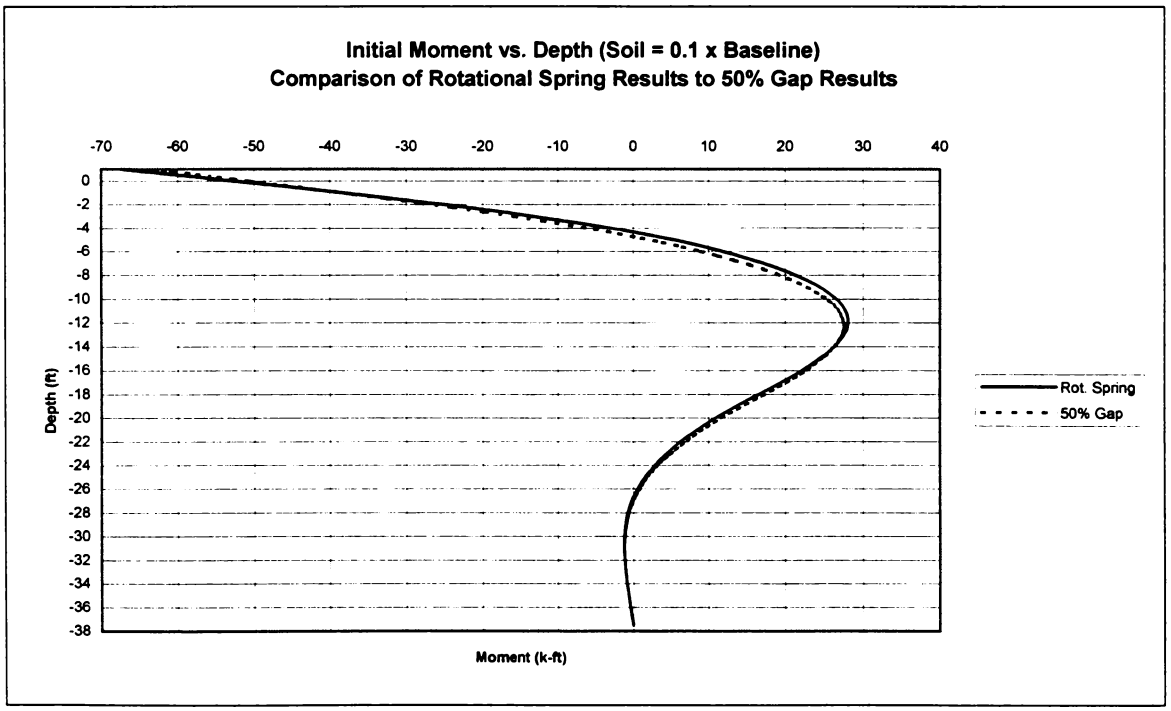


Figure 68: Initial Moment vs. Depth Comparison (Soil = 0.1 x Baseline)

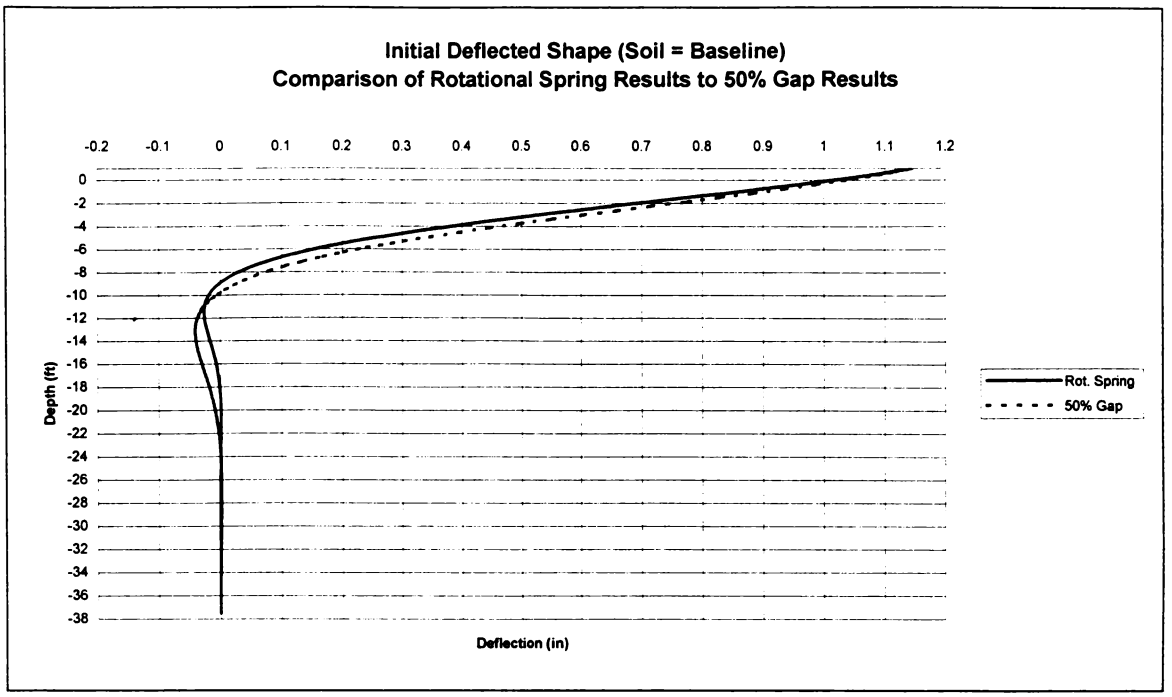


Figure 69: Initial Deflected Shape Comparison (Soil = Baseline)

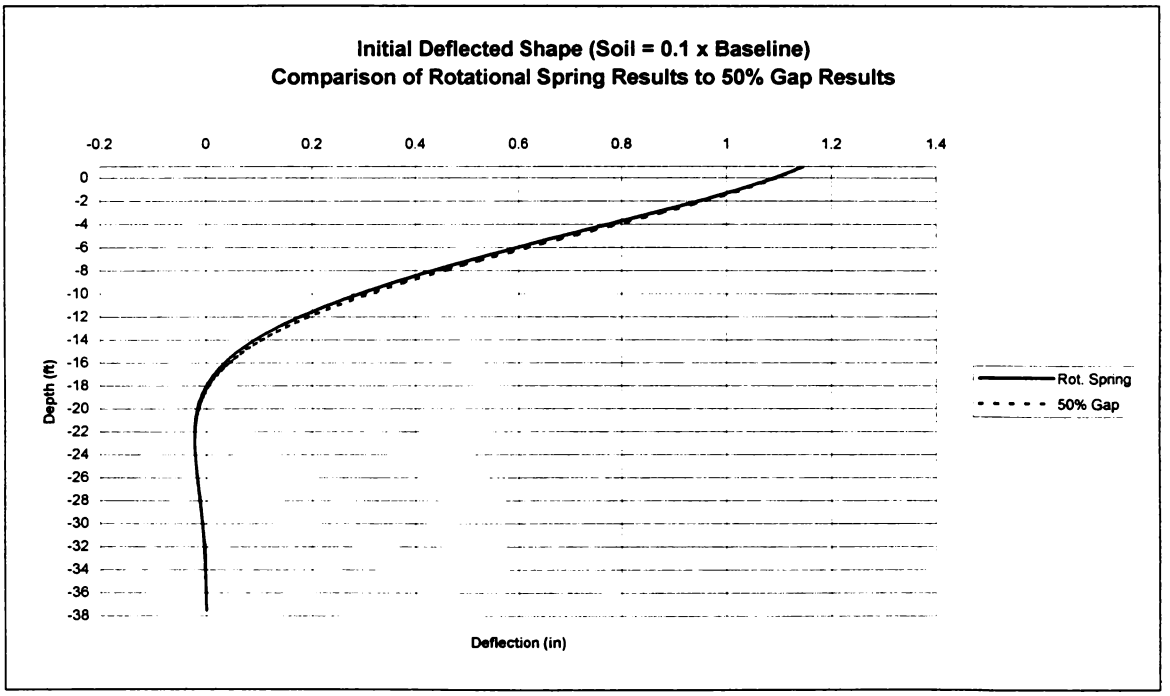


Figure 70: Initial Deflected Shape Comparison (Soil = 0.1 x Baseline)

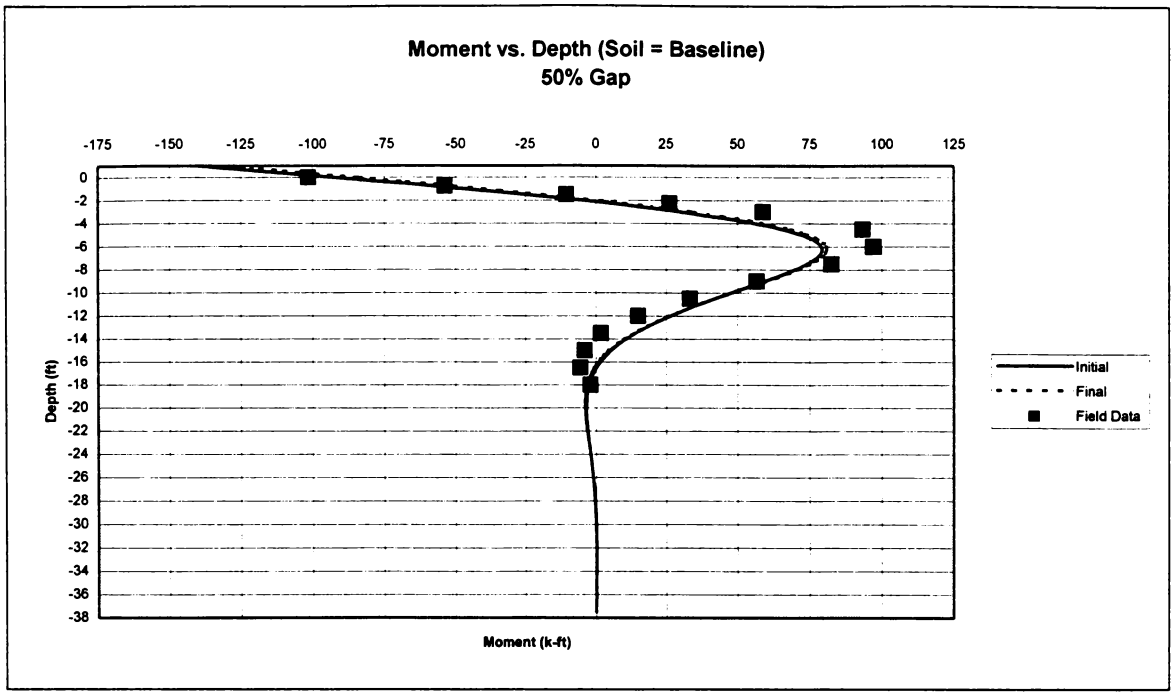


Figure 71: Moment vs. Depth, 50% Gap Model (Soil = Baseline)

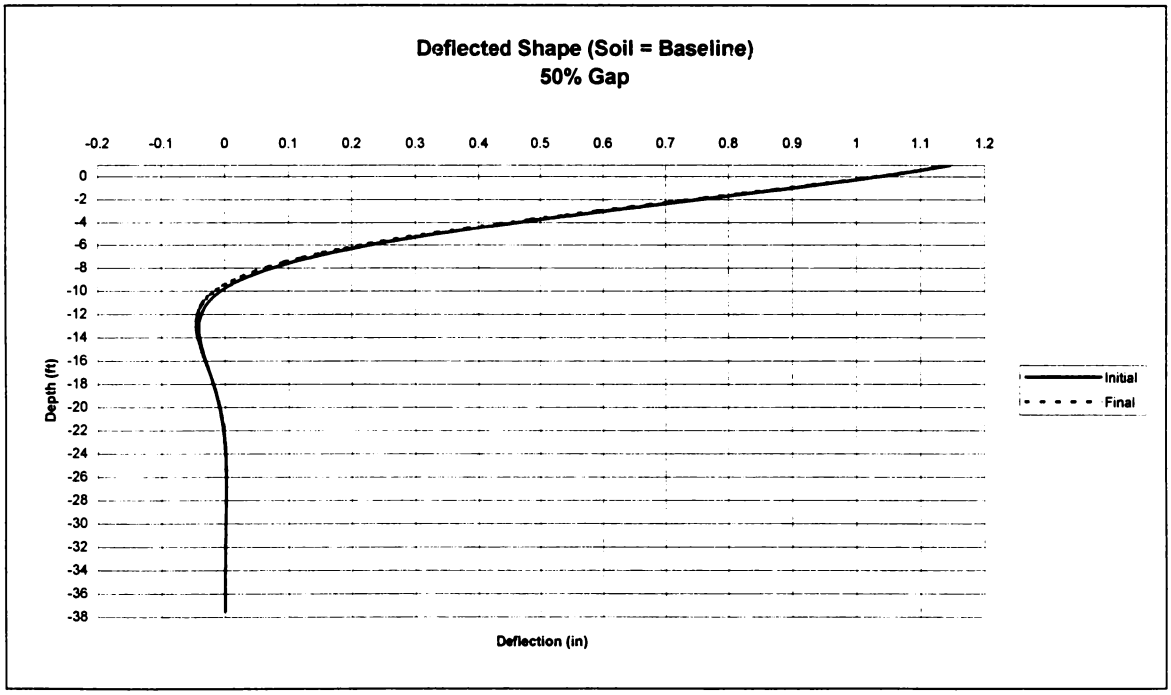


Figure 72: Deflected Shape, 50% Gap Model (Soil = Baseline)

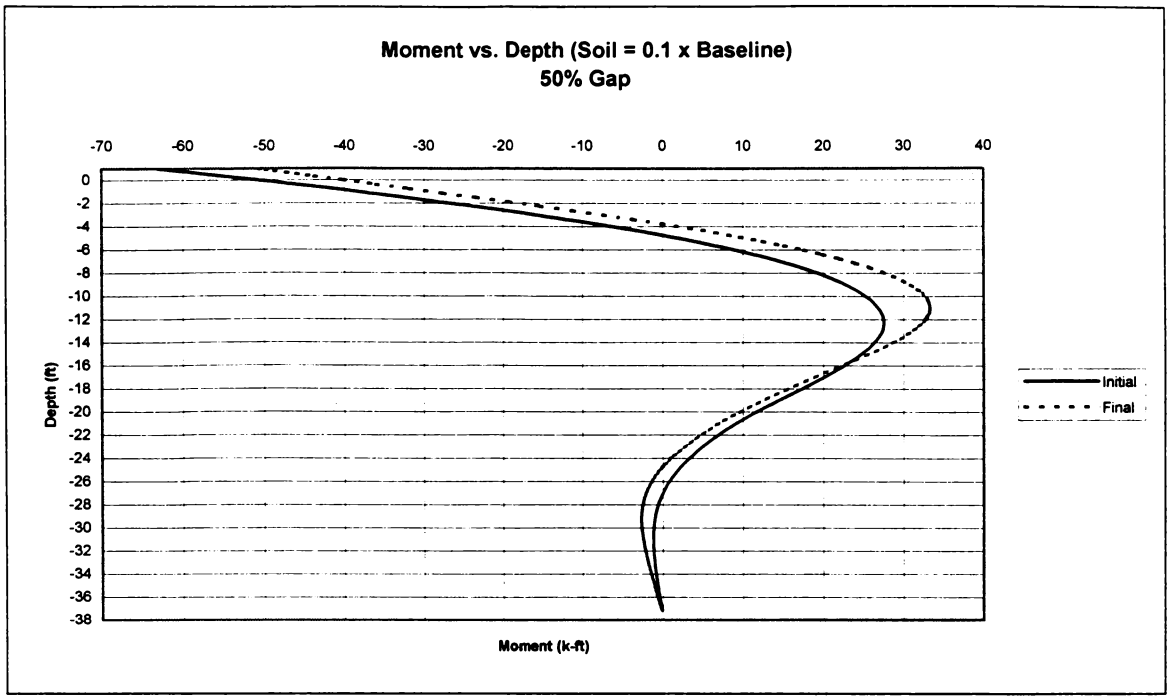


Figure 73: Moment vs. Depth, 50% Gap Model (Soil = 0.1 x Baseline)

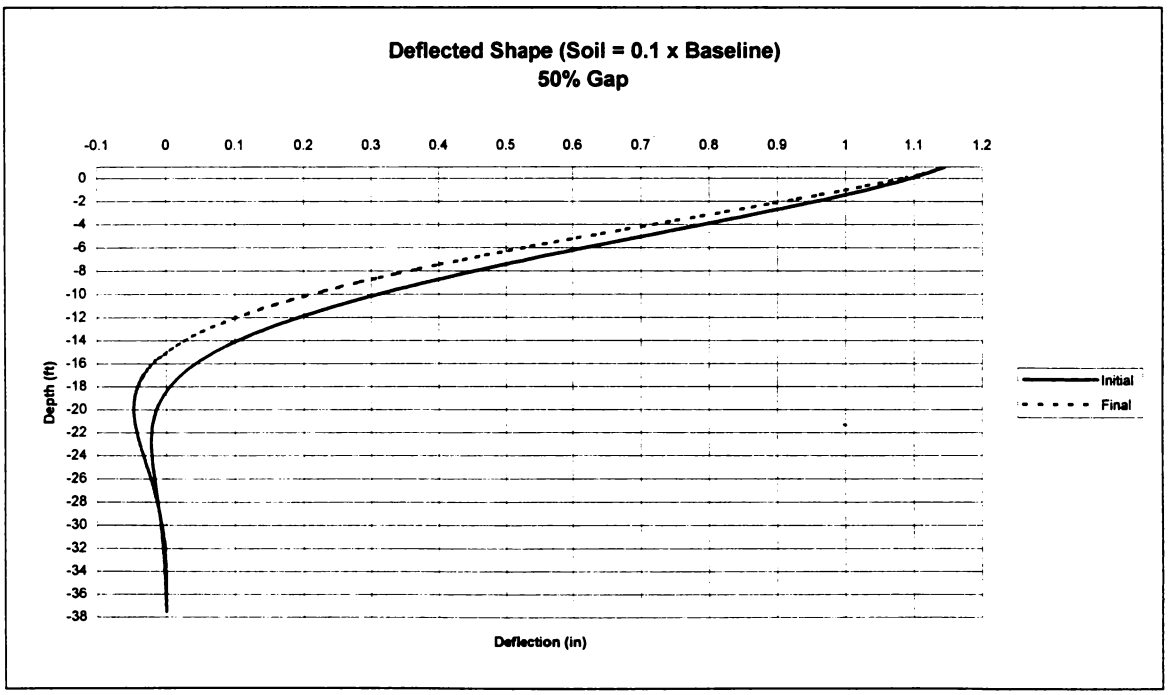


Figure 74: Deflected Shape, 50% Gap Model (Soil = 0.1 x Baseline)

Discussion of 50% Gap Model Results

Pile behavior in the presence of a gap between the pile and the soil was investigated for values of soil stiffness equal to the baseline soil and 10% of the baseline soil. Table 10 presents the initial and final moment data, as well as the expected axial capacity based upon the plastic limit, and the actual axial capacity as determined from the finite element model. In comparison to the rotational stiffness models without a gap, the moment induced into the pile is reduced when a gap between the pile and the soil is incorporated. This reduction in moment is caused by a reduced amount of lateral force required to achieve the desired lateral displacement of the pile head. In the case of the baseline soil, when compared to the rotational stiffness models, the reduction in lateral force is about 28% and the resulting reduction in moment at the top of the pile is approximately 15%. The reduction in moment at the top of the pile allows for a slight increase in axial capacity. In the case of the rotational stiffness models, moment at the top of the pile was significantly reduced (about 19%) after application of the axial load. This phenomenon was not as apparent in the gap model; therefore, the axial capacity initially predicted by the plastic limit curve based on the initial moment induced into the pile was only slightly lower than the axial capacity obtained from the finite element model.

In the presence of a less stiff soil, the gap does not have as great an effect on the overall stiffness of the soil system; therefore, results are only slightly affected when the gap is present. When the soil stiffness is reduced to 10% of the baseline soil, a

comparison of results shown in Tables 8 and 10 indicates that moment magnitudes and axial capacity are minimally changed in the presence of the gap.

Pile instability only occurs when lateral displacements in the center region of the pile embedment depth into the soil become excessively large. In order to produce a gap at elevations well below the ground surface, lateral displacement in the lower regions of the embedment depth must exceed the elastic limit of the soil during the previous load cycle. Lateral displacements large enough to cause permanent deformation to the soil near the mid-depth of the pile did not occur in the rotational stiffness models until the soil stiffness was reduced to a value less than 10% of the baseline soil, in which case stability issues were becoming a problem without the presence of a gap. Therefore, it follows that repeated load cycles that cause a gap in a soil where instability was not an issue prior to the presence of the gap will not lead to an instability problem.

Comparison of Finite Element Results with Results From Gabr's Method

The nomographs presented by Gabr (1994) indicate that for a fully embedded pile with a fixed head free to translate and pinned tip, L_e' is approximately equal to 2.0 for all values of h' greater than about 3.0. When the pile is extended well above the ground surface, the value of L_e' increases. The piles tested in Tennessee had a pile embedment ratio of approximately 0.97, thereby indicating that they were virtually fully embedded. Table 11 presents a summary of the calculated strong axis buckling capacity of a fixed-headed pile free to translate with a pinned tip in soil with a stiffness equivalent to the baseline soil, 10% of the baseline, and 1% of the baseline. The strong axis buckling

capacity is compared to results obtained from the fixed pile head finite element models. Table 12 shows results for weak axis buckling capacity calculated using Gabr's method. Weak axis results that are larger than the finite element strong axis results presented in Table 11 validate the assumption that lateral support provided by the soil will prevent weak axis buckling prior to pile failure about the strong axis.

Table 11: P_{cr} Values Obtained From Gabr's Method (Strong Axis)

Soil Stiffness (% of baseline)	h (in.)	L (in.)	e (h / L)	α	h'	L_e'	L_e (in.)	P_{cr} (kips)	FE Model P_{cr} (kips)
100	450	462	0.97	0.0252	11.4	2	79.3	10294	N/A
10	450	462	0.97	0.0159	7.2	2	125.6	4098	414.8
1	450	462	0.97	0.0100	4.5	2	199.1	1631	592.5

Table 12: P_{cr} Values Obtained From Gabr's Method (Weak Axis)

Soil Stiffness (% of baseline)	h (in.)	L (in.)	e (h / L)	α	h'	L_e'	L_e (in.)	P_{cr} (kips)
100	450	462	0.97	0.0317	14.3	2	63.1	5182
10	450	462	0.97	0.0200	9.0	2	99.9	2063
1	450	462	0.97	0.0126	5.7	2	158.4	821

CHAPTER 8

CONCLUSION

Conclusions Drawn From Finite Element Models

The rotational spring boundary condition models most accurately represent the true behavior of a single pile supporting an integral abutment. These models show that a soil stiffness of approximately 1% of the baseline soil provides adequate support to control instability. This minimum value of required soil stiffness to prevent inelastic buckling is believed to be somewhat conservative (that is, high) due to all soil spring force versus displacement curves being defined as perfectly plastic at the largest deflection experienced during field-testing.

The baseline soil model developed from field data and presented in Chapter 6 possessed a constant of horizontal subgrade reaction (η_h) equal to approximately 67 lb/in^3 and a coefficient of pile-soil compliancy (α), which is a function of soil stiffness and pile stiffness, of 0.025 in^{-1}. Since pile buckling is controlled by the stiffness of both the pile and the soil, the coefficient of pile-soil compliancy is an appropriate measure to be used to identify potential buckling problems. Based on results herein, in the presence of a constant of pile-soil compliancy (α) greater than or equal to 0.01 in^{-1}, which corresponds to a soil with a constant of horizontal subgrade reaction equal to 1% of the baseline soil, pile capacity can be predicted based solely on the plastic limit of the cross section, and without consideration of length effects. Piles could then be designed based upon a single interaction curve per cross section. Achieving a reasonably accurate estimate of pile

response when subjected to lateral displacement would still be necessary, but that is a task easily accomplished using LPILE. The models presented herein incorporated no load factors or reduction factors. In the case of actual design capacity, load and resistance factors should be appropriately applied.

Suggested Design Procedure

In the event that the designer determines that the coefficient of pile-soil compliancy (α) is greater than or equal to 0.01 in^{-1}, the structural capacity of the pile should be determined from the following suggested design approach. Prior to performing this procedure, the designer should develop plastic limit curves for commonly used HP sections.

1. Determine lateral displacement of pile head.
2. Estimate the rotational stiffness of the pile head from an analysis of the superstructure.
3. Collect soil data necessary to perform a lateral response analysis in LPILE.
4. Determine maximum bending moment from LPILE.
5. Choose a pile section based on the plastic limit curves for common HP sections.
6. Check weak axis capacity of chosen section using Gabr's method.

This procedure does not address the vertical bearing capacity of the soil, load and resistance factors, nor the pile-abutment connection. Typical pile design procedures for determining bearing capacity and appropriate load and resistance factors must also be

included in the actual design process. The pile abutment connection must be designed to resist the applied horizontal load and bending moment transferred from the top of the pile to the abutment.

Potential For Further Research

Many states have begun to install piles supporting integral abutments such that bending is about the weak axis. Two advantages to limiting bending to only the weak axis include (1) reduced shear at the pile-abutment connection due to a significant reduction in the bending stiffness of the pile and (2) the elimination of the possibility of lateral torsional buckling in the event that the assumption that the pile is continuously supported out of plane is invalid.

Not addressed in this paper are issues of high stress generation in the abutment due to large lateral and bending forces present when laterally loading a pile about its strong axis. Potential problems arise in the design of the pile-abutment connection that may be partially resolved by orienting the piles such that only weak axis loads are encountered. However, when subjected to large loads that may cause buckling about the weak axis, piles may require additional support to prevent buckling. Further study similar to that presented herein would then be in order.

WORKS CONSULTED

Works Consulted

Abendroth, Robert E., Greimann, Lowell F., and Patrick B. Ebner, "Abutment Pile Design for Jointless Bridges," *Journal of Structural Engineering*, Vol. 115, No. 11, ASCE, November 1989, pp. 2914-2929

American Association of State Highway and Transportation Officials, Standard Specifications for Highway Bridges, 16th Edition, 1996.

American Institute of Steel Construction, Manual of Steel Construction, "Load and Resistance Factor Design," Volume 1, Second Edition, 1998.

Anagnostopoulos, Christos, and Michael Georgiadis, "Interaction of Axial and Lateral Pile Responses," *Journal of Geotechnical and Geoenvironmental Engineering*, Vol. 119, No. 4, ASCE, April 1993, pp. 793-798

ANSYS, Inc., Software Help File

Ashour, Mohamed, and G. Norris, "Modeling Lateral Soil-Pile Response Based on Soil-Pile Interaction," *Journal of Geotechnical and Geoenvironmental Engineering*, Vol. 126, No. 5, ASCE, May 2000, pp. 420-428

Bradford, Mark A., and Nicholas Trahair, "Inelastic Buckling Tests on Beam-Columns," *Journal of Structural Engineering*, Vol. 112, No. 3, ASCE, March 1986, pp. 538-549

Bradford, Mark A., Gizejowski, Marion A., and Nicholas Trahair, "Inelastic Lateral Buckling of Beam-Columns," *Journal of Structural Engineering*, Vol. 113, No. 11, ASCE, November 1987, pp. 2259-2277

Burdette, Edwin G., J. Harold Deatherage, and David W. Goodpasture, Behavior of Laterally Loaded Piles Supporting Abutments, Final Report, The University of Tennessee Center for Transportation Research, The University of Tennessee Knoxville, December 1999.

Burke, Martin P., Jr., "The Genesis of Integral Bridges in Ohio," *Concrete International*, Vol. 18, No. 7, American Concrete Institute, July 1996.

Burke, Martin P., Jr., "The Structure Movement Systems Approach to Effective Bridge Design," *Transportation Research Record 1594*, TRB, National Research Council, Washington, D.C., 1997, pp. 147-153.

Dicleli, Murat, "Simplified Model for Computer-Aided Analysis of Integral Bridges," *Journal of Bridge Engineering*, Vol. 5, No. 3, ASCE, August 2000, pp. 240-248.

Faraji, Susan, Tang, John M., Corvo, Daniel S., and Helmut Ernst, "Nonlinear Analysis of Itegral Bridges: Finite Element Model," *Journal of Geotechnical and Geoenvironmental Engineering*, Vol. 127, No. 5, ASCE, May 2001, pp. 454-461

Gabr, M. A., Wang, J., and M. Zhao, "Buckling of Piles with General Power Distribution of Lateral Subgrade Reaction," *Journal of Geotechnical and Geoenvironmental Engineering*, Vol. 123, No. 2, February 1997, pp. 123-130

Gabr, Mohammed A., Wang, Jibai, and Sam A. Kiger, "Effect of Boundary Conditions on Buckling of Friction Piles," *Journal of Engineering Mechanics*, Vol. 120, No. 6, June 1994, pp. 1392-1400

Greimann, L. F., Abendroth, R. E., Johnson, D. E., and P. B. Eber, Pile Design and Tests for Integral Abutment Bridges. Iowa DOT Project HR-273, Final Report. December 1987.

Girton, D., Hawkins, T., and L. Greimann, "Validation of Design Recommendations for Integral Abutment Piles," *Journal of Structural Engineering*, Vol. 117, No. 7, ASCE, July 1991, pp. 2117-2134

Hetenyi, M., Beams on Elastic Foundation, The University of Michigan Press, Ann Arbor, 1946.

Horne, M.R., Plastic Theory of Structures, 2nd Edition, Pergamon Press, Oxford, 1979.

Kunin, Jonathan, and Sreenivas Alampalli, "Integral Abutment Bridges: Current Practice in United States and Canada," *Journal of Performance of Constructed Facilities*, Vol. 14, No. 3, ASCE, August 2000, pp. 104-111.

Madhav, Madhira R., and Edward H. Davis, "Buckling of Finite Beams in Elastic Continuum," *Journal of the Engineering Mechanics Division*, Vol. 100, No. 6, ASCE, November/December 1974, pp. 1227-1236.

Maleck, Andrea Eden, Second-Order Inelastic and Modified Elastic Analysis and Design Evaluation of Planar Steel Frames, Thesis, Georgia Institute of Technology, 2001.

Myers, Christopher Allen, Behavior of Laterally Loaded Piles Supporting Integral Abutments, Thesis, The University of Tennessee Knoxville, 1998.

Paduana, Joseph A., and Wilfred S. Yee. "Lateral Load Tests on Piles in Bridge Embankments," *Transportation Research Board 517*, TRB, National Research Council, Washington, D.C., 1974, pp. 77-92.

Reese, Lymon C., and S. T. Wang, Technical Manual of Documentation of Computer Program LPILE Plus 3.0 for Windows. Ensoft Inc., Austin, Texas. 1997.

Reese, Lymon C., and William F. Van Impe, Single Piles and Pile Groups Under Lateral Loading. A. A. Balkema, Brookfield. 2001.

Salmon, Charles G., and John E. Johnson, Steel Structures, Design and Behavior, Third Edition, HarperCollins*Publishers* Inc., New York, 1990.

Sun, Keming, "Laterally Loaded Piles in Elastic Media," *Journal of Geotechnical Engineering*, Vol. 120, ASCE, August 1994, pp. 1324-1344

Torkamani, Morteza A. M., and Mustafa Sonmez, "Inelastic Large Deflection Modeling of Beam-Columns," *Journal of Structural Engineering*, Vol. 127, No. 8, ASCE, August 2001, pp. 876-887

Wasserman, Edward P. and J. Houston Walker, "Integral Abutments For Steel Bridges," Highway Structures Design Handbook, Chapter 5, Vol. II, American Iron and Steel Institute, October 1996.

Wasserman, Edward P, "Design of Integral Abutments For Jointless Bridges," *Structure*, CASE / SEI, May 2001.

Welch, R. C., and L. C. Reese, "Laterally Loaded Behavior of Drilled Shafts." Research Report No. 3-5-65-89, Center for Highway Research, The University of Texas at Austin, May 1972.

APPENDIX

COMPUTER PROGRAM

Main Program

```
% This program solves for the deflection and soil reaction of a
% laterally loaded pile for a given moment versus depth curve

% Key variables: h = length of pile segment
%                n = number of segments
%                pile_length = length of the pile including imag. nodes
%                nodes = total number of nodes
%                Q = axial load
%                R = pile stiffness (EI)
%                coef = coefficient matrix for finite difference Eq.
%                A = reduced form of the coefficient matrix
%                b = boundary condition vector
%                sol = solution vector to Ax = b
%                y = deflection vector
%                yk = soil reaction per unit length vector
%                g = soil reaction vector
%                v = shear vector

% Associated function files: add_delta = adds non-zero elements to coef
%                            add_yb = adds deflection boundary
%                                     condition coefficients to coef
%                            add_vb = adds shear boundary condition
%                                     condition coefficients to coef
%                            add_mb = adds moment boundary condition
%                                     condition coefficients to coef

% clear memory
clear all;

% prompt user for segment length and number of segments
h = input('\n   Input the length of segment (in):  ');
n = input('\n   Input the number of segments:  ');

% calculate total length of pile and total number of nodes (incl. imag)
pile_length = h.*(n+4);
nodes = n+5;

% promt user for axial load, pile modulus of elasticity and moment of
% inertia
Q = input('\n   Input axial load on pile (kips):  ');
E = input('\n   Input modulus of elasticity of pile (ksi):  ');
I = input('\n   Input moment of inertia of pile (in^4):  ');

% create R vector assuming pile extends above the ground surface
R = zeros(nodes,1);
for ii = 1:1:nodes-2;
   R(ii,1) = E.*I;
end;

% initialize coefficient matrix of appropriate size
coef = zeros(2.*nodes-4,2.*nodes);
```

```
% insert non-zero coefficients for finite difference equation
for row1 = 1:1:nodes-4;
   col1 = 2.*row1 + 3;
   coef =
add_delta(coef,row1,col1,R(row1+1,1),R(row1+2,1),R(row1+3,1),h,Q);
end;

% insert finite difference coefficients for deflection boundary
% conditions
coef = add_yb(coef,nodes-3,5);
coef = add_yb(coef,nodes-2,2.*nodes-5);

% insert finite difference coefficients for shear boundary conditions
coef = add_vb(coef,nodes-1,5,R(3,1),h,Q);
coef = add_vb(coef,nodes,2.*nodes-5,R(nodes-3,1),h,Q);

% insert finite difference coefficients for moment versus depth
% boundary conditions
for row2 = nodes+1:1:2.*nodes-4;
   col2 = (row2-nodes).*2 + 3;
   coef = add_mb(coef,row2,col2,R((col2-1)./2+1,1),h);
end;

% remove lines corresponding to yk for imaginary nodes in coefficient
% matrix and define A as the reduced coefficient matrix
A = zeros(2.*nodes-4,2.*nodes-4);
A(:,1) = coef(:,1);
A(:,2) = coef(:,3);

for col3 = 3:1:2.*nodes-6;
   A(:,col3) = coef(:,col3+2);
end;

A(:,2.*nodes-5) = coef(:,2.*nodes-3);
A(:,2.*nodes-4) = coef(:,2.*nodes-1);

% read in boundary condition data from a text file
tempfile = fopen('c:\dissertation\pile5_1.txt','rt');
b = fscanf(tempfile,'%g',[1,inf]);
fclose(tempfile);

% convert boundary condition data to a column vector
b = b';

% solve A*sol=b
sol = A\b;

% seperate sol into deflection and soil reaction per length
jj=1;
for ii = 3:2:length(sol)-3;
   y(jj,1)=sol(ii);
   yk(jj,1)=sol(ii+1);
   jj=jj+1;
end;
```

```
% calculate a soil reaction vector
g = yk.*h;
g(1,1) = yk(1,1).*h./2;
g(length(yk),1) = yk(length(yk),1).*h./2;

% calculate a shear vector
v = zeros(length(y),1);
v(1,1)=R(3,1)./(2.*h.^3).*(y(3,1)-2.*y(2,1)+2.*sol(2,1)-
       sol(1,1))+Q./(2.*h).*(y(2,1)-sol(2,1));
v(2,1)=R(4,1)./(2.*h.^3).*(y(4,1)-2.*y(3,1)+2.*y(1,1)-
       sol(2,1))+Q./(2.*h).*(y(3,1)-y(1,1));
for ii = 3:1:length(y)-2;
   v(ii,1)=R(ii+2,1)./(2.*h.^3).*(y(ii+2,1)-2.*y(ii+1,1)+2.*y(ii-1,1)-
           y(ii-2,1))+Q./(2.*h).*(y(ii+1,1)-y(ii-1,1));
end;

% create x vector of depth
x(1,1) = 0;
for ii = 2:1:length(y);
   x(ii,1) = x(ii-1,1)+h;
end;

% create moment vector from boundary condition data
m = b(nodes+1:length(b),1);


% print a table of depth, deflection, moment, shear, shear
differential, and soil reaction
fprintf('\n  Depth     Def.      Moment      Shear       Soil React.');
fprintf('\n  (in)      (in)      (k-in)      (kips)        (kips) ');
fprintf('\n  -----    ------    --------     -------     -----------');

for ii = 1:1:length(y);
   fprintf('\n   %5.1f    %8.5f     %7.1f      %6.2f
            %7.4f',x(ii),y(ii),m(ii),v(ii),g(ii));
end;
fprintf('\n\n');

%end of program
```

Function Files

```
function m=add_delta(cm,row,col,r1,r2,r3,h,Q)
% Add to coefficient matrix
% Input: cm = coefficient matrix
%        row = line number of addition
%        col = column of first entry (ym-2)
%        r1 = Rm-1 EI for section of pile
%        r2 = Rm EI for section of pile
%        r3 = Rm+1 EI for section of pile
%        h = length of segment
%        Q = axial load on pile
% Output: coefficients for ym-2 * rm-1 + ... = 0

m=cm;
m(row,col-4) = r1;
m(row,col-2) = -2.*r1 - 2.*r2 + Q.*h.^2;
m(row,col) = r3 + 4.*r2 + r1 - 2.*Q.*h.^2;
m(row,col+1) = h.^4;
m(row,col+2) = -2.*r3 - 2.*r2 + Q.*h.^2;
m(row,col+4) = r3;
return;


function m=add_yb(cm,row,col)
% Add pile displacement boundry condition to coefficient matrix
% Input: cm = coefficient matrix
%        row = line number of addition
%        col = column entry
% Output: coefficients for yt = delta_pile

m=cm;
m(row,col) = 1;
return;


function m=add_vb(cm,row,col,r1,h,Q)
% Add shear boundry condition to coefficient matrix
% Input: cm = coefficient matrix
%        row = line number of addition
%        col = column entry
%        r1 = EI of pile
%        h = length of segment
%        Q = axial load on pile
% Output: coefficients for R/3h^3 (ym-2 - 2ym-1 +2 ym+1 - ym+2) + Q/2h
(ym-1 +ym+1) = V

m=cm;
m(row,col-4) = -r1./(2.*h.^3);
m(row,col-2) = 2.*r1./(2.*h.^3) - Q./(2.*h);
m(row,col+2) = -2.*r1./(2.*h.^3) + Q./(2.*h);
m(row,col+4) = r1./(2.*h.^3);
return;
```

```
function m=add_mb(cm,row,col,r1,h)
% Add moment boundry condition to coefficient matrix
% Input: cm = coefficient matrix
%        row = line number of addition
%        col = column entry
%        r1 = EI of pile
%        h = length of segment
% Output: coefficients for r/h^2 (ym-1 - 2ym + ym+1) = Mm

m=cm;

m(row,col-2) = r1./(h.^2);
m(row,col) = -2.*r1./(h.^2);
m(row,col+2) = r1./(h.^2);
return;
```

Sample Run

```
» lpile_r

   Input the length of segment (in):  4.5

   Input the number of segments:  49

   Input axial load on pile (kips):  34.7

   Input modulus of elasticity of pile (ksi):  29000

   Input moment of inertia of pile (in^4):  226
```

Depth (in)	Def. (in)	Moment (k-in)	Shear (kips)	Soil React. (kips)
0.0	1.01615	-1223.8	65.07	0.6840
4.5	0.95959	-932.1	63.65	1.4637
9.0	0.90016	-646.9	61.59	2.6628
13.5	0.83873	-373.6	58.45	3.6257
18.0	0.77615	-116.6	54.45	4.3740
22.5	0.71320	120.8	49.80	4.9289
27.0	0.65063	336.0	44.68	5.3101
31.5	0.58910	527.2	39.25	5.5370
36.0	0.52919	693.4	33.67	5.6276
40.5	0.47143	834.3	28.06	5.5993
45.0	0.41625	949.9	22.52	5.4685
49.5	0.36400	1040.7	17.16	5.2508
54.0	0.31496	1107.8	12.06	4.9608
58.5	0.26935	1152.5	7.27	4.6123
63.0	0.22730	1176.3	2.86	4.2182
67.5	0.18889	1181.0	-1.15	3.7906
72.0	0.15412	1168.5	-4.71	3.3404
76.5	0.12296	1140.9	-7.82	2.8780
81.0	0.09533	1100.2	-10.47	2.4127
85.5	0.07110	1048.5	-12.65	1.9530
90.0	0.05011	987.9	-14.38	1.5066
94.5	0.03217	920.4	-15.68	1.0802
99.0	0.01707	847.9	-16.55	0.6795
103.5	0.00459	772.3	-17.05	0.3097
108.0	-0.00550	695.3	-17.19	-0.0252
112.5	-0.01344	618.2	-17.02	-0.3220
117.0	-0.01947	542.6	-16.57	-0.5782

121.5	-0.02383	469.5	-15.88	-0.7925
126.0	-0.02674	399.9	-15.00	-0.9641
130.5	-0.02840	334.6	-13.98	-1.0933
135.0	-0.02904	274.2	-12.84	-1.1813
139.5	-0.02883	219.1	-11.63	-1.2301
144.0	-0.02794	169.5	-10.40	-1.2425
148.5	-0.02653	125.4	-9.16	-1.2223
153.0	-0.02473	86.9	-7.97	-1.1741
157.5	-0.02266	53.6	-6.83	-1.1034
162.0	-0.02043	25.3	-5.77	-1.0166
166.5	-0.01812	1.5	-4.80	-0.9209
171.0	-0.01580	-18.1	-3.93	-0.8245
175.5	-0.01354	-33.9	-3.15	-0.7363
180.0	-0.01139	-46.5	-2.44	-0.6663
184.5	-0.00938	-56.1	-1.80	-0.6251
189.0	-0.00754	-62.8	-1.17	-0.6245
193.5	-0.00589	-66.8	-0.52	-0.6770
198.0	-0.00446	-67.6	0.21	-0.7959
202.5	-0.00323	-64.9	1.11	-0.9955
207.0	-0.00220	-57.7	2.25	-1.2912
211.5	-0.00135	-44.7	3.75	-1.6988
216.0	-0.00064	-24.1	0.00	-0.7555
220.5	-0.00000	0.0	0.00	2.6739

Vita

Earl Evans Ingram was born in San Antonio, Tx on January 5, 1971. He was raised in San Marcos, Tx, where he attended school in the San Marcos Independent School District from first grade through high school graduation. From there, he went to Texas A&M University and received a B.S. in civil engineering in 1993. After graduating from Texas A&M, Earl worked for his father in his family's concrete business. In 1998, Earl left the concrete business to attend graduate school at the University of Tennessee, Knoxville and received a M.S. in 2000 and a Ph.D. in 2002, both in civil engineering.

Earl has been hired as an Assistant Professor by the Civil and Environmental Engineering Department at the University of Tennessee, Knoxville.

5179 3770 36
09/24/02 MAB